



**A MULTISCALE PROCEDURE FOR SOLVING  
NONLINEAR MECHANICAL PROBLEMS IN  
HETEROGENEOUS MEDIA**

**NASSER SAMIR ALKMIM**

**DISSERTATION FOR MASTER'S DEGREE IN STRUCTURAL ENGINEERING AND  
CIVIL CONSTRUCTION  
CIVIL AND ENVIRONMENTAL ENGINEERING DEPARTMENT**

**UNIVERSITY OF BRASÍLIA**

**UNIVERSITY OF BRASÍLIA  
DEPARTMENT OF STRUCTURAL ENGINEERING AND CIVIL  
CONSTRUCTION**

**A MULTISCALE PROCEDURE FOR SOLVING NONLINEAR  
MECHANICAL PROBLEMS IN HETEROGENEOUS MEDIA**

**NASSER S. ALKMIM**

**DISSERTATION SUBMITTED TO THE DEPARTMENT OF CIVIL AND ENVIRONMENTAL ENGINEERING AT UNIVERSITY OF BRASÍLIA AS A REQUIREMENT FOR MASTER'S DEGREE IN STRUCTURAL ENGINEERING AND CIVIL CONSTRUCTION.**

**APPROVED BY:**

---

**Francisco Evangelista Junior, Ph.D.  
(Advisor)**

---

**Edgar Mamiya, D.Sc.  
(External Examiner - Mechanical Engineering Department - University of Brasilia)**

---

**Fabio Comes de Castro, D.Sc.  
(Internal Examiner - Mechanical Engineering Department - University of Brasilia)**

**BRASÍLIA/DF, OCTOBER 2, 2019**

## FICHA CATALOGRÁFICA

ALKMIM, NASSER SAMIR	
A MULTISCALE PROCEDURE FOR SOLVING NONLINEAR MECHANICAL PROBLEMS IN HETEROGENEOUS MEDIA [Distrito Federal] 2019.	
v, 65 p., 210 x 279 mm (ENC/FT/UnB, Mestrado, Estruturas e Construção Civil, 2019)	
Dissertação de Mestrado. Universidade de Brasília. Faculdade de Tecnologia.	
Departamento de Engenharia Civil e Ambiental.	
1. Homogenização computacional	4. Plasticidade
2. Multi Escala	5. Python
3. Método dos Elementos Finitos	
I ENC/FT/UnB	II Título (Mestre)

## REFERÊNCIA BIBLIOGRÁFICA

ALKMIM, N.S. (2019). A MULTISCALE PROCEDURE FOR SOLVING NONLINEAR MECHANICAL PROBLEMS IN HETEROGENEOUS MEDIA. Publicação E.DM - 21A/19, Departamento de Engenharia Civil e Ambiental, Universidade de Brasília, Brasília, DF, vi, 54 p.

## CESSÃO DE DIREITOS

NOME DO AUTOR: NASSER SAMIR ALKMIM

TÍTULO: A MULTISCALE PROCEDURE FOR SOLVING NONLINEAR MECHANICAL PROBLEMS IN HETEROGENEOUS MEDIA

GRAU / ANO: Mestre em Estruturas e Construção Civil / 2019

É concedida à Universidade de Brasília a permissão para reproduzir cópias desta Dissertação de Mestrado e para emprestar ou vender tais cópias somente para propósitos acadêmicos e científicos. O autor reserva outros direitos de publicação e nenhuma parte desta Dissertação de Mestrado pode ser reproduzida sem a autorização por escrito do autor.

## CATALOGUING

ALKMIM, NASSER SAMIR

A MULTISCALE PROCEDURE FOR SOLVING NONLINEAR MECHANICAL PROBLEMS IN HETEROGENEOUS MEDIA [Distrito Federal] 2019.

xii, 65 p., 210 x 279 mm (ENC/FT/UnB, Master, Structural Engineering and Construction, 2019)

Masters's Dissertation. University of Brasilia, College of Technology.

Civil and Environment Engineering Department.

- |                                 |               |
|---------------------------------|---------------|
| 1. Computational Homogenization | 4. Plasticity |
| 2. Multi scale                  | 5. Python     |
| 3. Finite Element Method        |               |

I ENC/FT/UnB

II Degree (Master)

## BIBLIOGRAPHIC REFERENCE

ALKMIM, N.S. (2019). A MULTISCALE PROCEDURE FOR SOLVING NONLINEAR MECHANICAL PROBLEMS IN HETEROGENEOUS MEDIA. Publicação E.DM - 21A/19, Civil and Environment Engineering Department, University of Brasilia, Brasilia, DF, xii, 65 p.

## COPYRIGHT

AUTHOR NAME: NASSER SAMIR ALKMIM

TITLE: A MULTISCALE PROCEDURE FOR SOLVING NONLINEAR MECHANICAL PROBLEMS IN HETEROGENEOUS MEDIA

DEGREE / YEAR: Master in Structures and Civil Construction / 2019

The University of Brasilia is granted permission to reproduce copies of this Master's Dissertation and lend or sell such copies for academic and scientific purposes only. The author reserves other publication rights and no part of this Master's Dissertation may be reproduced without written authorization by the author.

## ABSTRACT

This work presents a multiscale procedure for solving mechanical problem in heterogeneous media. All materials are intrinsically heterogeneous at some scale. At this small scale nonlinear phenomena usually takes place, such as plastic flow and dislocations movements. This localized phenomena ultimately affects the behavior of the whole structure. The implemented procedure consists of solving a boundary value problem (BVP) in the representative volume element (RVE) that takes into account the microstructure for each integration point of the macro scale. There is no explicit declaration of the constitutive relation in the macro scale. In fact, the macro scale constitutive parameters are obtained via homogenization of the microstructure fields. Nonlinearities are also treated only in the micro scale. The micro scale displacement field must satisfy kinematical condition which generate multiple approaches to solve the BVP. This work deals with the two most simple ones, the Taylor and linear boundary condition assumptions. We show via examples that the Taylor assumption produces a stiffer model. The implementation was written using Python programming language and the mesh and post processing plots were done using the free software Gmsh. The solution modules were verified with simple benchmark problems and two more involved examples are provided, one of a perforated notched bar and the other of the proximal part of human femur. The femur example shows that a greater void ratio produces a more flexible model, as expected. It also shows that the microstructure configuration affects considerably the end result.

**Key-words:** Computational Homogenization, Multiscale, Finite Element Method, Plasticity, Python.

## RESUMO

Nesse trabalho é apresentado um procedimento multiescala para resolver problemas mecânicos em mídia heterogênea. Todos os materiais são intrinsecamente heterogêneos em uma escala. Nessa escala, fenômenos não-lineares geralmente ocorrem, como deformações plásticas e movimentos de deslocamento. Esse fenômeno local afeta o comportamento de toda a estrutura. O procedimento implementado consiste em resolver um problema de valor de contorno (PVC) em um volume representativo que considera a microestrutura para cada ponto de integração na escala macro. Não há declaração explícita das relações constitutivas na escala macro. Na realidade, os parâmetros constitutivos da escala macro são obtidos através da homogeneização dos campos da microestrutura. As não linearidades são tratadas apenas na escala micro. Os campos de deslocamento micro devem satisfazer as condições cinemáticas que geram diferentes abordagens para resolver o problema de valor de contorno. Esse trabalho trata das duas condições mais simples, a condição de Taylor e a condição de condição de contorno linear. Mostramos por meio de exemplos que a condição de Taylor produz um modelo mais rígido. A implementação foi realizada inteiramente utilizando a linguagem de programação Python, apenas a malha e os gráficos de pós processamento foram feitos utilizando o programa livre Gmsh. Os módulos implementados foram verificados utilizando problemas de *benchmark* simples e dois exemplos mais complexos são apresentados. O primeiro de uma placa com entalhe circular e material perfurado e o segundo o modelo da parte proximal do fêmur humano. O exemplo do fêmur mostra que quanto maior a porcentagem de vazios mais flexível é o modelo. Ele ainda mostra que a configuração da microestrutura afeta o resultado final consideravelmente.

**Palavras-chave:** Homogeneização computacional, Multiescala, Método dos Elementos Finitos, Plasticidade, Python.

# CONTENTS

<b>1</b>	<b>Introduction</b>	<b>1</b>
1.1	Motivation . . . . .	1
1.2	Context . . . . .	2
1.3	Objectives and scope . . . . .	2
1.4	Implementation considerations . . . . .	3
<b>2</b>	<b>Literature Review</b>	<b>4</b>
2.1	Early efforts . . . . .	4
2.2	Finite elements and homogenization methods . . . . .	4
2.3	Bone modeling . . . . .	7
<b>3</b>	<b>Mathematical and finite element formulation</b>	<b>9</b>
3.1	General methodology . . . . .	9
3.2	Finite element method . . . . .	9
3.3	Plasticity . . . . .	10
3.4	Multiscale Modeling . . . . .	11
3.4.1	Microscale displacement field . . . . .	12
3.4.2	Kinematically admissible micro displacement fields . . . . .	12
3.4.3	Hill-Mandel principle . . . . .	13
3.4.4	Scale transition for the stress . . . . .	14
3.4.5	Equilibrium of the RVE . . . . .	14
3.4.6	Linearized micro-scale virtual work equation . . . . .	15
3.4.7	Homogenized constitutive tangent operator . . . . .	15
3.5	Implementation considerations . . . . .	16
<b>4</b>	<b>Multiscale simulation of composites</b>	<b>18</b>
4.1	Plasticity Verification . . . . .	18
4.2	Multiscale verification with Taylor assumption . . . . .	18
4.2.1	Reinforcement with stiffer elastic modulus . . . . .	20
4.2.2	Reinforcement with higher yield stress . . . . .	21
4.2.3	Microstructure with a void . . . . .	21
4.3	Further composite analysis . . . . .	22
4.3.1	Different RVE boundary condition assumptions . . . . .	22
4.4	Different scale effect . . . . .	23
4.5	Perforated plate . . . . .	26
<b>5</b>	<b>Multiscale simulation of cancellous bone of human femur</b>	<b>31</b>
<b>6</b>	<b>Conclusion</b>	<b>36</b>
<b>A</b>	<b>Mathematical preliminaries</b>	<b>42</b>
A.1	Linearization of a general nonlinear multi variable function . . . . .	42
A.2	Derivative of tensors functions of tensors . . . . .	42
A.3	Chain rule . . . . .	43

<b>B</b>	<b>Computational plasticity</b>	<b>43</b>
	B.0.1 Linearization of the virtual work . . . . .	43
	B.1 Discretization of the linearized virtual work . . . . .	45
	B.2 Numerical integration for elastoplastic constitutive equations . . . . .	45
	B.3 Constitutive model considering Von Mises yield criteria . . . . .	46
	B.4 Single equation return mapping . . . . .	47
	B.5 General elastoplastic consistent tangent constitutive operator for implicit return mappings . . . . .	49
	B.6 Elastoplastic consistent tangent for von Mises model with isotropic hardening	51
<b>C</b>	<b>Extended Finite Elements</b>	<b>52</b>
	C.1 Level set function . . . . .	53
	C.2 Enrichment functions for weak discontinuity . . . . .	53
<b>D</b>	<b>Implementation aspects</b>	<b>55</b>
	D.1 Discretized equilibrium equation . . . . .	55
	D.2 Homogenized tangent constitutive operator for the general case . . . . .	56
	D.3 Homogenized tangent constitutive operator considering Taylor assumption for the micro displacement fluctuation . . . . .	57
	D.4 Linearization of micro equilibrium . . . . .	58
	D.5 Tangential relation between macro strain and gradient of micro displacement fluctuation . . . . .	59
<b>E</b>	<b>Notation convention</b>	<b>60</b>
	E.1 Contraction of tensors . . . . .	60
	E.2 Tensor product . . . . .	61
	E.3 Second order tensors . . . . .	61
	E.4 Fourth order tensors . . . . .	61
<b>F</b>	<b>Algorithms</b>	<b>61</b>
	F.1 Standard Newton procedure . . . . .	61
	F.2 State update procedure . . . . .	61
	F.3 Constitutive consistent tangent matrix . . . . .	63
	F.4 Newton procedure for multiscale analysis . . . . .	63
	F.5 Multiscale incremental procedure . . . . .	64
	F.6 Homogenization procedures . . . . .	64

## LIST OF FIGURES

3.1	Procedure for an increment considering multi-scale. . . . .	10
3.2	Newton method schematically represented to approximate the equilibrium solution . . . . .	11
3.3	Different scales associated with the multi-scale constitutive model. . . . .	12
3.4	Scheme of procedure . . . . .	17
3.5	Element class attributes and methods . . . . .	17
4.1	A single quad element with four integration points. A load step of $\Delta t = 0.01$ and a residual error tolerance of $5 \cdot 10^3$ . . . . .	18
4.2	Comparison between scikit-mechanics and ABAQUS, (a) the tip displacement, (b) the effective von Mises stress, (c) the equivalent plastic strain and (d) the other stresses compoments. . . . .	19
4.3	Different micro structure model . . . . .	19
4.4	Displacement load curve solved and microstructure fields at GP4 considering microstructure with stiffer reinforcement. . . . .	20
4.5	Displacement load curve solved and microstructure fields considering microstructure with stiffer and larger yield strength reinforcement. . . . .	21
4.6	Displacement load curve solved and microstructure fields at GP4 considering microstructure with hole. . . . .	22
4.7	One element model with square voids in the microstructure . . . . .	23
4.8	Displacement load curve solved and microstructure fields at GP3 considering microstructure with a square hole. . . . .	23
4.9	Slab model with boundary conditions for multiscale analysis . . . . .	24
4.10	Model with different number of inclusion (5, 20, 45, 80, 180) but with same reinforcement volume ratio of 23.56%. . . . .	25
4.11	Tip displacement as we increase the number of degree's of freedom for models with different number of inclusions but same reinforcement volume ratio. . . . .	25
4.12	Converged displacement at node 3 (fig. 4.9) we increase the number of inclusions keeping the same reinforcement volume ratio of 23.56% and the multi scale result. . . . .	26
4.13	Perforated plate model . . . . .	26
4.14	Tip displacement of perforated plate Heterogeneous with 12x12 hole grid (see fig. 4.17 d) and Multiscale (MS) with 203 elements (see fig. 4.16 b and c) . . . . .	27
4.15	Evolution of tip displacement of perforated plate in the fully discretized simulation considering different number of voids and comparison with the multiscale simulation with different RVE boundary condition assumption and number of elements. . . . .	28
4.16	Von Mises stress for standard and multiscale analysis of heterogeneous material. In (a) model using standard mixture theory, (b) considering the Taylor assumption and (c) considering linear displacement assumption. . . . .	28
4.17	Von Mises stress for full discretized model with different number N of voids in a grid NxN. Model (a) with a hole grid of 6 perforations and 3168 elements, (b) with a grid of 8 and 6708 elements, (c) with a grid of 10 and 10466 elements and (d) a grid of 12 and 15816 elements. . . . .	29

4.18	Micro cell fields for Taylor and linear assumptions at the gauss point 3 (fig. 4.13). In (a) and (c) the $\bar{\varepsilon}^p$ considering Taylor and Linear boundary displacement assumptions respectively; and (b) and (d) with von Mises stress, $q$ , considering Taylor and Linear boundary displacement assumptions respectively. Each set of fields is correspondent to the instants A, B, C (fig.4.14) . . . . .	30
5.1	Femur section and radiograph image (Cowin 2001). . . . .	31
5.2	Femur model and micro model. . . . .	31
5.3	Displacement at node 4 for a multiscale analysis considering a macro mesh of 102 elements and 4 different micro models, $v_v = 30\%$ , $v_v = 60\%$ each fraction with a single circle and multiple voids. (a) for a load of 2.5 MPa in an elastic domain and (b) for a load of 5 MPa with a plastic domain. . . . .	32
5.4	Von mises stress in the macro domain deformed shape scaled 10x for different micro structures with a 5 MPa load. In (a) with $V_v = 30\%$ Circle, (b) $V_v = 30\%$ Elipses, (c) $V_v = 60\%$ Circle and (d) $V_v = 60\%$ Elipses. . . . .	33
5.5	Equivalent plastic strain in the micro domain deformed shape scaled 30x referent to GP3 shown in fig. 5.2. In (a) $V_v = 30\%$ and (b) $V_v = 60\%$ . . . . .	33
5.6	Equivalent plastic strain in the micro domain deformed shape scaled 30x referent to GP3 shown in fig. 5.2. In (a) $V_v = 60\%$ 5 MPa $\sigma_y = 50$ MPa and (b) $V_v = 60\%$ 5 MPa $\sigma_y = 30$ MPa . . . . .	34
5.7	Comparison between multiscale (MS) analysis and a standard analysis with an effective isotropic elastic modulus, $\bar{E}$ , obtained by applying a known strain, $\varepsilon = [\varepsilon_x, 0, 0]$ , $[0, \varepsilon_y, 0]$ , $[0, 0, \gamma_{xy}]$ , into the microstructure. In (a) the circular microstructure and (b) the multiple elipses. . . . .	34
5.8	Deformed shape scaled 100x and Von Mises stress field of microstructure after applying a known macro strain field, $\varepsilon = [\varepsilon_x, 0, 0]$ , $[0, \varepsilon_y, 0]$ , $[0, 0, \gamma_{xy}]$ where $\varepsilon_x = \varepsilon_y = \gamma_{xy} = 10^{-4}$ in a (a) circular and (b) multiple elipses microstructure. . . . .	35
C.1	Level set function definition. . . . .	53
C.2	Interface definition with 2d array of 1 and -1. . . . .	54
C.3	Distance of grid points to the zero level set, which defines the inclusion interface. . . . .	55
C.4	Enriched nodes and regular nodes in the presence of a discontinuity. . . . .	55

## LIST OF TABLES

4.1	Material properties load control problem . . . . .	18
4.2	Material properties problem with stiffer elastic modulus . . . . .	20
4.3	Material properties problem with higher yield stress . . . . .	21
4.4	Material properties problem with a hole . . . . .	22
4.5	Material properties for example with different RVE boundary assumption . . . . .	23
4.6	Material properties example with different scales . . . . .	24
4.7	Material properties for notched plate . . . . .	26
4.8	Average error between MS linear and heterogeneous analysis. . . . .	27
5.1	Material properties for femur example . . . . .	32

## LIST OF SYMBOLS

$\alpha$	Internal variables
$\varepsilon$	Strain tensor
$\varepsilon^e$	Elastic strain
$\varepsilon^p$	Plastic strain
$\bar{\varepsilon}_v$	Volumetric strain
$\varepsilon_d$	Deviatoric strain
$\bar{\varepsilon}^p$	Equivalent plastic deformation
$\bar{\varepsilon}$	Macro strain tensor
$\dot{\varepsilon}$	Virtual strain tensor
$\varepsilon^\mu$	Micro strain tensor
$\tilde{\varepsilon}^\mu$	Micro strain fluctuation
$\tilde{\varepsilon}^{\mu}$	Micro virtual strain fluctuation
$\sigma$	Stress tensor
$\bar{\sigma}$	Macro stress tensor
$\sigma^\mu$	Micro stress tensor
$\hat{\sigma}^\mu$	Incremental constitutive function
$\sigma_y$	Yield stress
$\eta$	Test function or virtual displacement
$\nu$	Poisson's ratio
$\gamma$	Plastic multiplier
$\Phi$	Yield function
$b$	Body forces
$B$	Discrete gradient matrix for an element
$B^g$	Global discrete gradient matrix
$\hat{D}$	Constitutive matrix
$\hat{D}^\mu$	Micro constitutive matrix
$\bar{D}$	Macro constitutive tensor
$D^\mu$	Micro constitutive tensor
$D^e$	Elastic tangent operator
$D^{ep}$	Consistent tangent constitutive modulus
$E$	Elastic modulus
$f^{\text{int}}$	Internal load vector
$f^{\text{ext}}$	External
$\bar{\mathcal{F}}$	Macro general constitutive functional
$\mathcal{F}^\mu$	Micro general constitutive functional
$G$	Shear modulus
$H$	Hardening modulus
$K$	Bulk modulus
$\mathbf{K}$	Stiffness matrix
$\mathbf{K}_T$	Tangent matrix
$N$	Shape function matrix for an element
$N^g$	Global shape function matrix
$N$	Flow vector
$p$	Volumetric stress
$q$	von Mises equivalent stress
$s$	Deviatoric stress

$t$  Thickness  
 $\mathbf{t}$  Traction  
 $\mathbf{u}$  Displacement vector  
 $\mathbf{u}^\mu$  Micro displacement vector  
 $\tilde{\mathbf{u}}^\mu$  Micro displacement fluctuation  
 $V$  Volume  
 $V^\mu$  Micro volume  
 $V_v$  Volumetric void fraction  
 $\mathcal{V}$  Space of admissible displacement  
 $\mathcal{V}_\mu$  Space of admissible micro displacement

# 1. INTRODUCTION

Composite materials are formed by two or more materials, which remain separate from each other, and each material has its own set of characteristic properties. Examples of this kind of material are reinforced concrete, metal matrix composites and fiber reinforced polymer. The mechanical behavior of a composite material is directly affected by the mechanical properties and geometric configuration of its individual constituents. For instance, the macro-scale effects of plastic or any other dissipative phenomena depend on the complex interaction between heterogeneities and defects at small scales (Sánchez et al. 2013). Here we denote *macro scale* as the scale in which we are mainly interested, the structural level. The lower scales are referred as *micro scales*. Other aspect of composites is their multi-scale nature in which the size of their constituents is much smaller than the resulting structure. As a matter of fact, many materials regarded as homogeneous can have intrinsic heterogeneous nature. Materials like iron-carbon alloy, in which its microstructure depends on the carbon content and heat treatment, or even wood which is composed of cellulose fibers held together with a stiffer material called lignin (Callister 2007). Those two examples are called natural composites.

With advances in the manufacturing industry, many structures will be built using heterogeneous material designed to take advantages of its individual components. As opposed to the natural composites those are artificially made. One example is the disk in turbines, instead of build it with a homogeneous material, they are using long fiber reinforced SiC/Ti composite to resist inertial forced due high rotation speed (Feyel 2003). Those kind of materials are also used to reduce the strength to weight ratio which improves fuel consumption in vehicles. High-temperature strength is another parameter that can be obtained via composites. Industries that take advantage of composites are aerospace, transportation and under water (Callister 2007).

Engineering materials present some sort of separation of scales if we consider that the most basic element of matter is the atom. The organization of atoms form complex structures that are not visible to the naked eye even though this structure impacts the material properties. Engineering usually deals with this multiscale aspect of materials by proposing models that already take into account the microscopic process. However the development of those models can take tremendous amount of effort in laboratory work. Multiscale technique aims to give an alternative to this procedure and is expected to become a central approach to aid new design paradigms for materials and structures (Oliver et al. 2017).

## 1.1. MOTIVATION

When designing a multi-phase structure, it is usually important to establish the relation between the reinforcement phase and the desired overall structure property. The reinforcement phase, at micro level, can present complex behavior that directly affects the macro-scale such as the interaction between heterogeneities and defects (Sánchez et al. 2013). Even though we are dealing specifically with multi phase media, all engineering materials have a intrinsic heterogeneity at some scale. The behavior at this fine scale is generally nonlinear, such as plastic deformation, cracks, dislocations, creep, relaxation and defects. Ultimately, damage and fracture at the micro level governs the behavior of the whole structure (Matouš et al. 2017).

During design of heterogeneous structures, the first approach is to model the whole structure including small scale features, using some discretization technique such as the FEM. This approach leads to overly refined meshes that have a high computational cost (Saeb et al. 2016).

Instead of modeling the structure considering the small scale features, one can simply use the effective, or homogenized, properties obtained experimentally. However, this approach is usually difficult to be performed or too expensive, specially at the design phase, where the

composition may vary significantly and a series of samples are required (Kanouté et al. 2009; Carneiro Molina and Curiel-Sosa 2015; Saeb et al. 2016).

Pure phenomenological theories, in which constitutive response is defined by a set of ordinary differential equations, have drawbacks in regard complex strain paths, specially when damage or phase bonding are considered (Vaz Júnior et al. 2011). One example of such material is fibre-reinforced polymer which has many applications in the aerospace industry, civil structures and prosthetics (Tong et al. 2002; Ullah et al. 2017).

## 1.2. CONTEXT

In recent decades, a series of multi-scale approaches have been proposed and implemented based on different models, such as the *Homogenization Theory of Asymptotic Expansion*, the *effective medium approximation* and many others. Those methodologies consider for their conceptual foundation analytical and semi-analytical procedures, however, they are restricted to simple micro-structure configurations (Sánchez et al. 2013). For a conceptual review of the many theoretical approachs see Kanouté et al. (2009), McDowell (2010), Nguyen et al. (2011), Saeb et al. (2016), and Matouš et al. (2017)

The method used in this work is commonly called in the literature as *multiscale homogenization method*, or computational homogenization, which uses the concept of representative volume element (RVE) to derive global properties of highly heterogeneous media (Suquet 1983). The development of the RVE can be traced back to the work of Hill (1963) which describe it as a typical sample that represent the whole mixture on average. This approach is also referenced as *first-order homogenization* because it considers only the first gradient of the deformation gradient. It consists of using the macro-scale strain to solve the micro-scale problem to obtain the micro-scale stress tensor and the macro-scale stress by volume average. When the Finite Element Method is used at both scales the method is called FE<sup>2</sup> (Smit et al. 1998).

One of the main assumption in which the first-order homogenization method relies is separation of scales which can be stated as “the microscopic length is much smaller than the characteristic length of macro scale” (Geers et al. 2010; Saeb et al. 2016). The first-order<sup>1</sup> computational homogenization does not contain the physical size of the RVE (Javili et al. 2015). Second order approach allows taking into account micro scale size effects when the scales length are comparable (Kouznetsova et al. 2004; Kouznetsova et al. 2002; Kaczmarczyk et al. 2008)

Multi-scale methods have contributed to bridging the gap between mechanics and material science (Geers et al. 2010). The benefits of the method are

1. Modeling based on mechanics at micro scale
2. Macro phenomenological constitutive law not required
3. Represent macro anisotropy with interation of individual phases at micro scale
4. Allows gradual incorporaton of complex mechanical phenomena at the micro scale

As a drawback we have a high computational cost, specially for nonlinear problems, as we later verify.

## 1.3. OBJECTIVES AND SCOPE

The purpose of this work is to apply a multi-scale procedure in order to solve problems that involve highly heterogeneous media. In this procedure we consider nonlinearities only in

---

<sup>1</sup>The denomination first-order is given because the model only considers the first gradient of the macro scale displacement field, macro strain.

the microdomain and transfer homogenized properties to the macro level. We focus on the method procedure therefore we restrict ourselves to plane problems, more specifically plane strain, in order to avoid overly complex data structures in the early stage of the code and to avoid large computational requirements. Plane strain was chosen because its a first step in coding the numerical procedure for solving nonlinear problems. More complex behavior in the microstructure such as the debonding phenomenon was also left out of the scope of the thesis, nonetheless the code is structured in a way which allows further development in this direction. The main feature of this procedure consists in the fact that there is no constitutive assumption for the macro scale and nonlinearities are treated only in the micro scale.

The objectives are:

1. Describe and implement a multi-scale procedure, in its variational form, for solving mechanical problems in heterogeneous media, where the nonlinearities are treated only in the microdomain.
2. Describe and implement a nonlinear solution procedure for plane strain problems using the Finite Element Method. Using the von Mises Yield criteria and a linear isotropic hardening function.

#### **1.4. IMPLEMENTATION CONSIDERATIONS**

The motivation behind developing our own implementation, here called `scikit-mechanics`, instead of using a comercial software resides in the complexity of the non conventional analysis which requires two finite elements solvers to run simultaneously. The in-house development allows prototyping with different procedures due its flexibility.

The code was written in Python, a high level language which is flexible and legible. The model, mesh, material and element are abstracted in classes. The model class encapsulates the whole problem description and is extended with the other classes that are involved in the analysis. This design allows further improvements of the code features without compromising existing capabilities. So, for instance, the micro model object is assigned as an attribute of the model class.

The incremental procedure is performed via a function where the increments and iterations are standards loops. The data structure for the internal variables is currently handled by Python dictionaries due its straightforward key-value structure. Nonetheless the way it is handled in the code is quite complex and there room for improvement via another class abstraction. The usage of dictionaries is convenient but it may also contributes to the slowness of the code.

## 2. LITERATURE REVIEW

Numerous attempts have been made to effectively model composite materials using computational homogenization techniques. Many principles were used when deriving those attempts, this section presents some of the works that deal with multiscale analysis.

### 2.1. EARLY EFFORTS

Eshelby (1957) originally proposed a method to find the current stresses in an elastic solid when a inclusion is subjected to a change in its shape. With his method it was possible to solve many boundary value problems such as the ellipsoidal inclusion with elastic matrix, ellipsoidal hole with elastic in an elastic medium and ellipsoidal cracks in an elastic solid.

Suquet (1983) presented the homogenization theory to derive global properties of heterogeneous media. He defined the macroscopic variables as average of the fields in the heterogeneous body. Noting that if the constituents of the heterogeneous medium are not perfectly bonded (with voids and crack) the averaging process is valid on *extended fields*. He mentions that it is often assumed that micro-strain and or micro-stress is uniform on the boundary of the RVE. The macro-homogeneity condition consists of micro-work been equal to the macro-work (attributed to Hill). The induced micro-strain,  $\varepsilon^\mu$ , by the macro strain  $\varepsilon$  is obtained by localization.

### 2.2. FINITE ELEMENTS AND HOMOGENIZATION METHODS

Guedes and Kikuchi (1990) discussed the homogenization method to determine the effective average elastic constants of linear elasticity of general composite materials when the microstructure is considered. They presented the implementation of homogenization method using the finite element method for linear elastic problems in 2D and 3D. There is a PREMAT module that is responsible to compute the material constants based on homogenization method. They presented a series of simple examples that can be reproduced. They used asymptotic expansion theory and there is no mention to displacement fluctuation nor their kinematical admissibility.

Feyel (1999) presented a multi-scale model based on the multilevel finite element (FE<sup>2</sup>) in order to take into account heterogeneities in the behavior between fibre and matrix. He described the FE<sup>2</sup> model by considering only the constitutive relations on the microscopic scale. Then, the macroscopic strain and stresses are computed with homogenization and localization equations. The behavior of microstructure is obtained by FE computation. The steps in the FE<sup>2</sup> are: first, localization of macroscopic strain  $\varepsilon$ , then compute the response of the microstructure  $\sigma^\mu$ , finally homogenization of the micro-stress by averaging,  $\sigma = \langle \sigma^\mu \rangle$ , where  $\langle \cdot \rangle$  denotes volume average. He approximates the stiffness matrix by a *perturbation method*, which consists of finding the response of the structure for small strain variations. For 2D problems it is necessary to solve 4 FE problems. Finally he presents an example of four point bending problem where the influence of fibers sizes were analyzed.

Feyel and Jean-Louis Chaboche (2000) presented and analysis of the behavior of structures reinforced by long fibre SiC/Ti composite material with periodic microstructure. The analysis is carried with the multilevel finite element approach (FE<sup>2</sup>). In this approach the constitutive equations are only written in the microscopic scale. They showed an example of a simple 8-node quadrilateral element with 4 Gauss points. The local model was tested with four different meshes, the coarse one has 266 elements, they do not tell if the micro scale elements were quad4 or quad8.

Terada and Kikuchi (2001) presented a general algorithm for multi-scale analysis. Their algorithm goal is to generalize the multi-scale problems for heterogeneous media with fine

periodic microstructure using variational statements thus unifying the computational treatment. Their algorithm is similar to the one implemented for this work. They also conclude the infeasibility of the procedure for practical application when nonlinearity is considered due to large computational requirements. The difficulties encountered then can be solved with approaches such as localized usage of the method and parallelization. They do not mention the different types of boundary conditions that can be applied in the RVE.

Miehe and Koch (2002) investigated algorithms for computational homogenized stresses and overall tangent moduli of microstructure considering small strains. It is shown that the overall stress and tangent stiffness can be defined exclusively in terms of discrete forces and stiffness properties on the boundary. He focused on deformation driven where the macroscopic deformation is controlled. Different types of boundary conditions are investigated, linear displacements, constant tractions and periodic displacements. He presented micro-to-macro transition algorithms. The displacement boundary conditions imposed in the microstructure is obtained with  $\mathbf{u}_q = \mathbf{D}^T \boldsymbol{\varepsilon}$ , where  $\boldsymbol{\varepsilon}$  is the macroscopic strain vector and  $\mathbf{D}$  is a  $3 \times 2$  (for  $n_{\text{dim}} = 2$ ) with the coordinates of a point in the reference configuration. The product of  $\mathbf{D}$  and  $\boldsymbol{\varepsilon}$  gives the displacement at a specific node.

Böhm et al. (2002) presented a unit cell approach for randomly oriented fibers, which differs from this work. They only performed the analysis on the micro structure, generating the homogenized variables. The solved problem was not coupled with a macro structure like in this work.

Yuan and Fish (2008) presented a computational homogenization approach for linear and non-linear mechanics using ABAQUS and Python.

de Souza Neto and Feijóo (2008) discussed the equivalence relationships for large strain multi-scale solid constitutive model based on volume average of microscopic stress over RVE. He pointed out that for finite strain multi-scale constitutive model based on the reference volume average of the first Piola-Kirchhoff stress differs from the spatial volume average of the Cauchy stress field. But under certain kinematically admissible conditions, both are mechanically equivalent.

Temizer and Zohdi (2007) They showed that as we increase the number of particles in the RVE the homogenized parameter converge to a certain value and there is a fixed difference between the value obtained using linear displacement boundary conditions and traction boundary conditions. However, with mesh refinement the gap between the choice of two boundary conditions decrease. This was also tested by Saeb et al. (2016).

Miehe et al. (2010) presented a new method for quasi-static homogenization of granular microstructure.

Saavedra Flores and de Souza Neto (2010) presented a workaround for the high computational cost of the coupled multiscale problem. In their discussion, the size of the RVE represented the major factor that affected in computational time. Therefore, their goal was to use symmetries in order to choose the most appropriate RVE size without compromising the solution accuracy.

Saavedra Flores and Friswell (2012) presented a couple multi-scale finite element model for constitutive description of an alumina/magnesium alloy/epoxy composite. Their work aims to use multiscale simulation to shed light on how natural materials, such as wood, can be optimized on the microstructure level to absorb large amounts of strain before failure.

Tchalla et al. (2013) presented a implementation of multilevel finite element method in ABAQUS. The implementation is used to model composite materials. The multilevel finite element method framework consists of finding the unknown macro-scale constitutive relationship by solving a local finite element problem at micro-scale. They used a Python script and

FORTRAN subroutines. Feyel and Chaboche developed their own code ZéBuLon, based on Newton-Raphson procedure to solve nonlinear problems. They pointed out that two-scale finite element method remains unused because of the great effort needed to implement it. The micro-macro problem is described. At macro-scale the constitutive relation is unknown. The stresses at macro-scale are computed by solving a local finite element. The local finite element is defined by the same equations as the macro-scale. The boundary conditions used in the local problem are based on the macro-scale deformation tensor. The deformation tensor is computed as the integral of the deformation rate, which is approximated in ABAQUS by central differencing. After solving the micro-scale problem the macro-scale stress is obtained via volumetric average of micro-scale stress. With the macro-scale stress, the homogenized linear elasticity tensor can be calculated. They presented the implementation of two-level analysis for linear elastic and nonlinear cases.

Sánchez et al. (2013) presented a good description of the variational formulation of multi-scale model. They considered that at the macroscopic level the medium is continuum but it admits nucleation and cohesive cracks due to progressive localization phenomena occurring at microscopic level. The microscopic effect is considered at the macro-scale only when a certain criterion is fulfilled. Their main goal is to model micro-scale phenomena that leads to material failure.

Eftekhari et al. (2014) presented a XFEM multi-scale approach for fracture analysis of carbon nanotube reinforced concrete. At nanoscale, molecular dynamics is used to find mechanical properties of carbon nanotubes. Then, a hydration model is used to find the chemical composition of cement paste. The addition of carbon nanotubes can increase the strength of concrete up to 50%. It also increases the fracture resistance properties, decreasing porosity and shrinkage which contributes to long term durability. A finite element analysis is constructed for the micro-scale using the properties from the nanotubes and the chemical composition of cement. A mechanical and damage response of the structure is obtained from the micro-scale finite element analysis. The homogenized response of the micro-scale is upscaled to a macro-scale analysis. The nanoscale analysis results in the mechanical properties of CNTs, elastic modulus, failure stress, Poisson's ratio. The molecular dynamics was performed using the LAMMPS open source code, in order to capture the stress-strain response. Only the tensile behavior of CNTs was carried because they rarely bear compressive stresses. The micro model presents three different phases: unhydrated, hydrated phases and porosity. The problem takes in consideration an isotropic damage model. An incremental procedure is carried using a Newton-Raphson solver. The model is incrementally loaded by the applied strain and the corresponding stress is computed in order to calculate the mechanical properties. The author did not specify how the micro-scale mesh was produced or solved, only that they have used the open source code OOFEM.

Blanco et al. (2016) presented a unified variational theory for a general class of multi-scale models based on the representative volume elements. This work consolidates the variational basis of the multiscale theory. They also presented a numerical example.

Carneiro Molina and Curiel-Sosa (2015) presented a multi-scale finite element procedure for nonlinear multi-phase materials. They used the multi-scale computational homogenization which is the *most effective way* to deal with arbitrary nonlinear material behavior at micro level. In the procedure, the stress-strain relationship is computed at every macro-scale integration point.

de Souza Neto et al. (2015) presented an extension of the classical multi-scale theory by considering inertia effects and body forces. Their description of the model is based on solid variational foundations which allows further usage of the methodology to different problems, such as dynamics, material failure with kinematical discontinuities and coupled multi-physics.

Bencheikh et al. (2017) presented a multi-scale modeling of thin films that are applied to coat tools during machining operations. The problem involves thermomechanical coupling and it was solved using a combination of XFEM and level set functions. The framework was applied to solve 2D transient thermomechanical problems. The results were compared to classic FEM approach using the number of Gauss points.

Oliver et al. (2017) presented an alternative to the expensive  $FE^2$  procedure. In regard the code of the method, it is the same as the standard couple multiscale with an RVE. The alternative method consists of substituting the displacement fluctuation unknown variables to strain fluctuation. The RVE boundary conditions are also formulated in terms of the strains. They also used a method to reduce the number of quadrature points to further reduce the computational cost. They considered a RVE with only elastic materials and in order to represent the fracture phenomena a large set of cohesive softening bands that provide a good approximation for possible crack paths. The micro-problem is formulated considering displacement fluctuations and the variational equations are also presented.

Ullah et al. (2017) presented a multi scale framework for fiber-reinforcement polymer composites. They used an unified approach to impose the multiple types of RVE boundary conditions. They performed multiple tests to check the response of the micro structure alone where the homogenized stress computed was compared with experimental data. They also used cohesive interface elements to model fiber-matrix decohesion.

Eidel and Fischer (2018) presented the formulation of heterogeneous multiscale finite element method (FE-HMM) for *linear elastic solids*. They show how the FE-HMM compares to the  $FE^2$ , which is used in this work. This comparison establishes a link between asymptotic homogenization from the FE-HMM with the macro homogeneity conditions, *Hill-Mandel conditions*. The  $FE^2$  most prominent feature is the two level finite element procedure, which is used in this work. They also derived error estimates for the multiscale procedure FE-HMM which helps with macro and micro mesh refinements. The micro problem is solved using a single increment step, the same was done in this dissertation. While the  $FE^2$  method is already been used for linear and nonlinear problems, the FE-HMM extension to nonlinear problems is not straightforward.

Matouš et al. (2017) presented a review of the multiple procedures to solve multiscale nonlinear problems. They show the state-of-the-art platform of predictive simulation. This platform allows the use of image-based simulation that work together with the experiment. They classify multiscale methods based on the procedure adopted as *concurrent methods*, *hierarchical methods* and *hybrid methods*. This work adopts the hierarchical method, which link both scales by means of averaging theorems.

### 2.3. BONE MODELING

Regarding the usage of the Finite Element Method for modeling bone biomechanics, Parashar and Sharma (2016) presented a review of the current state of the art. The mechanical prediction of bone behavior is the subject of many publications. In Budyn and Hoc (2007) they used a multiple scale method to model crack growth in cortical bone, albeit the simulation is performed only in a 2D four phase microstructure. Their goal was to figure out the importance of the microstructure in bone failure. Podshivalov et al. (2011) proposed a new 3D multiscale finite element analysis of trabecular bone but performed a test case in 2D. They used a technique to convert a medical image into the microstructure mesh. In the homogenization method they used an ad-hoc method where a set of boundary conditions is applied on the micro structure in order to find the effective material parameters. Works such as Abdel-Wahab et al. (2012) deals with only the bone micro structure analysis to investigate the effect of micro structure changes

in crack propagation. They used a 2D model with XFEM to simulate cortical bone. van den Munckhof and Zadpoor (2014) assess the accuracy of FE methods for predicting fracture load of proximal femoral. They concluded that FE produces results more accurate than usual fracture risk techniques used, however the FE results are highly dependent on modeling quality and methodologies which lack standards.

In Ural and Mischinski 2013 they showed that bone fracture phenomena is highly dependent of a multiscale mechanism. The 2D analysis is used to provide information on how microstructural properties influence the overall bone behavior, for instance, the effect of cement line strength on crack deflection. Their main focus was on modeling the crack formation on the cohesive element used to simulate the cement line. They used computational fracture mechanics based on the cohesive finite element method to model this phenomena.

In Vellwock et al. 2018 they used a mixture of multiscale techniques together with extended finite elements (XFEM) to model fracture behavior of bone inspired composite. The goal of the authors with their simulation was to provide understanding of the effect of microstructure in overall material behavior. They separated the domain in three regions: linear elastics, damage initiation and damage evolution. All the analysis were based on the cohesive segment approach.

### 3. MATHEMATICAL AND FINITE ELEMENT FORMULATION

In this section the mathematical model for the standard Finite Element is presented.

#### 3.1. GENERAL METHODOLOGY

One solution to model the interaction between different material scales is a multi-scale strategy in which both scales are modeled separately and coupled together. In this coupled analysis the homogenized properties of the material are obtained from the micro-scale analysis, which is performed at every macro-scale integration point. This way the constitutive relation is not required at the macro level.

Both scales are solved using the Finite Element Method. The standard Newton Raphson procedure is used for incrementally solving the macro-scale problem in multiple increments and solve the micro-scale problem in a single increment. Each micro scale analysis has as input parameters the macro strain trial increment. After the micro scale analysis is completed the homogenized parameters are passed to the macro scale and convergence is checked. If it converged, the internal variables are updated and the next macro increment is started. If not converged, we repeat the global iteration and solve the micro scale problem again with another macro strain increment.

Figure 3.1 shows schematically the adopted procedure. In a macroscale increment  $[t_n, t_{n+1}]$  the goal is to compute the nodal displacement at  $t_{n+1}$  such that equilibrium is satisfied. Starting with a known displacement increment  $\Delta \mathbf{u}^{(k+1)} = \mathbf{u}_{n+1}^{(k+1)} - \mathbf{u}_n$ , in which  $\Delta \mathbf{u}^{(1)} = \mathbf{0}$ , the solution proceeds to a step called as localization. The array  $\alpha_n$  contains the internal variables at the gauss points. In this step, element matrices are formed through calculations using standard state update algorithms for each integration point, see Simo and Hughes (1998) and de Souza Neto et al. (2008) for a detailed explanation.

When a multi-scale procedure is considered, in the macro-scale localization, at each macro-scale integration point, a micro-scale increment procedure is called. The micro-scale procedure repeats the same steps of the macro one, the difference is that this one is performed in a single load (or pseudo-time) increment.

#### 3.2. FINITE ELEMENT METHOD

The Finite Element Method is a discretization method in which the differential equation that describe a physical phenomena is solved on an weak sense by assigning an approximated solution formed as linear combination of known functions. This approximation is such that the domain is subdivided into finite elements connected by their nodes. The method when applied to linear mechanical problems yields a linear system of equations,

$$\mathbf{K} \mathbf{u} \stackrel{\text{law}}{=} \mathbf{f}^{\text{ext}} \quad (3.1)$$

where  $\mathbf{K}$  is the assembled stiffness matrix,  $\mathbf{u}$  is a vector with unknown nodal displacements and  $\mathbf{f}^{\text{ext}}$  is the vector with external equivalent nodal load.

The element stiffness matrix is given by,

$$\mathbf{K}^{(e)} \stackrel{\text{def}}{=} \int_{V^{(e)}} \mathbf{B}^T \hat{\mathbf{D}} \mathbf{B} dV \quad (3.2)$$

where  $\mathbf{B}$  is the discretized version of the symmetric gradient operator,  $\nabla^s$ , which relates the strains and displacements,  $\varepsilon \stackrel{\text{def}}{=} \nabla^s \mathbf{u}$ , for small displacements. The matrix  $\hat{\mathbf{D}}$  is the constitutive matrix which in the elastic case is constant and in the plastic case is dependent on the stress state,  $\hat{\mathbf{D}} = \hat{\mathbf{D}}(\boldsymbol{\sigma})$ , where  $\boldsymbol{\sigma}$  is the vector representation of the Cauchy stress tensor,  $\boldsymbol{\sigma}$ .

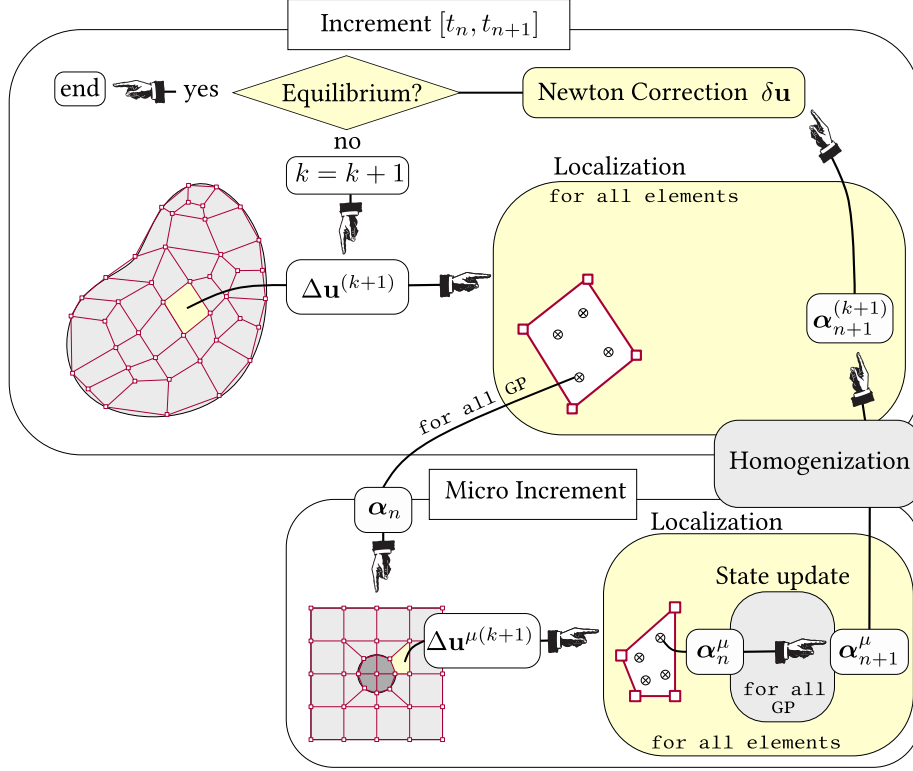


Figure 3.1. Procedure for an increment considering multi-scale.

### 3.3. PLASTICITY

When the stress-strain relation is unknown in eq. (3.1), this equation is written as,

$$\mathbf{f}^{\text{int}}(\mathbf{u}) \stackrel{\text{law}}{=} \mathbf{f}^{\text{ext}} \quad (3.3)$$

which represents a balance law where the internal load,  $\mathbf{f}^{\text{int}}(\mathbf{u})$ , must be equal to the external load. The internal load vector is computed for an element with,

$$\mathbf{f}_{(e)}^{\text{int}}(\mathbf{u}) \stackrel{\text{def}}{=} \int_{V(e)} \mathbf{B}^T \hat{\boldsymbol{\sigma}}(\boldsymbol{\alpha}, \boldsymbol{\varepsilon}) dV \quad (3.4)$$

where  $\hat{\boldsymbol{\sigma}}(\boldsymbol{\alpha}, \boldsymbol{\varepsilon})$  is a general constitutive equation, when an incremental procedure is adopted, that depends on the strains  $\boldsymbol{\varepsilon}$ , and internal variables  $\boldsymbol{\alpha}$ . This equation is nonlinear because the incremental constitutive function depends on the unknown displacements,  $\hat{\boldsymbol{\sigma}}(\boldsymbol{\alpha}, \boldsymbol{\varepsilon}(\mathbf{u}))$ . See appendix D.1 for detailed derivation of the discretized FEM equation.

When solving a nonlinear problem a incremental procedure is adopted. So the problem can be stated as *knowing the state at  $t_n$ , find the displacement,  $\mathbf{u}_{n+1}$  and internal variables,  $\boldsymbol{\alpha}_{n+1}$  at time  $t_{n+1}$* . For a single increment the eq. (3.4) becomes,

$$\mathbf{f}_{(e)}^{\text{int}}(\mathbf{u}_{n+1}) \stackrel{\text{def}}{=} \int_{V(e)} \mathbf{B}^T \hat{\boldsymbol{\sigma}}(\boldsymbol{\alpha}_n, \boldsymbol{\varepsilon}_{n+1}) dV \quad (3.5)$$

thus, the constitutive function is dependent only on the unknown strains  $\boldsymbol{\varepsilon}_{n+1}$  because the internal variables  $\boldsymbol{\alpha}_n$  are *constant* during a single step.

In order to solve the nonlinear eq. (3.3) we use the Newton method which linearizes it, see appendix A.1 for details on linearization. The Newton method yields,

$$\mathbf{K}_T^{(k)} \delta \mathbf{u}^{(k+1)} = - \left( \mathbf{f}^{\text{int}}(\mathbf{u}_{n+1}^{(k)}) - \mathbf{f}_{n+1}^{\text{ext}} \right) \quad (3.6)$$

where  $\mathbf{K}_T$  is the tangent stiffness matrix and the vector difference is defined as equilibrium residual,  $\mathbf{r} = \mathbf{f}^{\text{int}} - \mathbf{f}^{\text{ext}}$ . The vector  $\delta \mathbf{u}^{(k+1)}$  is the Newton correction which corrects the solution and guides it towards equilibrium,

$$\mathbf{u}_{n+1}^{(k+1)} = \mathbf{u}_{n+1}^{(k)} + \delta \mathbf{u}^{(k+1)} \quad (3.7)$$

this procedure of approximating the equilibrium solution iteratively is schematically represented in fig. 3.2.

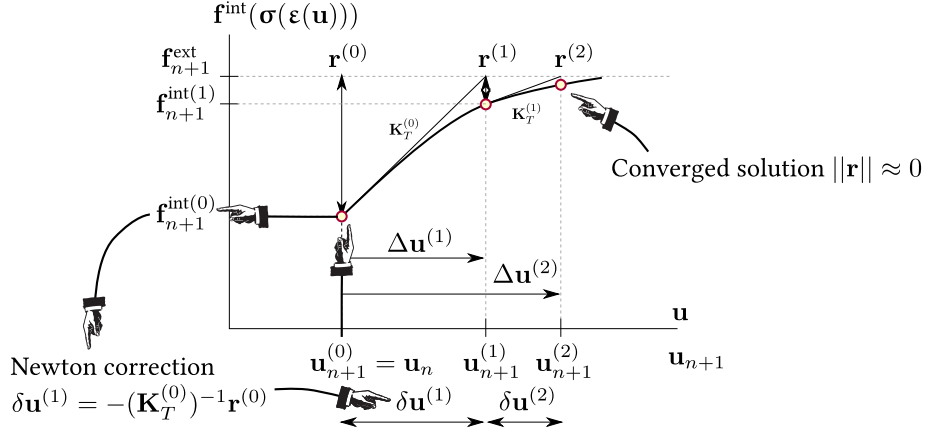


**Figure 3.2.** Newton method schematically represented to approximate the equilibrium solution

The material nonlinearity, represented by the constitutive function,  $\hat{\sigma}(\alpha_n, \epsilon_{n+1})$ , consists of the relation between stresses and strains. In a numerical procedure we need to find the internal state variable for a given strain. This procedure can be stated as: *for a given strain increment  $\Delta \epsilon = \epsilon_{n+1} - \epsilon_n$  and internal variables  $\alpha_n$  find the internal variables at the next step  $\alpha_{n+1}$  which includes the stress  $\sigma_{n+1}$  and elastic strain  $\epsilon_{n+1}^e$ .*

This problem can be solved using a standard state update procedure assuming von Mises yield criteria a particular hardening rule. In this work it was assumed a linear hardening curve. Details of the state update procedure can be found in Simo and Hughes (1998), de Souza Neto et al. (2008), and Borst and Crisfield (2012). The computational implementation is also detailed in appendix B.

### 3.4. MULTISCALE MODELING

This section deals with the variational formulation of multiscale procedure.

Multiscale theory aims to model constitutive behavior of solids by considering its different scales. Figure 3.3 shows the different scales associated with multi-scale modeling. The basic assumption used to derive multi-scale constitutive theories is that the micro-scale characteristic length,  $\ell^\mu$ , is much smaller than the macro-scale characteristic length  $\ell$ . Zooming into a point on the macro structure we can see how the micro structure is arranged, then we can select a Representative Volume Element (RVE) to perform our micro analysis.

The classical multi-scale theory can be derived from two principles: (i) kinematical admissibility, and (ii) multi-scale virtual power (de Souza Neto et al. 2015). These two principles are used to establish the transition between scales. The kinematical admissibility arises from the average relation between micro and macro strains. The multi scale virtual power is related to the Hill-Mandel principle (Hill 1963; Hill 1972) which states that the volume average of the power of an equilibrium stress field over an RVE equals to the macro-scale stress power. Both will be detailed in subsequent sections.

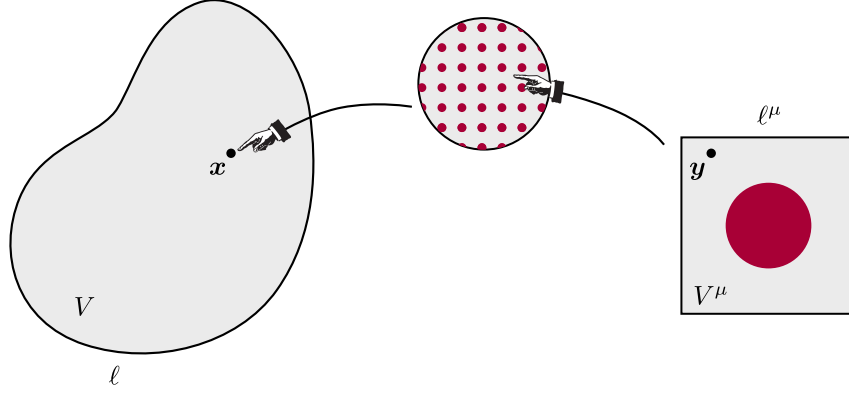


**Figure 3.3.** Different scales associated with the multi-scale constitutive model.

### 3.4.1. MICROSCALE DISPLACEMENT FIELD

The micro-scale displacement field can be split in two parts, one related to the effect of macro-scale strain,  $\bar{\boldsymbol{\varepsilon}}$ . This step is also known as additive split of microscopic displacement,

$$\mathbf{u}^\mu(\mathbf{y}) \stackrel{\text{def}}{=} \bar{\boldsymbol{\varepsilon}}(\mathbf{x})\mathbf{y} + \tilde{\mathbf{u}}^\mu(\mathbf{y}) \quad (3.8)$$

where  $\tilde{\mathbf{u}}^\mu(\mathbf{y})$  is a micro-scale *displacement fluctuation* unknown part of the micro-scale displacement. The term  $\mathbf{y}$  represents a point coordinate in the micro-scale and the product  $\bar{\boldsymbol{\varepsilon}}\mathbf{y}$  the effect of the macro-scale strain in the micro-scale displacement.

The micro displacement fluctuation is a periodic function which means that it has identical value at the boundary of the RVE domain when this domain is translated parallel to the direction of invariance of the lattice by a distance equal to its length (Michel et al. 1999).

The micro-scale strain can be obtained from eq. (3.8),

$$\boldsymbol{\varepsilon}^\mu \stackrel{\text{def}}{=} \bar{\boldsymbol{\varepsilon}} + \tilde{\boldsymbol{\varepsilon}}^\mu \quad (3.9)$$

where  $\tilde{\boldsymbol{\varepsilon}}^\mu = \nabla_y^s \tilde{\mathbf{u}}^\mu$  is the micro strain fluctuation. The bar over the variables,  $(\bar{\cdot})$ , indicates an homogenized quantity. The superscript  $(\cdot)^\mu$  indicates a micro-scale variable (also encounter in the literature as  $\mu = 1$ ).

Notice that the micro strain does not depend explicitly on the micro position  $\mathbf{y}$ , this allow independence of the RVE dimensions, which is a benefit of the first order multiscale analysis (Gruer 2015). Multiple authors use this split form of micro displacement (Michel et al. 1999; de Souza Neto and Feijóo 2006; Saavedra Flores and de Souza Neto 2010; Kanouté et al. 2009; Otero et al. 2018)

### 3.4.2. KINEMATICALLY ADMISSIBLE MICRO DISPLACEMENT FIELDS

The kinematics conditions for the micro displacement come from the coupling between the two scales. This coupling is based on average theorems which was proposed, for infinitesimal deformations, by Hill (1963). The coupling states that the macro strain is equal to the volume average of the micro strains. Substituting the definition of the micro strain field in eq. (3.9) into the following average relation for the strains,

$$\bar{\boldsymbol{\varepsilon}}(\mathbf{x}) \stackrel{\text{def}}{=} \frac{1}{V^\mu} \int_{V^\mu} \boldsymbol{\varepsilon}^\mu(\mathbf{y}) dV \quad (3.10)$$

we get

$$\frac{1}{V^\mu} \int_{V^\mu} \tilde{\boldsymbol{\varepsilon}}^\mu dV = \mathbf{0} \quad (3.11)$$

and using a general tensor relation<sup>2</sup> we get an expression for the micro displacement fluctuation.

$$\frac{1}{V^\mu} \int_{S^\mu} \tilde{\mathbf{u}}^\mu \otimes_s \mathbf{n} dS = \mathbf{0} \quad (3.12)$$

where  $\mathbf{n}$  is the unit normal vector to the micro domain boundary  $S_\mu$  and  $\mathbf{a} \otimes_s \mathbf{b} \equiv \frac{1}{2}(\mathbf{a} \otimes \mathbf{b} + \mathbf{b} \otimes \mathbf{a})$  is the symmetric tensor product, used because of the relation  $\tilde{\boldsymbol{\varepsilon}}^\mu = \nabla^s \tilde{\mathbf{u}}^\mu$ .

With this restriction in mind, the most simple kinematic conditions for the micro displacement fluctuation are

1. *Taylor assumption or zero fluctuations* (Taylor 1938). This will imply homogeneous deformation in the micro-scale, which will be equal to macro strain,  $\bar{\boldsymbol{\varepsilon}}$ .

$$\tilde{\mathbf{u}}^\mu(\mathbf{y}) = \mathbf{0}, \quad \forall \mathbf{y} \in V^\mu \quad (3.13)$$

where  $V^\mu$  is the micro volume. This model represents an upper bound of the homogenized stiffness, which is also same result from the classic mixing theory (Gruer 2015).

2. *Linear boundary displacements or zero boundary fluctuation*

$$\tilde{\mathbf{u}}^\mu(\mathbf{y}) = \mathbf{0}, \quad \forall \mathbf{y} \in S^\mu \quad (3.14)$$

where  $S^\mu$  is the micro boundary surface. This model was demonstrated to be a restrictive constraint that produces an overestimated homogenized microscopic stiffness (Kaczmarczyk et al. 2008). It yields a conventional BVP with Dirichlet boundary conditions. It is called linear boundary displacement because the micro scale displacement is simply a linear function of the macro strain by means of (3.8).

The other two, *periodic boundary fluctuations* and *minimal constraint* are discussed thoroughly in de Souza Neto and Feijóo (2006), de Souza Neto et al. (2015), and Blanco et al. (2016). The periodic boundary condition has been shown to produce better stiffness estimates for periodic and random microstructure. Whereas the Taylor assumption is the easiest to implement however it does not capture internal fluctuations due heterogeneities.

### 3.4.3. HILL-MANDEL PRINCIPLE

This principle was first proposed by Hill (1963), and later developed in Hill (1972). The Hill-Mandel principle says that the macro-scale *virtual* virtual work must be equal to volume average of micro-scale *virtual* virtual work over the RVE. It establishes the energy consistency between scales and can be stated as,

$$\bar{\boldsymbol{\sigma}} : \dot{\bar{\boldsymbol{\varepsilon}}} \stackrel{\text{def}}{=} \frac{1}{V^\mu} \int_{V^\mu} \boldsymbol{\sigma}^\mu : \dot{\boldsymbol{\varepsilon}}^\mu dV \quad (3.15)$$

the reference to *virtual* means that this equation must hold for any admissible strain field. This statement in the context of the finite element is multiplication of a general test function in the weighted residuals method.

---

<sup>2</sup>General tensor relation from Gurtin (1981),  $\int_V \mathbf{S}(\nabla \mathbf{v})^T dV = \int_S (\mathbf{S}\mathbf{n}) \otimes \mathbf{v} dS - \int_V (\text{div} \mathbf{S}) \otimes \mathbf{v} dV$  with  $\mathbf{S} = \mathbf{I}$ , a general identity tensor, and  $\mathbf{v} = \tilde{\mathbf{u}}^\mu$

This principle has two consequences. The first relates to the micro-macro transition for the stresses and the second to the micro equilibrium equation. In order to better visualize those consequences it is useful to rewrite this principle using the micro displacement split, from eq. (3.9), we get

$$\bar{\boldsymbol{\sigma}} : \dot{\bar{\boldsymbol{\varepsilon}}} \stackrel{\text{def}}{=} \frac{1}{V^\mu} \int_{V^\mu} \boldsymbol{\sigma}^\mu : \dot{\bar{\boldsymbol{\varepsilon}}} dV + \frac{1}{V^\mu} \int_{V^\mu} \boldsymbol{\sigma}^\mu : \dot{\bar{\boldsymbol{\varepsilon}}}^\mu dV \quad (3.16)$$

#### 3.4.4. SCALE TRANSITION FOR THE STRESS

The scale transition for the stresses is a consequence of the Hill-Mandel principle, eq. (3.15). By choosing a virtual micro displacement fluctuation equal to zero,  $\dot{\bar{\mathbf{u}}}^\mu = \mathbf{0}$ ,<sup>3</sup> the Hill-Mandel principle becomes,

$$\bar{\boldsymbol{\sigma}} : \dot{\bar{\boldsymbol{\varepsilon}}} = \frac{1}{V^\mu} \int_{V^\mu} \boldsymbol{\sigma}^\mu : \dot{\bar{\boldsymbol{\varepsilon}}} dV \quad (3.17)$$

therefore, the equation is only satisfied if

$$\bar{\boldsymbol{\sigma}}(\mathbf{x}) \stackrel{\text{def}}{=} \frac{1}{V^\mu} \int_{V^\mu} \boldsymbol{\sigma}^\mu(\mathbf{y}) dV \quad (3.18)$$

It can be shown that the homogenized stress can be expressed in terms of RVE boundary tractions,  $\mathbf{t}(\mathbf{y})$ , and body forces,  $\mathbf{b}(\mathbf{y})$ , (de Souza Neto and Feijóo 2006),

$$\bar{\boldsymbol{\sigma}}(\mathbf{x}) \stackrel{\text{def}}{=} \frac{1}{V^\mu} \left[ \int_{S^\mu} \mathbf{t}(\mathbf{y}) \otimes \mathbf{y} dS - \int_{V^\mu} \mathbf{b}(\mathbf{y}) \otimes \mathbf{y} dV \right] \quad (3.19)$$

#### 3.4.5. EQUILIBRIUM OF THE RVE

Strong form of equilibrium equations at the micro-scale is expressed by

$$\text{div}_{\mathbf{y}} \boldsymbol{\sigma}^\mu + \mathbf{b}(\mathbf{y}) \stackrel{\text{law}}{=} \mathbf{0}, \quad \text{in } V^\mu \quad (3.20)$$

$$\boldsymbol{\sigma}^\mu \mathbf{n} \stackrel{\text{def}}{=} \mathbf{t}(\mathbf{y}) \quad \text{in } S_t^\mu \quad (3.21)$$

using the Principle of Virtual Work,<sup>4</sup>

$$\int_{V^\mu} \boldsymbol{\sigma}^\mu : \nabla_{\mathbf{y}}^s \boldsymbol{\eta} dV - \int_{V^\mu} \mathbf{b}(\mathbf{y}) \cdot \boldsymbol{\eta} dV - \int_{S_t^\mu} \mathbf{t}(\mathbf{y}) \cdot \boldsymbol{\eta} dS = 0, \quad \forall \boldsymbol{\eta} \in \mathcal{V}_\mu \quad (3.22)$$

where  $\boldsymbol{\sigma}^\mu \equiv \boldsymbol{\sigma}^\mu(\mathbf{y})$  is the micro-scale stress,  $\boldsymbol{\eta}$  is a virtual displacement that is in an appropriate set  $\mathcal{V}_\mu$  and  $\nabla_{\mathbf{y}}^s$  is the symmetric gradient operator on the  $\mathbf{y}$  coordinate variable.

The lack of definition of the space  $\mathcal{V}_\mu$  makes the equilibrium problem ill-posed (de Souza Neto and Feijóo 2006). The space  $\mathcal{V}_\mu$  must ensure that the strain average relation between  $\bar{\boldsymbol{\varepsilon}}$  and  $\boldsymbol{\varepsilon}^\mu$ , holds as discussed in the previous section 3.4.2. Once the space is defined, the multi-scale model will yield the macro-scale stress as a function of the macro-scale strain,  $\bar{\boldsymbol{\sigma}} = \bar{\boldsymbol{\sigma}}(\bar{\boldsymbol{\varepsilon}})$ .

Using the Hill-Mandel condition, eq. (3.15) considering a virtual macro strain field equals to zero,  $\dot{\bar{\boldsymbol{\varepsilon}}} = \mathbf{0}$ , and changing notation for the virtual strain field  $\dot{\bar{\boldsymbol{\varepsilon}}}^\mu \equiv \nabla_{\mathbf{y}}^s \boldsymbol{\eta}$ , where  $\boldsymbol{\eta}$  is a general test function, we get as micro equilibrium equation

$$\frac{1}{V^\mu} \int_{V^\mu} \boldsymbol{\sigma}^\mu : \nabla_{\mathbf{y}}^s \boldsymbol{\eta} dV = \mathbf{0} \quad (3.23)$$

<sup>3</sup>Since its a virtual field we can choose any kinematically admissible strain field.

<sup>4</sup>Using the product rule  $\boldsymbol{\sigma} : \nabla_x \boldsymbol{\eta} \stackrel{\text{def}}{=}} \text{div}_x(\boldsymbol{\sigma} \boldsymbol{\eta}) - (\text{div}_x \boldsymbol{\sigma}) \cdot \boldsymbol{\eta}$

This is an important result for multiscale theory. It implies that external load system of the RVE (body force and surface traction) is a *mere reaction to the imposed kinematical constraints* (de Souza Neto and Feijóo 2006; Vaz Júnior et al. 2011).

### 3.4.6. LINEARIZED MICRO-SCALE VIRTUAL WORK EQUATION

In order to solve problems considering material nonlinearity we need an incremental form of the finite element equation. This is obtained by linearizing the weak equilibrium equation at a known point in the direction of a small perturbation in the displacement.

Rewriting considering a general constitutive functional,  $\mathcal{F}^\mu$ , in order to obtain an expression that can be used for material nonlinearity

$$G(\mathbf{u}^\mu, \boldsymbol{\eta}) \stackrel{\text{def}}{=} \int_{V^\mu} \mathcal{F}^\mu : \nabla_y^s \boldsymbol{\eta} dV = 0, \quad \forall \boldsymbol{\eta} \in \mathcal{V}_\mu \quad (3.24)$$

where  $\mathcal{F}^\mu = \mathcal{F}^\mu(\boldsymbol{\varepsilon}^{\mu t})$  is dependent on the strain path but the time superscript is avoided. By linearizing the functional  $G(\mathbf{u}^\mu, \boldsymbol{\eta})$  about a point  $\mathbf{u}_*^\mu$  in a general direction  $\delta \mathbf{u}^\mu$  using the standard procedure shown in appendix A.1, we get

$$G(\mathbf{u}_*^\mu, \boldsymbol{\eta}) + \mathcal{D}G(\mathbf{u}_*^\mu, \boldsymbol{\eta})[\delta \mathbf{u}^\mu] = 0 \quad (3.25)$$

the first term in the left hand side is equal to zero only when the solution satisfies the equilibrium statement in eq. (3.24). The directional derivative can be developed by substituting eq. (3.24) in eq. (3.25), resulting in

$$\int_{V^\mu} \mathcal{D}\mathcal{F}^\mu(\boldsymbol{\varepsilon}_*^\mu)[\nabla_y^s \delta \tilde{\mathbf{u}}^\mu] : \nabla_y^s \boldsymbol{\eta} dV = - \int_{V^\mu} \mathcal{F}^\mu(\boldsymbol{\varepsilon}_*^\mu) : \nabla_y^s \boldsymbol{\eta} dV \quad (3.26)$$

where we can compute the increment in the micro displacement  $\delta \tilde{\mathbf{u}}^\mu$ . Details of this derivation can be found in appendix D.4. In a time discrete form,

$$\int_{V^\mu} \mathbf{D}^\mu : \nabla_y^s \delta \tilde{\mathbf{u}}^\mu : \nabla_y^s \boldsymbol{\eta} dV = - \int_{V^\mu} \hat{\boldsymbol{\sigma}}^\mu(\boldsymbol{\varepsilon}_*^\mu) : \nabla_y^s \boldsymbol{\eta} dV \quad (3.27)$$

where  $\mathbf{D}^\mu$  is the tangent constitutive operator at  $\boldsymbol{\varepsilon}_*^\mu$  and  $\hat{\boldsymbol{\sigma}}^\mu$  is the incremental constitutive function. With the FEM discretization, we need to solve the following system of equations to find the Newton correction for the micro displacement fluctuation

$$\int_{hV^\mu} (\mathbf{B}^g)^T \mathbf{D}^\mu \mathbf{B}^g \delta \tilde{\mathbf{u}}^\mu dV = - \int_{hV^\mu} (\mathbf{B}^g)^T \boldsymbol{\sigma}^\mu dV \quad (3.28)$$

### 3.4.7. HOMOGENIZED CONSTITUTIVE TANGENT OPERATOR

The definition of homogenized constitutive tangent operator is obtained by linearizing the constitutive functional about a specific strain configuration,  $\bar{\boldsymbol{\varepsilon}}_*^t$ , and in a generic strain direction,  $\delta \bar{\boldsymbol{\varepsilon}}$ ,<sup>5</sup>

$$\bar{\mathcal{F}}(\bar{\boldsymbol{\varepsilon}}_*^t + \delta \bar{\boldsymbol{\varepsilon}}) = \bar{\mathcal{F}}(\bar{\boldsymbol{\varepsilon}}_*^t) + \mathcal{D}\bar{\mathcal{F}}(\bar{\boldsymbol{\varepsilon}}_*^t)[\delta \bar{\boldsymbol{\varepsilon}}] \quad (3.29)$$

where the directional derivative defines the tangent relation between the stresses and strains. Notice that the constitutive functional depends on the strain path,  $\bar{\boldsymbol{\varepsilon}}^t$ , whereas the incremental

<sup>5</sup>This direction should not be confused with a virtual strain.

constitutive function,  $\hat{\sigma}$  depends only on the strain of the time increment. Through out the text the time superscript is avoided to keep the notation less cluttered.

For multi-scale constitutive models based on the volume average of micro stress, consequence of Hill-Mandel principle, the homogenized constitutive functional can be defined as

$$\bar{\mathcal{F}}(\bar{\boldsymbol{\varepsilon}}) = \frac{1}{V^\mu} \int_{V^\mu} \mathcal{F}^\mu(\boldsymbol{\varepsilon}^\mu) dV \quad (3.30)$$

which is equivalent to the relation between micro and macro stresses.

By using the definition in eq. (3.29) and eq. (3.30) the homogenized constitutive tangent operator for multi-scale problem can be obtained by taking the derivative of the constitutive functional at a point  $\bar{\boldsymbol{\varepsilon}}_*$  in a general direction  $\delta\bar{\boldsymbol{\varepsilon}}$ , which results in

$$\mathcal{D}\bar{\mathcal{F}}(\bar{\boldsymbol{\varepsilon}}_*)[\delta\bar{\boldsymbol{\varepsilon}}] = \frac{1}{V^\mu} \int_{V^\mu} \mathcal{D}\mathcal{F}^\mu(\boldsymbol{\varepsilon}^\mu)[\delta\bar{\boldsymbol{\varepsilon}}] dV + \frac{1}{V^\mu} \int_{V^\mu} \mathcal{D}\mathcal{F}^\mu(\boldsymbol{\varepsilon}^\mu) [\mathcal{D}\mathcal{G}(\bar{\boldsymbol{\varepsilon}})[\delta\bar{\boldsymbol{\varepsilon}}]] dV \quad (3.31)$$

here the function  $\nabla_y^s \tilde{\boldsymbol{u}} = \mathcal{G}(\bar{\boldsymbol{\varepsilon}})$  relates the micro displacement fluctuations to the macro strains. See appendix D.2 for details on this procedure. After mathematical manipulation the homogenized tangent operator has the following form,

$$\bar{\mathbf{D}} \stackrel{\text{def}}{=} \mathbf{D}_T + \tilde{\mathbf{D}} \quad (3.32)$$

where the first fourth order tensor,  $\mathbf{D}_T$ , is the called Taylor tangent operator and the second,  $\tilde{\mathbf{D}}$ , is the fluctuation contribution. The Taylor contribution is simply the homogenized constitutive operator considering the Taylor assumption, see appendix D.3. The fluctuation contribution depends on the choice of admissible space for the micro displacement fluctuation and it is calculated based on the tangential relation between the macro strain,  $\bar{\boldsymbol{\varepsilon}}$ , and the gradient of micro displacement fluctuation,  $\nabla_y^s \tilde{\boldsymbol{u}}^\mu$  which is discussed in details in appendix D.5.

### 3.5. IMPLEMENTATION CONSIDERATIONS

The multiscale procedure was implemented on top of a standard finite element in its incremental form. The following diagram, fig. 3.4, shows a representation of this scheme. The Increment step represents a load increment for each we seek a converged displacement. The Newton Raphson is a iterative procedure where we get closer and closer to the desired tolerance of the actual solution, when it converges. Next we have a localization procedure in which we loop over each element. Inside the element we are interested in find its internal variables and with that build the element matrices and vectors. The multiscale procedure enters the algorithm inside a macro localization procedure. At this stage we check if the analysis is going to be a multiscale one or a standard state update procedure. If it is multiscale we then start a micro increment followed by a Newton Raphson and a localization through elements in the micro domain. We can see that we are repeating the FEM procedure in the macro localization step.

The procedural paradigm was used in order to perform the multiscale analysis. Object oriented programming was used to encapsulate the material, element and model properties. An element class for instance has the structure shown in fig. 3.5. We have a parent Element class which all new elements can inherit. This class has basic element attributed such as node coordinate, connectivity, material properties and also method to create element matrices and vectors.

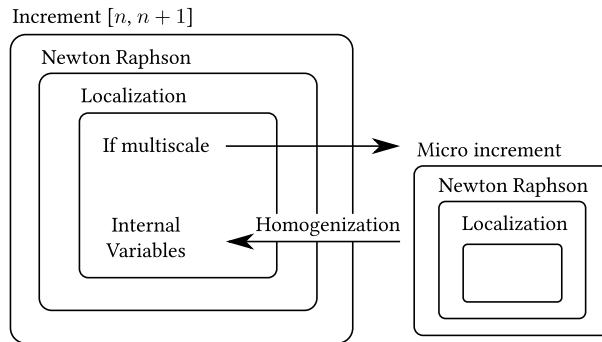


Figure 3.4. Scheme of procedure

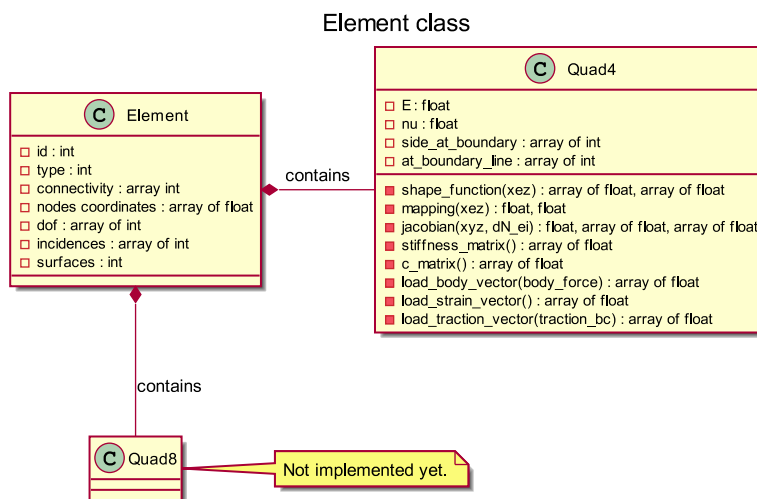


Figure 3.5. Element class attributes and methods

## 4. MULTISCALE SIMULATION OF COMPOSITES

In this section the results obtained with the computer implementation of the numerical method, scikit-mechanics, are presented. The plasticity results are compared to an Abaqus simulation. The multi-scale results are compared with the simulation considering the rule of mixture and fully discretized microstructure models.

### 4.1. PLASTICITY VERIFICATION

The plasticity module verification consists of a single element subject to a load control. The load control test was compared with a simulation using the software Abaqus.

The load control simulation model parameters are shown in fig. 4.1. It consists of a 1 mm square plate with 5 MPa applied in one of the boundaries. Plane strain is assumed and the material properties are shown in table 4.1. The results for the horizontal displacement, for the von Mises equivalent stress,  $q$ , for the equivalent plastic strain,  $\bar{\epsilon}^p$ , and for the stress components are shown in fig. 4.2. We can see that the Skmech (Scikit-Mechanics) results matched exactly the Abaqus results for this example.

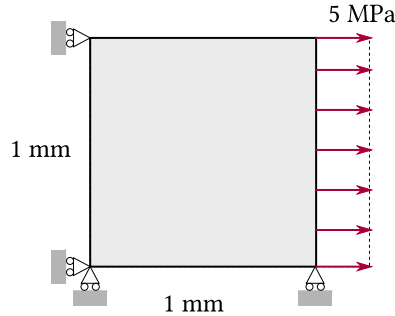


**Figure 4.1.** A single quad element with four integration points. A load step of  $\Delta t = 0.01$  and a residual error tolerance of  $5 \cdot 10^3$ .

**Table 4.1.** Material properties load control problem

$E$	250 GPa
$\nu$	0.25
$\sigma_y$	5 MPa
$H$	50 GPa
$t$	1 mm

### 4.2. MULTISCALE VERIFICATION WITH TAYLOR ASSUMPTION

In this section we verify the multiscale implementation considering the Taylor assumption, in which the macro strain is applied uniformly in the micro domain and there is no internal fluctuations. The model used for this test is presented in fig. 4.3, it consists of a single element with a horizontal traction applied on the right boundary.

This test was performed for three different microstructures. The first with a circular reinforcement with greater elastic modulus and the same other material parameters as the matrix. The second a circular reinforcement with greater elastic modulus, yield stress and hardening modulus. The third with a circular void. All of them with reinforcement and void

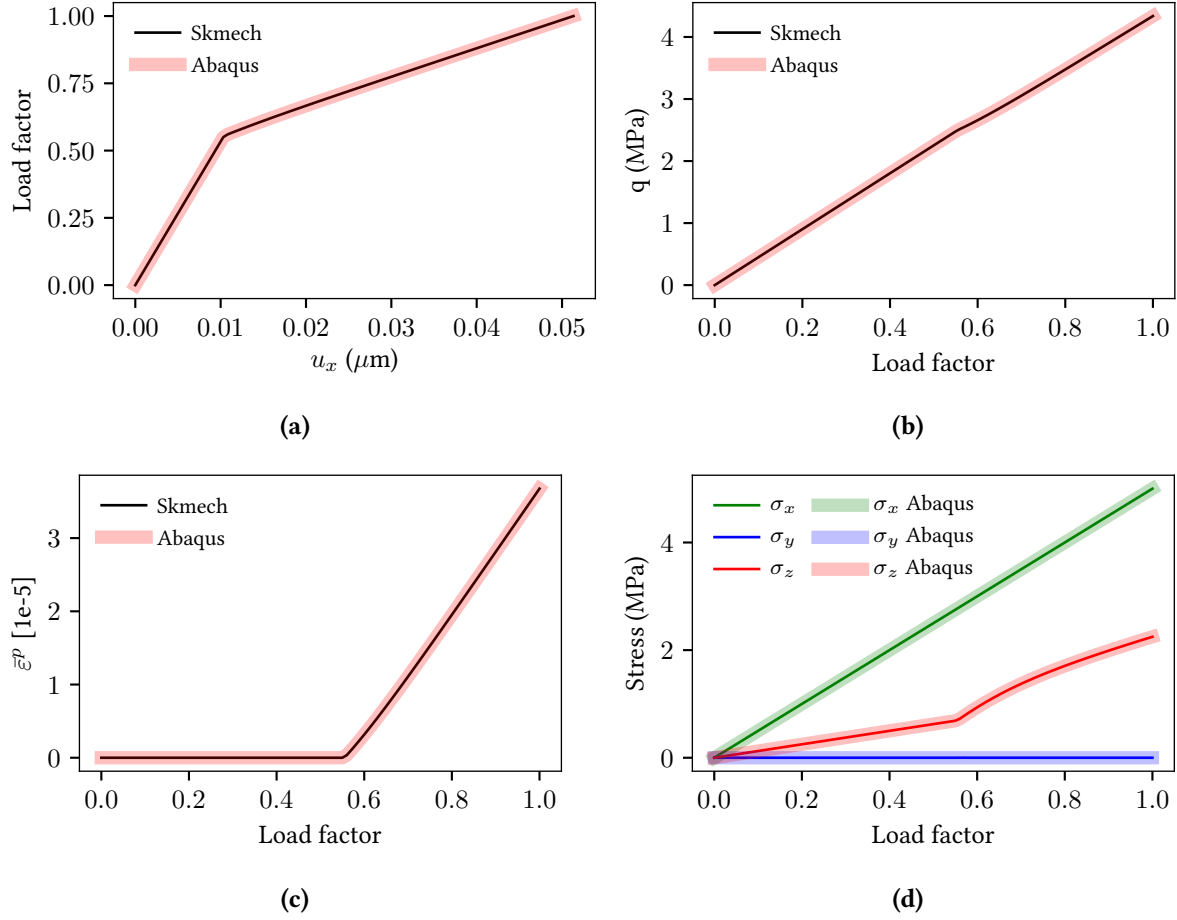


**Figure 4.2.** Comparison between scikit-mechanics and ABAQUS, (a) the tip displacement, (b) the effective von Mises stress, (c) the equivalent plastic strain and (d) the other stresses components.

ratio of 23.56%. In every analysis the homogeneous problem is plotted as a reference. The multiscale analysis is compared with the standard analysis considering the rule of mixture for the material parameters.

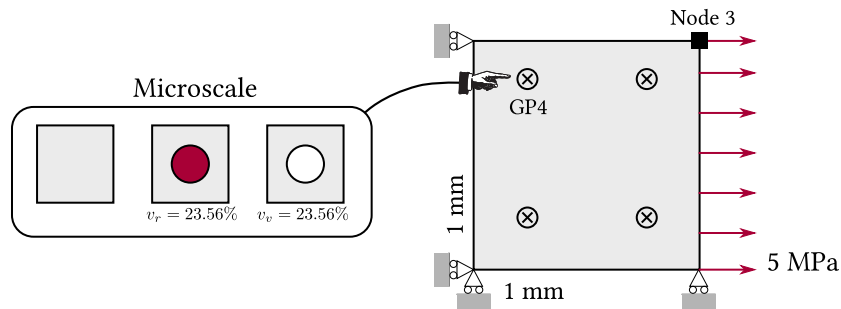


**Figure 4.3.** Different micro structure model

The rule of mixture expressions to approximate the effective material properties of heterogeneous media, (Callister 2007). Those expressions are going to be useful when checking the multiscale analysis. The upper and lower bound are given by,

$$E_{eff}^{upp} = E_m v_m + E_r v_r \quad \text{and} \quad E_{eff}^{low} = \frac{E_m E_r}{v_m E_r + v_r E_m} \quad (4.1)$$

where  $E_m$  is the elastic modulus of the matrix material,  $E_r$  the elastic modulus of the reinforcement material,  $v_r$  and  $v_m$  are the volume fraction of the reinforcement and matrix materials.

#### 4.2.1. REINFORCEMENT WITH STIFFER ELASTIC MODULUS

In this example the reinforcement has stiffer elastic modulus than the matrix, 8 times greater. However the other material parameters are the same. Table 4.2 shows the material parameters used in the analysis.

The goal with this test is to compare the multiscale analysis with the rule of mixture results when they are applied only to the elastic modulus. All analysis were run in the implemented code skmech, only the homogeneous analysis was performed also using abaqus.

**Table 4.2.** Material properties problem with stiffer elastic modulus

	Matrix	Reinforcement
$E$	250 GPa	2000 GPa
$\nu$	0.25	0.25
$\sigma_y$	2.5 MPa	2.5 MPa
$H$	50 GPa	50 GPa
$t$	1 mm	1mm

We can see from fig. 4.4 that when there is no reinforcement the multiscale analysis (MS) results the same as the previous direct incremental analysis. When reinforcement is added we notice the decrease in the tip displacement resulted from a stiffer model. We also notice two changes in inclination of the load-displacement curve. The first one marks the yielding on the reinforcement, which can be seen in the equivalent plastic strain field at point A in fig. 4.4.

In regards the micro scale fields with the Taylor assumption, we should expect homogeneous distribution of the fields in the different materials. This happens because in the Taylor assumption the macro strain field is applied uniformly in the micro domain. However in the fields shown in fig. 4.4 we see that they are not homogeneous. The explanation for that is because when interpolating the field from the Gauss point to the nodes and smoothing them out by a simple element average we get intermediary values.

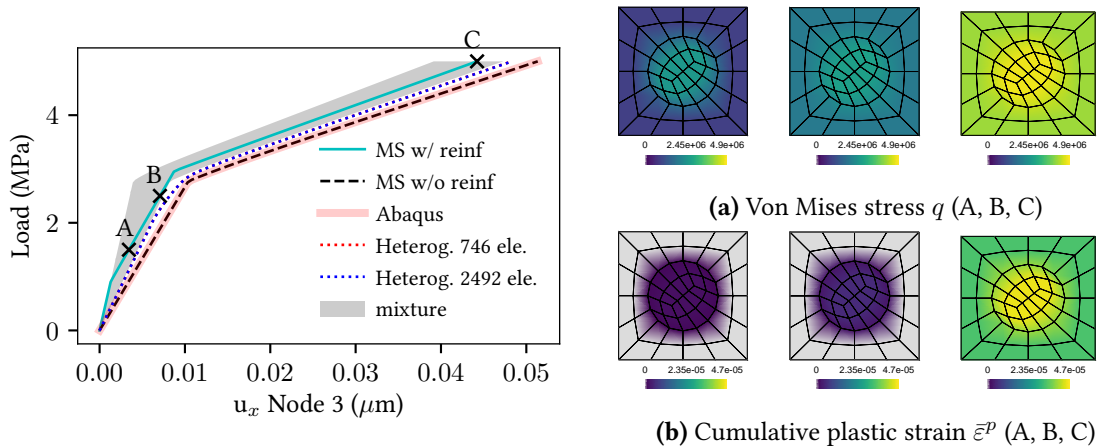


**Figure 4.4.** Displacement load curve solved and microstructure fields at GP4 considering microstructure with stiffer reinforcement.

### 4.2.2. REINFORCEMENT WITH HIGHER YIELD STRESS

This example consists of the same macro structure from the previous example, single square element, and a microstructure with a stiffer reinforcement and greater yield stress and hardening modulus. The material properties are shown in table 4.3.

**Table 4.3.** Material properties problem with higher yield stress

	Matrix	Reinforcement
$E$	250 GPa	2000 GPa
$\nu$	0.25	0.25
$\sigma_y$	2.5 MPa	10 MPa
$H$	50 GPa	200 GPa

We expect with this example to produce a stiffer structure. And because the reinforcement has a higher elastic modulus it will absorb most of the stress inside the microstructure. We can see the von Mises stress distribution in the microstructure in fig. 4.5. At the last load increment we notice that only the reinforcement developed stress greater than the yield limit and the matrix has not yielded. From the load-displacement curve we notice only change in the inclination which marks the point where the reinforcement yields. The rule of mixture results, represented with the gray area, mark a wide interval where the heterogeneous material response may lie. The wide range is explained due to the large difference in the yield stress and hardening modulus of both materials, the reinforcement is 4 times larger.

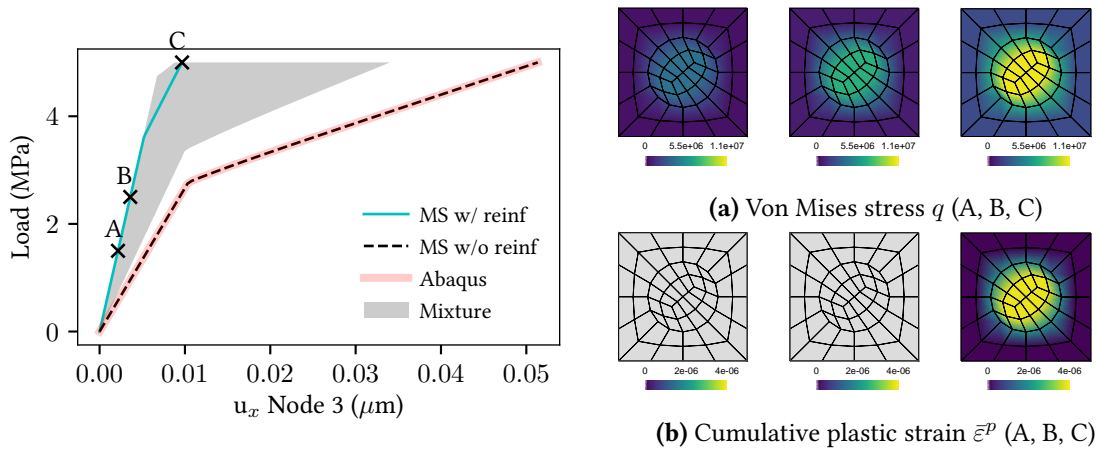


**Figure 4.5.** Displacement load curve solved and microstructure fields considering microstructure with stiffer and larger yield strength reinforcement.

### 4.2.3. MICROSTRUCTURE WITH A VOID

This example consists of the same single macro element with a circular void micro domain. The material properties for the matrix is the same as before and it is presented in table 4.4.

The void fraction is the same as the reinforcement used in the previous sections,  $v_v = 23.56\%$ . Because we are removing material from the structure we expect it to behave less stiff than the previous analysis. Figure 4.6 shows the load-displacement curve and the microstructure fields at three different load increments. We can see that in this case the curve is below the

**Table 4.4.** Material properties problem with a hole

Matrix	
$E$	250 GPa
$\nu$	0.25
$\sigma_y$	2.5 MPa
$H$	50 GPa

homogeneous case, performed in abaqus and skmech (MS w/o reinf), which represents a larger displacement as expected.

The microstructure fields are homogeneous because of the Taylor assumption. At point A we still in the linear regime and the microstructure did not yield, as we can see from the equivalent plastic strain field. The multiscale result with a hole matched exactly the result obtained using the rule of mixture formular and a standard FEM analysis.

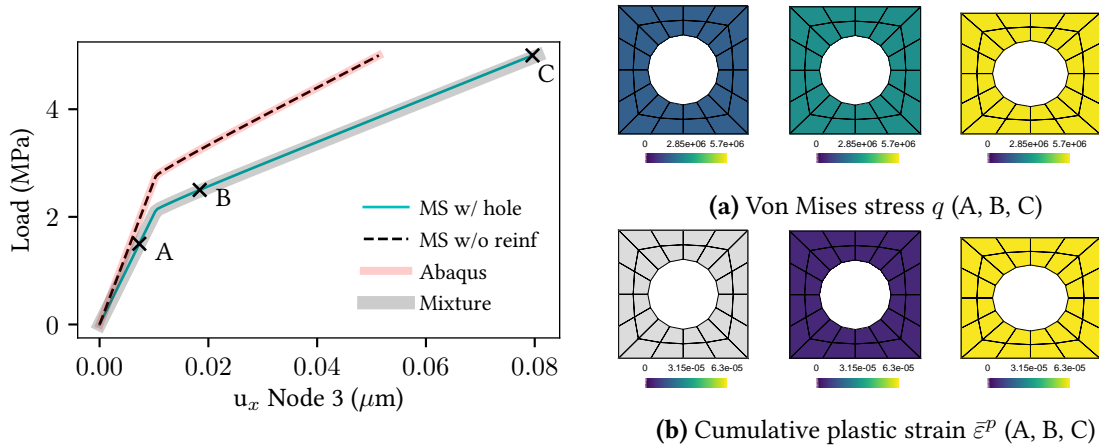


**Figure 4.6.** Displacement load curve solved and microstructure fields at GP4 considering microstructure with hole.

### 4.3. FURTHER COMPOSITE ANALYSIS

This section explores different aspects of the multiscale analysis. First we test the two RVE boundary condition assumptions, Taylor and Linear. Next we analyze the effect of the inclusion scale on the overall response.

#### 4.3.1. DIFFERENT RVE BOUNDARY CONDITION ASSUMPTIONS

In this section we will test the different RVE boundary condition assumption. Specifically, the Taylor and the linear boundary condition assumptions. The model used for this test is shown in fig. 4.7, again a single element with fixed bottom and left sides and with a shear traction applied on the top and right sides. The microstructure considered is a square with a square hole so we can better visualize the displacement fluctuations inside of it. The material parameters are shown in table 4.5.

The analysis considers a nonlinear material, the load increment-displacement curve is plotted in fig. 4.8. The fields in the gauss point 3, see fig. 4.9, for three different load increments are also plotted. We can see from the curves that the Taylor assumption for the RVE matches the rule of

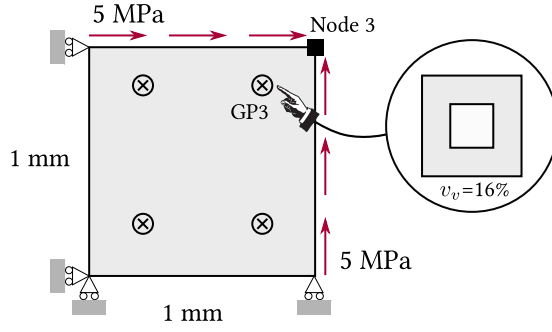


**Figure 4.7.** One element model with square voids in the microstructure

**Table 4.5.** Material properties for example with different RVE boundary assumption

Matrix	
$E$	250 GPa
$\nu$	0.25
$\sigma_y$	2.5 MPa
$H$	50 GPa

mixture results which consider the elastic module of the material fraction occupied by the matrix, further explained in the next sessions. We can also see that the Taylor assumption produces a stiffer model, with less displacement. This happens because the interactions, fluctuations due the square hole, inside the miscro structure are not considered. Whereas when the linear assumption is considered, the square hole affects the homogenized parameters producing a less stiff model. Notice that the micro fields, equivalent plastic strain, are homogeneous in the Taylor model, and that they fluctuate when the linear boundary condition model is considered.

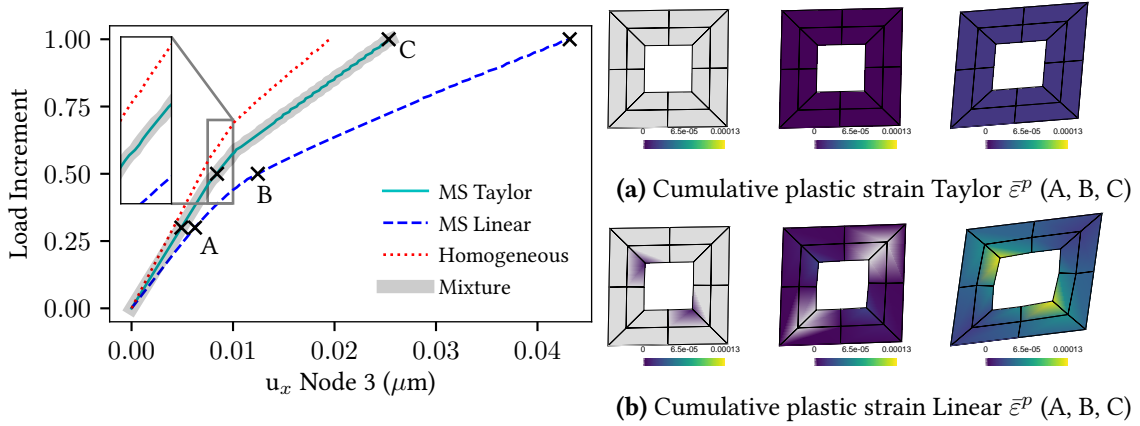


**Figure 4.8.** Displacement load curve solved and microstructure fields at GP3 considering microstructure with a square hole.

#### 4.4. DIFFERENT SCALE EFFECT

In this section we explore the effect of different microstructure scales. The model used is slab with circular inclusions, shown in fig. 4.9, with restrict displacements on the left, top and bottom. The slab is only allowed to deform in the horizontal direction. There is a uniform traction applied on the left side. The microstructure has a reinforcement ratio of 23.56% which

gives a ratio between diameter and length of 27.38%. We restricted this test to the linear case in order to avoid larger processing time when simulating the fully discretized domain (which considers the microstructure).

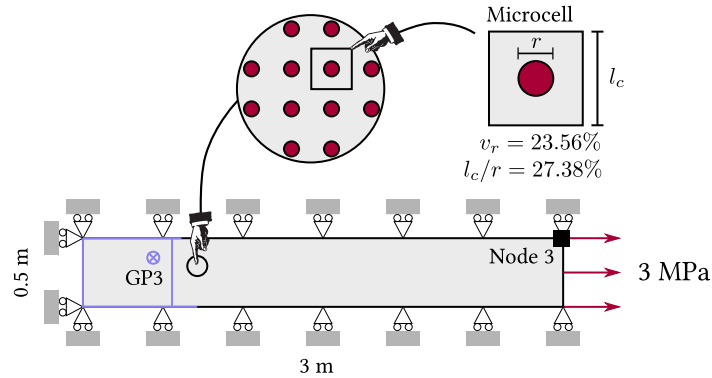


**Figure 4.9.** Slab model with boundary conditions for multiscale analysis

The reinforcement has a higher stiffness than the matrix, ten times higher. The other material parameters are the same and they are shown in table 4.6.

**Table 4.6.** Material properties example with different scales

	Matrix	Reinforcement
$E$	20 GPa	200 GPa
$\nu$	0.25	0.25
$\sigma_y$	2.5 MPa	2.5 MPa
$H$	50 GPa	50 GPa

This test will explore the effect of the distribution of the material through the macro domain. We expect that as we increase the number of reinforcement inclusions we approach the rule of mixture results, which is equivalent to using the Taylor assumption in the RVE.

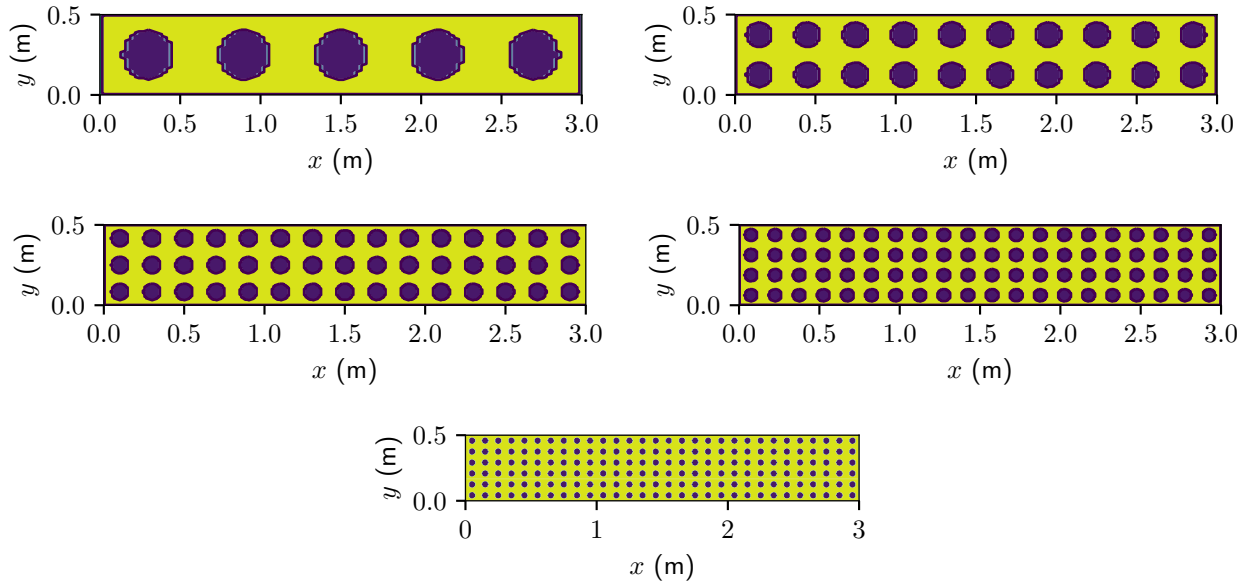
Effect of scale difference between micro and macro length represented by different number of inclusions but with the *same reinforcement ratio*. Figure 4.10 shows the different models tested. We started with only five inclusions with 0.3 m of diameter, which yields 23.56% reinforcement ratio, and increased the number of inclusions while keeping the same ratio. The next four models have respectively 20, 45, 80 and 180 inclusion. In this analysis we opted for using the XFEM module in order to automate the creation of different models with different number of inclusions with different radius. Using the python programming language we defined a function in which the zero level set is the inclusion boundaries<sup>6</sup>.

Figure 4.11 shows the tip displacement of the models considering different inclusions number as we increase the number of degree's of freedom. We can clearly see that the tip displacement decreases as we increase the number of inclusions. The shaded band mark the

<sup>6</sup>This function was created by summing boolean expressions that define each hole in a particular cell. Those boolean expression are simply,

$$\text{micro\_domains}+ = ((x > x_c - d_x)(x < x_c + d_x)(y > y_c - d_y)(y < y_c + d_y)((x - x_c)^2 + (y - y_c)^2 - r^2)) \quad (4.2)$$

where  $(x_c, y_c)$  is the inclusion center,  $r$  the inclusion radius and  $d_x, d_y$  define the micro cell. Then, for each micro cell we compute if a point  $(x, y)$  is inside or outside the inclusion using the circle equation. If it is inside the expression will be negative and if it is outside, positive. The zero level set will define the inclusion boundaries.



**Figure 4.10.** Model with different number of inclusion (5, 20, 45, 80, 180) but with same reinforcement volume ratio of 23.56%.

ruled of mixture lower and upper limit. Notice that the more inclusion we have the more we get close to the lower limit. This lower limit is obtained using the first expression in eq. (4.1) which represents a volumetric average.

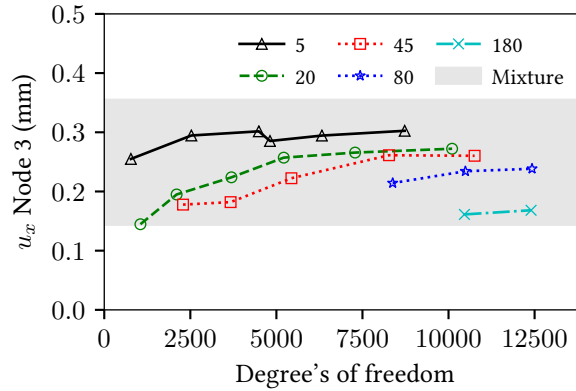


**Figure 4.11.** Tip displacement as we increase the number of degree's of freedom for models with different number of inclusions but same reinforcement volume ratio.

We can see in fig. 4.12 that increasing the number of inclusion, and keeping the same reinforcement ratio, makes the structure stiffer which reduces the displacement. This happens because we are spreading the stiffer material evenly throughout the geometry. The multi scale simulation considering the Taylor assumption matches the result obtained with the rule of mixtures, which can be seen as the lower limit in the fig. 4.12. The multiscale analysis considering Linear assumption takes into account fluctuations inside the microstructure, which results in a less stiff structure.

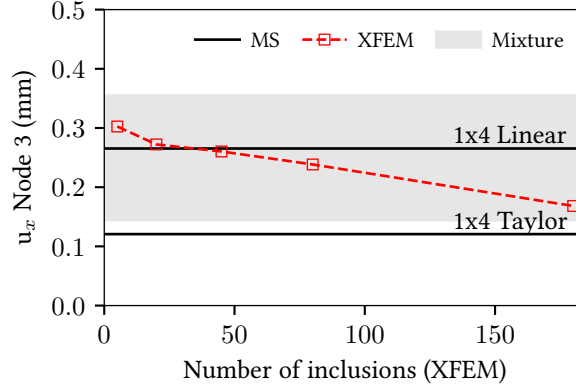


**Figure 4.12.** Converged displacement at node 3 (fig. 4.9) we increase the number of inclusions keeping the same reinforcement volume ratio of 23.56% and the multi scale result.

#### 4.5. PERFORATED PLATE

We now focus on testing the multiscale procedure for nonlinear problems. A similar study was done in Matsui et al. (2004) but with a different kind of microstructure and without fully discretized model.

This test consists of a notched rod which after symmetry arguments is reduced to the model shown in fig. 4.13. The micro scale consists of a periodic distributed circular voids, volumetric fraction of the voids is 12.56%. Uniform load is applied at the top.

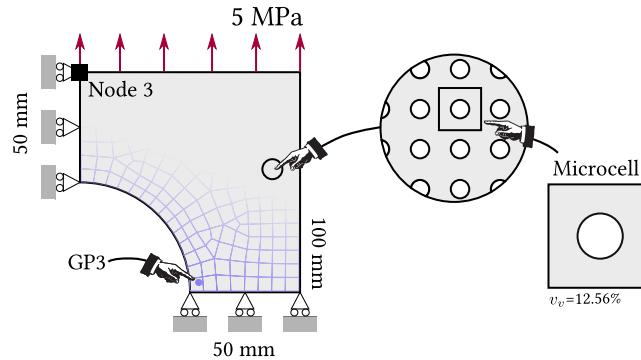


**Figure 4.13.** Perforated plate model

The material properties considered for the nonlinear analysis are expressed in table 4.7. and Plane strain is considered together with von Mises yielding criteria and isotropic hardening.

**Table 4.7.** Material properties for notched plate

Matrix	
$E$	100 GPa
$\nu$	0.15
$\sigma_y$	10 MPa
$H$	20 GPa

Figure 4.14 shows the load-displacement curve. The displacement considered was from node 3, see fig. 4.13. The homogeneous case was also simulated in order to give a reference

to the multiscale result. For the homogeneous domain we run it in three different ways. The first one was the standard incremental FEM implemented, the second from Abaqus and the third the implemented multiscale considering homogeneous micro cell. We can see that they match closely with the Abaqus result. The standard FEM procedure has 1328 elements whereas in the multiscale we used 203 elements. The mesh for the standard analysis was chosen by comparing the error relative with the Abaqus result and the mesh choice for the macro scale took in consideration the rule of mixture result. Even though we used less elements in the multiscale analysis it took longer, 5.2 hours, whereas the standard analysis took 10 minutes, i.e. 30 times more.

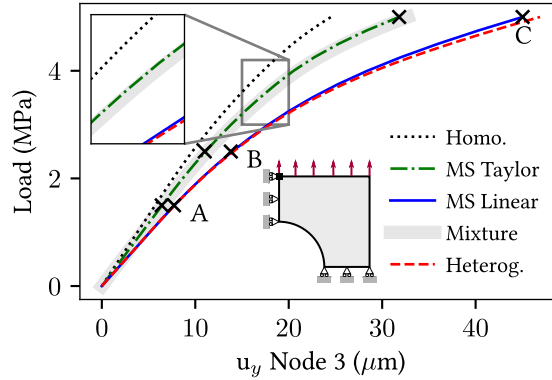


**Figure 4.14.** Tip displacement of perforated plate Heterogeneous with 12x12 hole grid (see fig. 4.17 d) and Multiscale (MS) with 203 elements (see fig. 4.16 b and c)

The multiscale analysis considering the Taylor assumption was then performed with 224 elements in the macro scale and 128 elements in the micro scale. This simulation took 28.6 hours (i5 1.90GHz 8GB RAM). The result of this simulation should match the standard analysis considering effective properties with rule of mixtures. We can see in the plot, fig. 4.14, that the curves are fairly close. The average error between the multiscale simulation with linear boundary displacement assumption (MS Linear) and the heterogeneous fully discretized model are shown in the Table 4.8 below,

**Table 4.8.** Average error between MS linear and heterogeneous analysis.

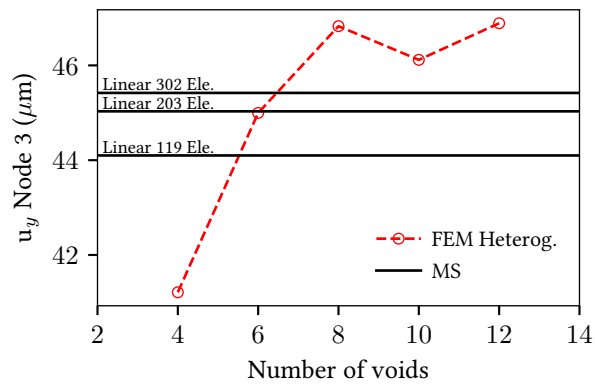
Average error	1.43%
Maximum error	3.96%
RMSE	$7.01 \cdot 10^{-7}$

The simulation considering the linear boundary condition for the RVE, no micro displacement fluctuation in the boundary, is also performed with 203 macro elements and 128 micro elements. Comparing the processing time, the MS Linear with 203 macro elements and 128 micro elements took twice the processing time of the heterogeneous model fully discretized with 15816 quad elements. This happens because the multiscale implementation is not using parallelization and it is used on all elements even in the elastic case. Therefore there still room for great improvement in performance time. As we expected from this RVE boundary condition assumption we get a less stiff model when it is considered. This happens because a non homogeneous stress distribution produce a non homogeneous plastic behavior.

We also notice that the linear displacement boundary condition assumption for the RVE generates a stiffer model, or upper bound, for the multiscale analysis. The literature report

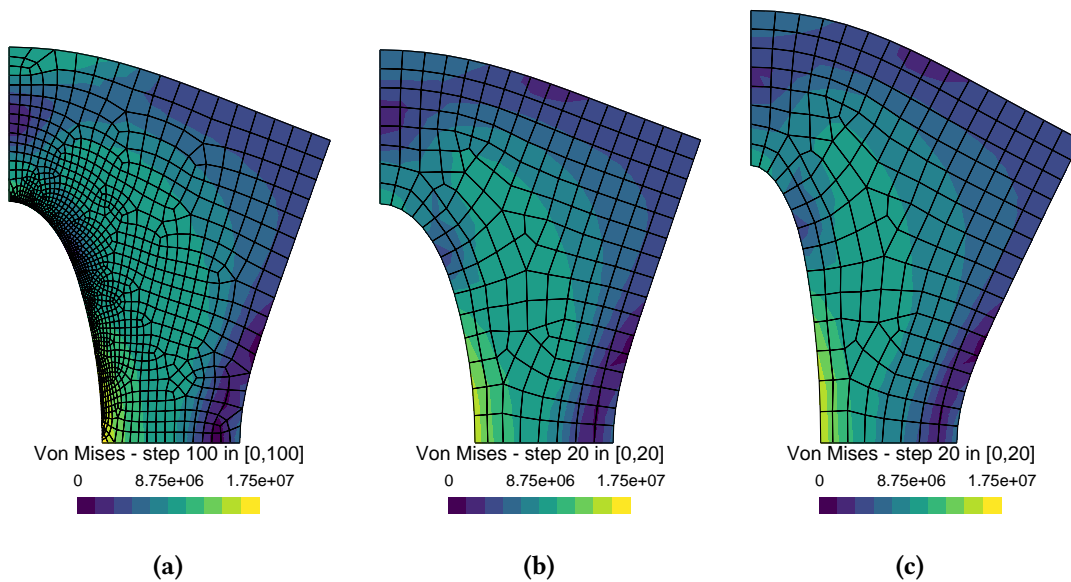
that this occur generally and the lower bound is obtained using the periodic displacement boundary condition for the RVE. (Hollister and Kikuchi 1992; Nemat-Nasser et al. 1993; Hori and Nemat-Nasser 1999; Miehe and Koch 2002; Kanit et al. 2003; de Souza Neto and Feijóo 2006)

Figure 4.15 shows the comparison between the standard analysis in the fully discretized heterogeneous model and the multiscale. The parameter is the tip displacement at node 3 in the last load step. We can see that as we increase the number of voids we approach the multiscale considering the linear boundary condition assumption for the RVE.



**Figure 4.15.** Evolution of tip displacement of perforated plate in the fully discretized simulation considering different number of voids and comparison with the multiscale simulation with different RVE boundary condition assumption and number of elements.

The von Mises stress for the multiscale analysis and the mixture one are shown in fig. 4.16. We can notice from the figure the number of elements used on each analysis. The standard FEM considering rule of mixtures with 1328 quad elements and the multiscale with 203 elements. Those figures also show the deformed shape scaled by a 1000 times.



**Figure 4.16.** Von Mises stress for standard and multiscale analysis of heterogeneous material. In (a) model using standard mixture theory, (b) considering the Taylor assumption and (c) considering linear displacement assumption.

In order to verify the accuracy of the multiscale analysis considering linear displacement

boundary condition in the RVE we use a fully discretized model. The fully discretized model consists of the perforated plate with small holes in its domain. In the test we gradually increase the number of the holes in a grid  $N \times N$ . The different models used and the respective number of elements are shown in fig. 4.17. The models tested have respectively 6, 8, 10 and 12 holes in a grid  $N \times N$ . We notice from the results of the vertical displacement of node 3, in fig. 4.15, as we increase the number of holes in the structure the overall response is more flexible. This occurs because the stress concentration at the holes, specially in the bottom row, produce plastic response that increases the vertical elongation. From the plot we can see that the multiscale analysis considering the linear displacement boundary condition approaches the result of the fully discretized model as we increase the number of macro elements.

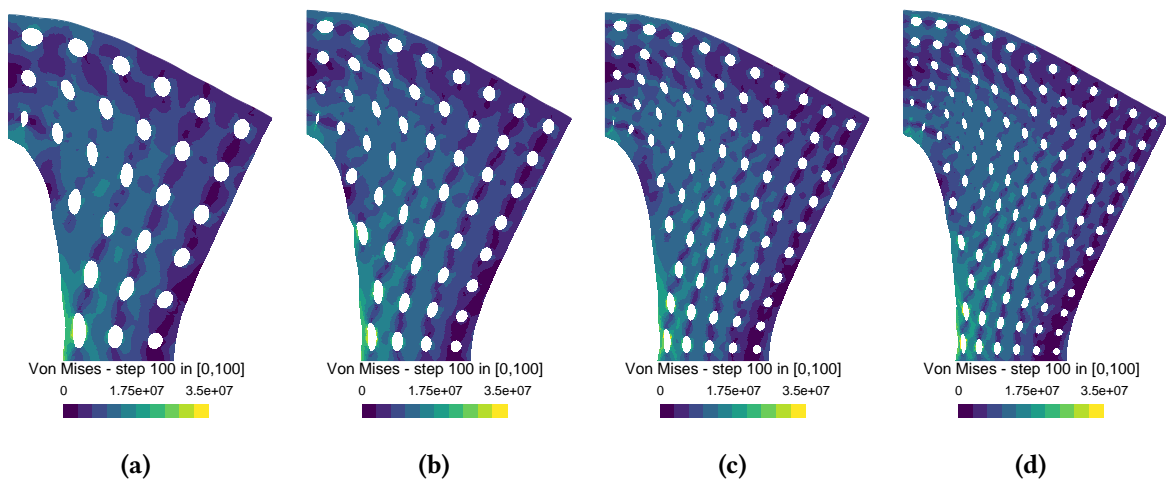


**Figure 4.17.** Von Mises stress for full discretized model with different number  $N$  of voids in a grid  $N \times N$ . Model (a) with a hole grid of 6 perforations and 3168 elements, (b) with a grid of 8 and 6708 elements, (c) with a grid of 10 and 10466 elements and (d) a grid of 12 and 15816 elements.

Figure 4.18 shows the micro scale von Mises stress and the equivalent plastic strain field at three different instants, (A, B, C) from fig. 4.14. We can notice the homogeneous distribution when the Taylor assumption is considered and the non-homogeneous distribution when the internal fluctuations are considered. Notice that when the linear boundary condition of the RVE is considered the section presents plastic behavior earlier.

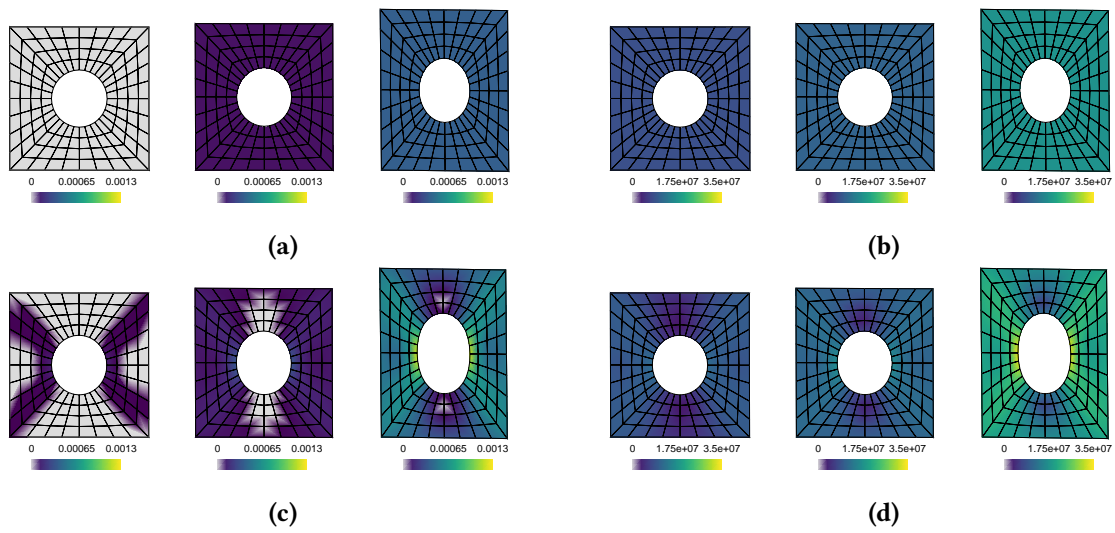


**Figure 4.18.** Micro cell fields for Taylor and linear assumptions at the gauss point 3 (fig. 4.13). In (a) and (c) the  $\bar{\varepsilon}^p$  considering Taylor and Linear boundary displacement assumptions respectively; and (b) and (d) with von Mises stress,  $q$ , considering Taylor and Linear boundary displacement assumptions respectively. Each set of fields is correspondent to the instants A, B, C (fig.4.14)

## 5. MULTISCALE SIMULATION OF CANCELLOUS BONE OF HUMAN FEMUR

In this example we explore the multiscale procedure to model the proximal part of human femur. The typical structure of long bones consists of a cylindrical shaft called *diaphysis* and two rounded ends called *epiphysis*. The diaphysis is composed mainly of cortical bone whereas the epiphysis contains mostly cancellous bone. Cortical bone is a solid mass with microscopic channels. The human skeleton mass is formed by approximately 80% of cortical bone. The other 20% is cancellous bone, found in inner parts of bones. Cortical bone main role is to support and protect the skeleton therefore it has low porosity. Cancellous bone function is mainly mineral homeostasis and also supportive. Figure 5.1 shows the proximal end of the human femur cross section and a radiograph. More details about bone morphology can be found in (Cowin 2001).

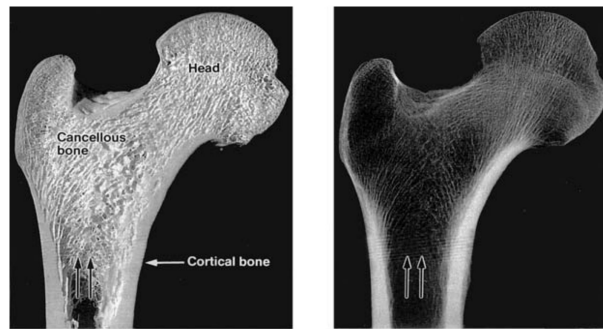


Figure 5.1. Femur section and radiograph image (Cowin 2001).

The model used in this example is shown in fig. 5.2. Our goal with this analysis is to test the effect of different microstructure void ratios and its distribution. Four different microstructure were tested, two with 30% void fraction and two with 60%. In regards the void distribution we tested a micro domain with only a single circular void and one with multiple ellipses and circular voids, referred hereafter as *multiple ellipses* only. Another analysis is performed comparing the multiscale results with a standard finite element procedure using an effective isotropic elastic modulus from a single RVE analysis.

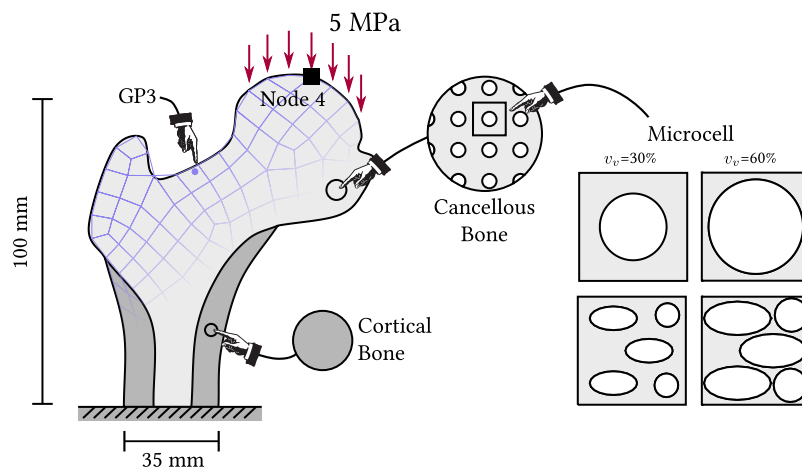


Figure 5.2. Femur model and micro model.

Different from the previous examples, the macro model used in this analysis is separated in two parts: one where multiscale is performed and the other with standard finite element. The

standard part is used to model the homogeneous cortical bone whereas the multiscale is used to model the cancellous bone with its high porosity. Table 5.1 shows the material properties used which were based on the work of Wolfram and Schwiedrzik (2016).

**Table 5.1.** Material properties for femur example

Matrix	
$E$	20 GPa
$\nu$	0.3
$\sigma_y$	50 MPa
$H$	20 GPa

The results for the displacement at node 4, see Fig. 5.2, are shown in the Fig. 5.3 bellow. On the left, fig. 5.3a, we have the comparison between the different microstructure and different void volume fraction. We can see noticeable difference on the response of the structure depending on its microstructure arrangement.

The RVE with 30% void fraction presented a elastic response. And the difference between the two microstructure arrangement, single circle and multiple voids, was smaller. When the void fraction increased to 60% the bone response was nonlinear. The effect of the RVE void arrangement is significant, the micro structure with multiple voids is much more flexible than the single circle micro structure.

The microstructure with multiple ellipses voids produced a more flexible model and we can conclude that the larger the void fraction the greater is the difference compared with a single circle void. This is mainly because the larger the void fraction the micro structure with multiple ellipses voids produce a model with weak spots which are points subjected to stress concentrations and plastification as consequence.

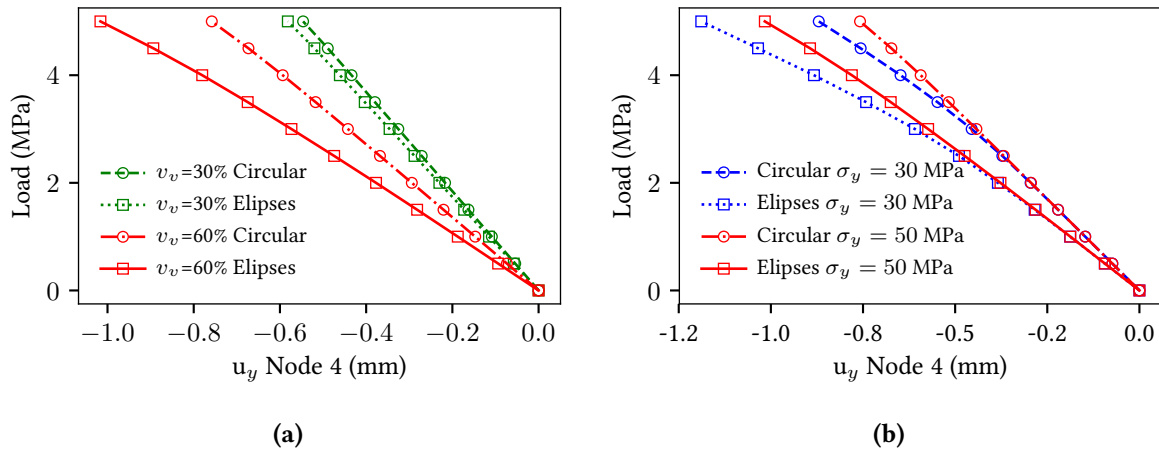


**Figure 5.3.** Displacement at node 4 for a multiscale analysis considering a macro mesh of 102 elements and 4 different micro models,  $v_v = 30\%$ ,  $v_v = 60\%$  each fraction with a single circle and multiple voids. (a) for a load of 2.5 MPa in an elastic domain and (b) for a load of 5 MPa with a plastic domain.

Figure 5.3b shows the vertical displacement at node 4 for the model with void fraction of 60%, however we changed the plastic property of the bone to a yield stress of 30 MPa instead of 50 MPa. As expected, the smaller yield stress resulted in greater deformation. The difference between the two RVE micro structure configuration kept the same, the model with multiple

voids deformed more than the model with a single circle void. The deformed macro model is shown in Fig. 5.4, we notice a similar stress distribution when using both micro structures.

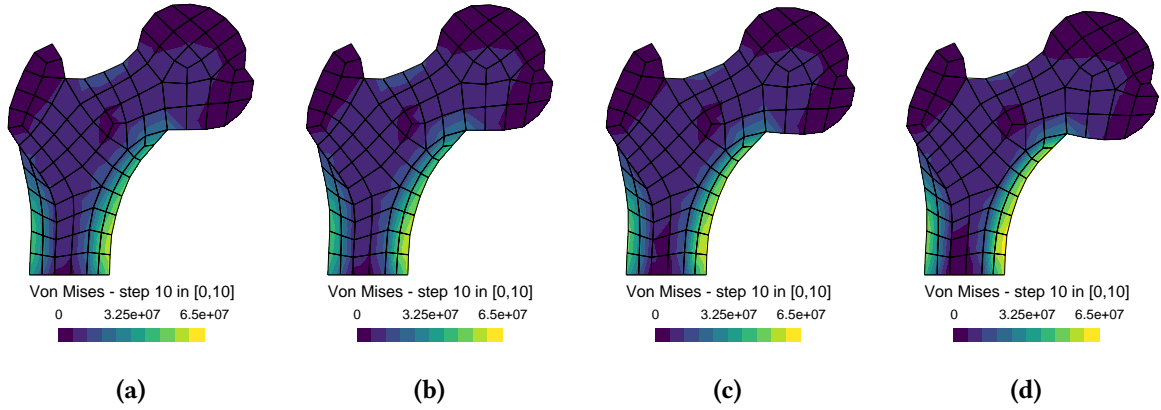


**Figure 5.4.** Von mises stress in the macro domain deformed shape scaled 10x for different micro structures with a 5 MPa load. In (a) with  $V_v = 30\%$  Circle, (b)  $V_v = 30\%$  Ellipses, (c)  $V_v = 60\%$  Circle and (d)  $V_v = 60\%$  Ellipses.

From the von Mises equivalent stress distribution we can notice the most solicited areas are concentrated in the femoral shaft due the moment arm generated by the vertical load. This region is formed by the denser bone which can better resist to the load. In the cancelous bone the most solicited area is in the neck region, which is in between the head and the greater trochanter.

Figure 5.5 shows the equivalent plastic strain for the model with 30% void ration and for the model with 60%. We can see that the model with more voids is more flexible due the plastification of the section areas where stresses concentrate.

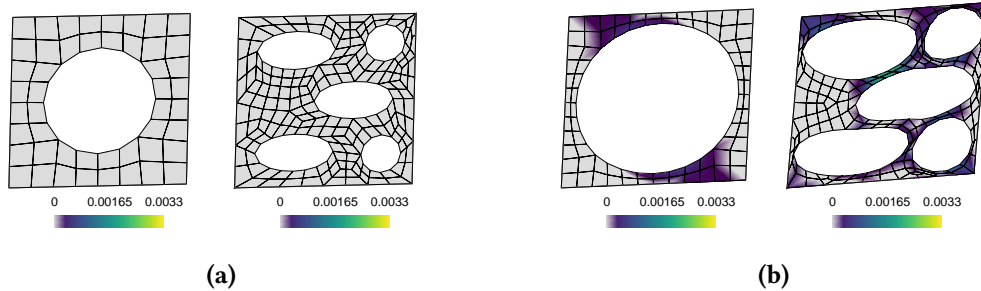


**Figure 5.5.** Equivalent plastic strain in the micro domain deformed shape scaled 30x referent to GP3 shown in fig. 5.2. In (a)  $V_v = 30\%$  and (b)  $V_v = 60\%$

The equivalent plastic strain for the microstructure in the model with 60% void ratio and two different yield stress  $\sigma_y = 50$  MPa and 30 MPa are shown in fig. 5.6. We can see that the model with smaller yield stress the plastification of the section was greater than the model with larger yield stress.

Next we compare the multiscale results with an analysis made with an effective isotropic elastic modulus obtained by using a single microstructure model. The effective elastic modulus is computed by applying a uniform strain in the microstructure within the elastic range, then compute the stress response and average that over the domain, finally we use the plane strain stress-strain relation to calculate the elastic modulus for a known poisson ratio.

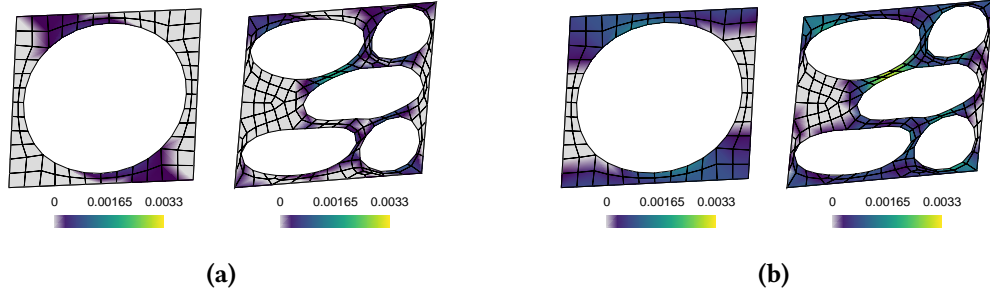


**Figure 5.6.** Equivalent plastic strain in the micro domain deformed shape scaled 30x referent to GP3 shown in fig. 5.2. In (a)  $V_v = 60\%$  5 MPa  $\sigma_y = 50$  MPa and (b)  $V_v = 60\%$  5 MPa  $\sigma_y = 30$  MPa

From Fig. 5.7 we can see that the micro structure configuration considerably affect the effective elastic modulus obtained by applying a known macro strain. The microstructure with multiple ellipses voids has a stiffer response in the x-direction than in the y-direction, 5.7b. This occurs because of the geometric characteristic of ellipses which has greater strength in the major axis direction. When we apply a shear strain in the micro structure we get an effective elastic modulus that produces a response that closely match the multiscale analysis.

When the circular void microstructure is considered we get an isotropic response. This happens due symmetry of the micro structure model. All directions produce the same response. Again we observe that when we use the effective elastic modulus from the shear perturbation we get a better approximation to the multiscale analysis. Both homogeneous analysis fail to capture the localized plastification phenomena which is accounted when a multiscale analysis is used.

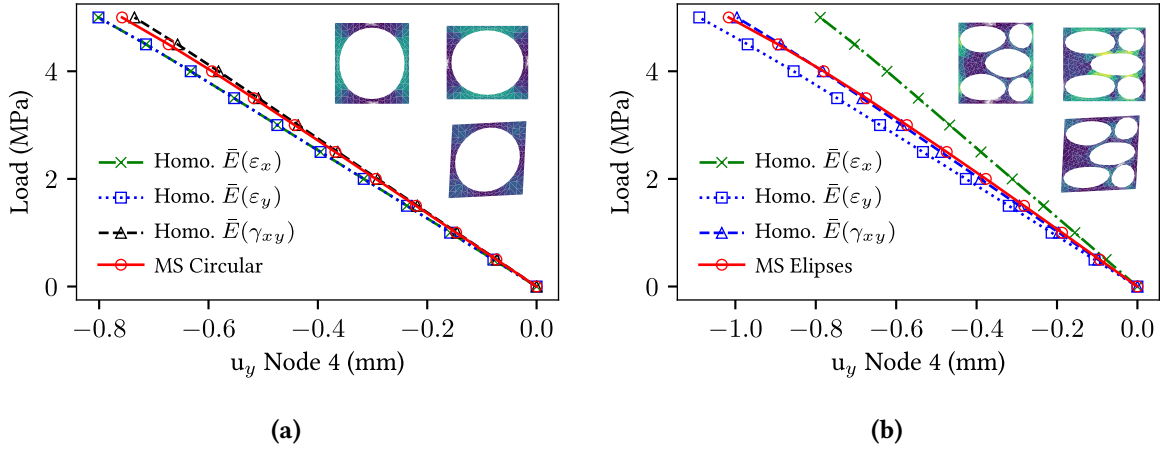


**Figure 5.7.** Comparison between multiscale (MS) analysis and a standard analysis with an effective isotropic elastic modulus,  $\bar{E}$ , obtained by applying a known strain,  $\epsilon = [\epsilon_x, 0, 0]$ ,  $[0, \epsilon_y, 0]$ ,  $[0, 0, \gamma_{xy}]$ , into the microstructure. In (a) the circular microstructure and (b) the multiple ellipses.

Figure 5.8 shows the deformed shape and the von Mises stress distribution of the single microstructure where the uniform strain is applied. Each strain component is applied separately. We notice that the response of the micro structure when only shear strain is applied is similar to the RVE representing the gauss point in the neck region of the femur, see fig. 5.2. This can be an explanation for why the effective elastic modulus obtained from the shear strain

perturbation resulted in a closer response to the multiscale analysis. The gauss point is subject to a strain state with a dominance of shear strain and the strength of the neck region is the most responsible for the node 4 vertical displacement.

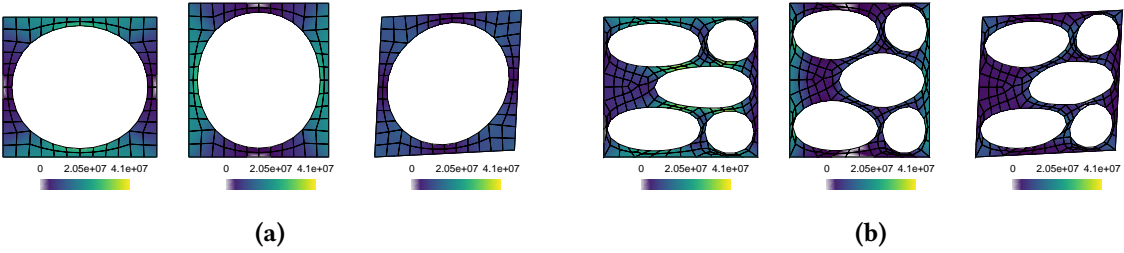


**Figure 5.8.** Deformed shape scaled 100x and Von Mises stress field of microstructure after applying a known macro strain field,  $\varepsilon = [\varepsilon_x, 0, 0], [0, \varepsilon_y, 0], [0, 0, \gamma_{xy}]$  where  $\varepsilon_x = \varepsilon_y = \gamma_{xy} = 10^{-4}$  in (a) circular and (b) multiple ellipses microstructure.

## 6. CONCLUSION

This work focused on developing an in-house code that can be later expanded and serve as a base for prototyping new analysis methods. The implementation was verified using simple benchmark problems.

The multiscale procedure implemented, also known as FE<sup>2</sup>, proved as an option to treat highly heterogeneous problems which are difficult to solve using the standard FEM approach. The procedure also poses many challenges, one of them is the high computational cost for nonlinear analysis. The high cost occur due the need to perform a non linear finite element analysis for each macro gauss point. When the Taylor assumption for the RVE is considered the macro field is applied homogeneously in the micro domain and the fluctuations are not considered. Since the micro fields are known, there is no need to solve a boundary field problem in this case, which reduces the computational cost. By not considering the micro fluctuations the complex interaction that may happen in the microstructure is not taken into account. Therefore, the Taylor assumption serves as an approximation of the macro-micro coupling.

The Taylor assumption for the RVE displacement condition produced a stiffer model. When the fluctuations are considered, we need to solve a boundary value problem at each gauss point. When nonlinearity is considered, multiple iterations are needed for each of them. This introduces a great amount of extra computations into the problem. A first intuitive solution is to use parallelization to solve the micro problem for the RVE. Other solution is to use the micro scale solution only at points of interest, an adaptive method.

Although the multiscale procedure is computationally expensive, it allows computing the structure response for arbitrary microstructure geometry. New mechanical models to predict complex phenomena can be gradually added to the code. In this work we presented microstructures with square and circular voids, however the code is capable of handling arbitrary plane geometry.

We presented an example of the code application to model the proximal part of human femur considering that the cancelous bone is highly porous. We tested the effect of the void distribution in the microstructure, concluding that it affects the overall response significantly, specially when high porosity is considered. We tested RVE with void fraction of 30% and 60%. As expected, a greater void fraction produces a more flexible overall response. Two different micro structure configuration were tested, one with a single circular void and other with multiple ellipses voids. The micro structure with multiple voids produces a more flexible macro response. The difference between the micro structure configuration is much more noticeable for large void fraction. This happens because the void distribution creates regions of stress concentration that are more susceptible to plastification.

Further research based on this work can explore different aspects of the problem, such as

1. Parallelization of the RVE boundary value problem;
2. New constitutive models for the micro scale problem;
3. Add complex modeling such as damage, crack formation and debonding mechanism to the microstructure;
4. New techniques to optimize the micro scale procedure for nonlinear problems.

## REFERENCES

- Abdel-Wahab, Adel A., Angelo R. Maligno, and Vadim V. Silberschmidt (Feb. 2012). “Micro-Scale Modelling of Bovine Cortical Bone Fracture: Analysis of Crack Propagation and Microstructure Using X-FEM”. en. In: *Computational Materials Science* 52.1, pp. 128–135. ISSN: 09270256. DOI: [10.1016/j.commatsci.2011.01.021](https://doi.org/10.1016/j.commatsci.2011.01.021).
- Asada, Takashi and Nobutada Ohno (Nov. 2007). “Fully Implicit Formulation of Elastoplastic Homogenization Problem for Two-Scale Analysis”. en. In: *International Journal of Solids and Structures* 44.22-23, pp. 7261–7275. ISSN: 00207683. DOI: [10.1016/j.ijsolstr.2007.04.007](https://doi.org/10.1016/j.ijsolstr.2007.04.007).
- Bencheikh, I., F. Bilteryst, and M. Nouari (Oct. 2017). “Modelling of the Thermomechanical Behaviour of Coated Structures Using Single and Multi-Level-Set Techniques Coupled with the eXtended Finite Element Method”. en. In: *Finite Elements in Analysis and Design* 134, pp. 68–81. ISSN: 0168874X. DOI: [10.1016/j.finel.2017.06.001](https://doi.org/10.1016/j.finel.2017.06.001).
- Blanco, Pablo J., Pablo J. Sánchez, Eduardo A. de Souza Neto, and Raúl A. Feijóo (June 2016). “Variational Foundations and Generalized Unified Theory of RVE-Based Multiscale Models”. en. In: *Archives of Computational Methods in Engineering* 23.2, pp. 191–253. ISSN: 1134-3060, 1886-1784. DOI: [10.1007/s11831-014-9137-5](https://doi.org/10.1007/s11831-014-9137-5).
- Böhm, H.J, A Eckschlagler, and W Han (Sept. 2002). “Multi-Inclusion Unit Cell Models for Metal Matrix Composites with Randomly Oriented Discontinuous Reinforcements”. en. In: *Computational Materials Science* 25.1-2, pp. 42–53. ISSN: 09270256. DOI: [10.1016/S0927-0256\(02\)00248-3](https://doi.org/10.1016/S0927-0256(02)00248-3).
- Borst, René de and M. A. Crisfield, eds. (2012). *Nonlinear Finite Element Analysis of Solids and Structures*. 2nd ed. Hoboken, NJ: Wiley. ISBN: 978-0-470-66644-9.
- Budyn, Élisabeth and Thierry Hoc (Jan. 2007). “Multiple scale modeling for cortical bone fracture in tension using X-FEM”. fr. In: *European Journal of Computational Mechanics* 16.2, pp. 213–236. ISSN: 1779-7179, 1958-5829. DOI: [10.3166/remn.16.213-236](https://doi.org/10.3166/remn.16.213-236).
- Callister, William D. (2007). *Materials Science and Engineering: An Introduction*. en. 7. ed. OCLC: 636794325. New York, NY: Wiley. ISBN: 978-0-471-73696-7.
- Carneiro Molina, A.J. and J.L. Curiel-Sosa (Feb. 2015). “A Multiscale Finite Element Technique for Nonlinear Multi-Phase Materials”. en. In: *Finite Elements in Analysis and Design* 94, pp. 64–80. ISSN: 0168874X. DOI: [10.1016/j.finel.2014.10.001](https://doi.org/10.1016/j.finel.2014.10.001).
- Cowin, Stephen C., ed. (Mar. 2001). *Bone Mechanics Handbook*. en. 0th ed. CRC Press. ISBN: 978-0-429-12544-7. DOI: [10.1201/b14263](https://doi.org/10.1201/b14263).
- de Souza Neto, E. A. and R. A. Feijóo (2006). *Variational Foundations of Multi-Scale Constitutive Models of Solid: Small and Large Strain Kinematical Formulation*. Tech. rep.
- de Souza Neto, E. A., D. Peri, and D. R. J. Owen (Oct. 2008). *Computational Methods for Plasticity*. en. Chichester, UK: John Wiley & Sons, Ltd. ISBN: 978-0-470-69462-6 978-0-470-69452-7. DOI: [10.1002/9780470694626](https://doi.org/10.1002/9780470694626).
- de Souza Neto, E.A. and R.A. Feijóo (Oct. 2008). “On the Equivalence between Spatial and Material Volume Averaging of Stress in Large Strain Multi-Scale Solid Constitutive Models”. en. In: *Mechanics of Materials* 40.10, pp. 803–811. ISSN: 01676636. DOI: [10.1016/j.mechmat.2008.04.006](https://doi.org/10.1016/j.mechmat.2008.04.006).
- de Souza Neto, E.A., P.J. Blanco, P.J. Sánchez, and R.A. Feijóo (Jan. 2015). “An RVE-Based Multi-scale Theory of Solids with Micro-Scale Inertia and Body Force Effects”. en. In: *Mechanics of Materials* 80, pp. 136–144. ISSN: 01676636. DOI: [10.1016/j.mechmat.2014.10.007](https://doi.org/10.1016/j.mechmat.2014.10.007).
- Eftekhari, Mehdi, Saeed Hatefi Ardakani, and Soheil Mohammadi (Aug. 2014). “An XFEM Multiscale Approach for Fracture Analysis of Carbon Nanotube Reinforced Concrete”. en.

- In: *Theoretical and Applied Fracture Mechanics* 72, pp. 64–75. ISSN: 01678442. DOI: [10.1016/j.tafmec.2014.06.005](https://doi.org/10.1016/j.tafmec.2014.06.005).
- Eidel, Bernhard and Andreas Fischer (Feb. 2018). “The Heterogeneous Multiscale Finite Element Method for the Homogenization of Linear Elastic Solids and a Comparison with the FE<sup>2</sup> Method”. en. In: *Computer Methods in Applied Mechanics and Engineering* 329, pp. 332–368. ISSN: 00457825. DOI: [10.1016/j.cma.2017.10.001](https://doi.org/10.1016/j.cma.2017.10.001). arXiv: [1701.08313](https://arxiv.org/abs/1701.08313).
- Eshelby, J. D. (Aug. 1957). “The Determination of the Elastic Field of an Ellipsoidal Inclusion, and Related Problems”. en. In: *Proceedings of the Royal Society of London. Series A. Mathematical and Physical Sciences* 241.1226, pp. 376–396. ISSN: 2053-9169. DOI: [10.1098/rspa.1957.0133](https://doi.org/10.1098/rspa.1957.0133).
- Feyel, Frédéric (Dec. 1999). “Multiscale FE<sup>2</sup> Elastoviscoplastic Analysis of Composite Structures”. en. In: *Computational Materials Science* 16.1-4, pp. 344–354. ISSN: 09270256. DOI: [10.1016/S0927-0256\(99\)00077-4](https://doi.org/10.1016/S0927-0256(99)00077-4).
- (July 2003). “A Multilevel Finite Element Method (FE<sup>2</sup>) to Describe the Response of Highly Non-Linear Structures Using Generalized Continua”. en. In: *Computer Methods in Applied Mechanics and Engineering* 192.28-30, pp. 3233–3244. ISSN: 00457825. DOI: [10.1016/S0045-7825\(03\)00348-7](https://doi.org/10.1016/S0045-7825(03)00348-7).
- Feyel, Frédéric and Jean-Louis Chaboche (2000). “FE<sup>2</sup> Multiscale Approach for Modelling the Elastoviscoplastic Behaviour of Long Fibre SiC/Ti Composite Materials”. In: *Computer Methods in Applied Mechanics and Engineering* 183, pp. 309–330.
- Geers, M.G.D., V.G. Kouznetsova, and W.A.M. Brekelmans (Aug. 2010). “Multi-Scale Computational Homogenization: Trends and Challenges”. en. In: *Journal of Computational and Applied Mathematics* 234.7, pp. 2175–2182. ISSN: 03770427. DOI: [10.1016/j.cam.2009.08.077](https://doi.org/10.1016/j.cam.2009.08.077).
- Gruet, Fermin Otero (2015). “Multiscale numerical modelling of microstructured reinforced composites”. es. PhD thesis.
- Guedes, José Miranda and Noboru Kikuchi (Oct. 1990). “Preprocessing and Postprocessing for Materials Based on the Homogenization Method with Adaptive Finite Element Methods”. en. In: *Computer Methods in Applied Mechanics and Engineering* 83.2, pp. 143–198. ISSN: 00457825. DOI: [10.1016/0045-7825\(90\)90148-F](https://doi.org/10.1016/0045-7825(90)90148-F).
- Gurtin, Morton E. (1981). *An Introduction to Continuum Mechanics*. Mathematics in Science and Engineering v. 158. New York: Academic Press. ISBN: 978-0-12-309750-7.
- Hill, R. (Sept. 1963). “Elastic Properties of Reinforced Solids: Some Theoretical Principles”. en. In: *Journal of the Mechanics and Physics of Solids* 11.5, pp. 357–372. ISSN: 00225096. DOI: [10.1016/0022-5096\(63\)90036-X](https://doi.org/10.1016/0022-5096(63)90036-X).
- (Jan. 1972). “On Constitutive Macro-Variables for Heterogeneous Solids at Finite Strain”. en. In: *Proceedings of the Royal Society A: Mathematical, Physical and Engineering Sciences* 326.1565, pp. 131–147. ISSN: 1364-5021, 1471-2946. DOI: [10.1098/rspa.1972.0001](https://doi.org/10.1098/rspa.1972.0001).
- Hollister, S. J. and N. Kikuchi (1992). “A Comparison of Homogenization and Standard Mechanics Analyses for Periodic Porous Composites”. en. In: *Computational Mechanics* 10.2, pp. 73–95. ISSN: 0178-7675, 1432-0924. DOI: [10.1007/BF00369853](https://doi.org/10.1007/BF00369853).
- Hori, Muneo and Sia Nemat-Nasser (Oct. 1999). “On Two Micromechanics Theories for Determining Micro–Macro Relations in Heterogeneous Solids”. en. In: *Mechanics of Materials* 31.10, pp. 667–682. ISSN: 01676636. DOI: [10.1016/S0167-6636\(99\)00020-4](https://doi.org/10.1016/S0167-6636(99)00020-4).
- Javili, Ali, George Chatzigeorgiou, Andrew T. McBride, Paul Steinmann, and Christian Linder (Sept. 2015). “Computational Homogenization of Nano-Materials Accounting for Size Effects via Surface Elasticity: Computational Homogenization of Nano-Materials Accounting for Size Effects via Surface Elasticity”. en. In: *GAMM-Mitteilungen* 38.2, pp. 285–312. ISSN: 09367195. DOI: [10.1002/gamm.201510016](https://doi.org/10.1002/gamm.201510016).

- Jothi, S., T.N. Croft, S.G.R. Brown, and E.A. de Souza Neto (Feb. 2014). “Finite Element Microstructural Homogenization Techniques and Intergranular, Intragranular Microstructural Effects on Effective Diffusion Coefficient of Heterogeneous Polycrystalline Composite Media”. en. In: *Composite Structures* 108, pp. 555–564. ISSN: 02638223. DOI: [10.1016/j.compstruct.2013.09.026](https://doi.org/10.1016/j.compstruct.2013.09.026).
- Kaczmarczyk, Łukasz, Chris J. Pearce, and Nenad Bićanić (Apr. 2008). “Scale Transition and Enforcement of RVE Boundary Conditions in Second-Order Computational Homogenization”. en. In: *International Journal for Numerical Methods in Engineering* 74.3, pp. 506–522. ISSN: 00295981, 10970207. DOI: [10.1002/nme.2188](https://doi.org/10.1002/nme.2188).
- Kanit, T., S. Forest, I. Galliet, V. Mounoury, and D. Jeulin (June 2003). “Determination of the Size of the Representative Volume Element for Random Composites: Statistical and Numerical Approach”. en. In: *International Journal of Solids and Structures* 40.13-14, pp. 3647–3679. ISSN: 00207683. DOI: [10.1016/S0020-7683\(03\)00143-4](https://doi.org/10.1016/S0020-7683(03)00143-4).
- Kanouté, P., D. P. Boso, J. L. Chaboche, and B. A. Schrefler (Mar. 2009). “Multiscale Methods for Composites: A Review”. en. In: *Archives of Computational Methods in Engineering* 16.1, pp. 31–75. ISSN: 1134-3060, 1886-1784. DOI: [10.1007/s11831-008-9028-8](https://doi.org/10.1007/s11831-008-9028-8).
- Khoei, Amir R (2015). *Extended Finite Element Method: Theory and Applications*. John Wiley & Sons, Inc.
- Kouznetsova, V., M. G. D. Geers, and W. A. M. Brekelmans (July 2002). “Multi-Scale Constitutive Modelling of Heterogeneous Materials with a Gradient-Enhanced Computational Homogenization Scheme”. en. In: *International Journal for Numerical Methods in Engineering* 54.8, pp. 1235–1260. ISSN: 0029-5981, 1097-0207. DOI: [10.1002/nme.541](https://doi.org/10.1002/nme.541).
- Kouznetsova, V.G., M.G.D. Geers, and W.A.M. Brekelmans (Dec. 2004). “Multi-Scale Second-Order Computational Homogenization of Multi-Phase Materials: A Nested Finite Element Solution Strategy”. en. In: *Computer Methods in Applied Mechanics and Engineering* 193.48-51, pp. 5525–5550. ISSN: 00457825. DOI: [10.1016/j.cma.2003.12.073](https://doi.org/10.1016/j.cma.2003.12.073).
- Matouš, Karel, Marc G.D. Geers, Varvara G. Kouznetsova, and Andrew Gillman (Feb. 2017). “A Review of Predictive Nonlinear Theories for Multiscale Modeling of Heterogeneous Materials”. en. In: *Journal of Computational Physics* 330, pp. 192–220. ISSN: 00219991. DOI: [10.1016/j.jcp.2016.10.070](https://doi.org/10.1016/j.jcp.2016.10.070).
- Matsui, Kazumi, Kenjiro Terada, and Kohei Yuge (Mar. 2004). “Two-Scale Finite Element Analysis of Heterogeneous Solids with Periodic Microstructures”. en. In: *Computers & Structures* 82.7-8, pp. 593–606. ISSN: 00457949. DOI: [10.1016/j.compstruct.2004.01.004](https://doi.org/10.1016/j.compstruct.2004.01.004).
- McDowell, David L. (Sept. 2010). “A Perspective on Trends in Multiscale Plasticity”. en. In: *International Journal of Plasticity* 26.9, pp. 1280–1309. ISSN: 07496419. DOI: [10.1016/j.ijplas.2010.02.008](https://doi.org/10.1016/j.ijplas.2010.02.008).
- Michel, J.C., H. Moulinec, and P. Suquet (Apr. 1999). “Effective Properties of Composite Materials with Periodic Microstructure: A Computational Approach”. en. In: *Computer Methods in Applied Mechanics and Engineering* 172.1-4, pp. 109–143. ISSN: 00457825. DOI: [10.1016/S0045-7825\(98\)00227-8](https://doi.org/10.1016/S0045-7825(98)00227-8).
- Miehe, C. and A. Koch (July 2002). “Computational Micro-to-Macro Transitions of Discretized Microstructures Undergoing Small Strains”. en. In: *Archive of Applied Mechanics (Ingenieur Archiv)* 72.4-5, pp. 300–317. ISSN: 09391533. DOI: [10.1007/s00419-002-0212-2](https://doi.org/10.1007/s00419-002-0212-2).
- Miehe, C., J. Dettmar, and D. Zäh (Aug. 2010). “Homogenization and Two-Scale Simulations of Granular Materials for Different Microstructural Constraints”. en. In: *International Journal for Numerical Methods in Engineering* 83.8-9, pp. 1206–1236. ISSN: 00295981. DOI: [10.1002/nme.2875](https://doi.org/10.1002/nme.2875).

- Nemat-Nasser, S., N. Yu, and M. Hori (May 1993). “Bounds and Estimates of Overall Moduli of Composites with Periodic Microstructure”. en. In: *Mechanics of Materials* 15.3, pp. 163–181. ISSN: 01676636. DOI: [10.1016/0167-6636\(93\)90016-K](https://doi.org/10.1016/0167-6636(93)90016-K).
- Nguyen, Vinh Phu, Martijn Stroeve, and Lambertus Johannes Sluys (Dec. 2011). “MULTISCALE CONTINUOUS AND DISCONTINUOUS MODELING OF HETEROGENEOUS MATERIALS: A REVIEW ON RECENT DEVELOPMENTS”. en. In: *Journal of Multiscale Modelling* 03.04, pp. 229–270. ISSN: 1756-9737, 1756-9745. DOI: [10.1142/S1756973711000509](https://doi.org/10.1142/S1756973711000509).
- Oliver, J., M. Caicedo, A.E. Huespe, J.A. Hernández, and E. Roubin (Jan. 2017). “Reduced Order Modeling Strategies for Computational Multiscale Fracture”. en. In: *Computer Methods in Applied Mechanics and Engineering* 313, pp. 560–595. ISSN: 00457825. DOI: [10.1016/j.cma.2016.09.039](https://doi.org/10.1016/j.cma.2016.09.039).
- Otero, Fermin, Sergio Oller, and Xavier Martinez (Apr. 2018). “Multiscale Computational Homogenization: Review and Proposal of a New Enhanced-First-Order Method”. en. In: *Archives of Computational Methods in Engineering* 25.2, pp. 479–505. ISSN: 1134-3060, 1886-1784. DOI: [10.1007/s11831-016-9205-0](https://doi.org/10.1007/s11831-016-9205-0).
- Parashar, Sandeep Kumar and Jai Kumar Sharma (Sept. 2016). “A Review on Application of Finite Element Modelling in Bone Biomechanics”. en. In: *Perspectives in Science* 8, pp. 696–698. ISSN: 22130209. DOI: [10.1016/j.pisc.2016.06.062](https://doi.org/10.1016/j.pisc.2016.06.062).
- Perić, D., E. A. de Souza Neto, R. A. Feijóo, M. Partovi, and A. J. Carneiro Molina (July 2011). “On Micro-to-Macro Transitions for Multi-Scale Analysis of Non-Linear Heterogeneous Materials: Unified Variational Basis and Finite Element Implementation”. en. In: *International Journal for Numerical Methods in Engineering* 87.1-5, pp. 149–170. ISSN: 00295981. DOI: [10.1002/nme.3014](https://doi.org/10.1002/nme.3014).
- Podshivalov, L., A. Fischer, and P.Z. Bar-Yoseph (Aug. 2011). “Multiscale FE Method for Analysis of Bone Micro-Structures”. en. In: *Journal of the Mechanical Behavior of Biomedical Materials* 4.6, pp. 888–899. ISSN: 17516161. DOI: [10.1016/j.jmbbm.2011.03.003](https://doi.org/10.1016/j.jmbbm.2011.03.003).
- Saavedra Flores, E.I. and E.A. de Souza Neto (June 2010). “Remarks on Symmetry Conditions in Computational Homogenisation Problems”. en. In: *Engineering Computations* 27.4, pp. 551–575. ISSN: 0264-4401. DOI: [10.1108/02644401011044612](https://doi.org/10.1108/02644401011044612).
- Saavedra Flores, E.I. and M.I. Friswell (July 2012). “Multi-Scale Finite Element Model for a New Material Inspired by the Mechanics and Structure of Wood Cell-Walls”. en. In: *Journal of the Mechanics and Physics of Solids* 60.7, pp. 1296–1309. ISSN: 00225096. DOI: [10.1016/j.jmps.2012.03.007](https://doi.org/10.1016/j.jmps.2012.03.007).
- Saeb, Saba, Paul Steinmann, and Ali Javili (Sept. 2016). “Aspects of Computational Homogenization at Finite Deformations: A Unifying Review From Reuss’ to Voigt’s Bound”. en. In: *Applied Mechanics Reviews* 68.5, p. 050801. ISSN: 0003-6900. DOI: [10.1115/1.4034024](https://doi.org/10.1115/1.4034024).
- Sánchez, P.J., P.J. Blanco, A.E. Huespe, and R.A. Feijóo (Apr. 2013). “Failure-Oriented Multi-Scale Variational Formulation: Micro-Structures with Nucleation and Evolution of Softening Bands”. en. In: *Computer Methods in Applied Mechanics and Engineering* 257, pp. 221–247. ISSN: 00457825. DOI: [10.1016/j.cma.2012.11.016](https://doi.org/10.1016/j.cma.2012.11.016).
- Simo, J. C. and Thomas J. R. Hughes (1998). *Computational Inelasticity*. en. Interdisciplinary Applied Mathematics v. 7. New York: Springer. ISBN: 978-0-387-97520-7.
- Smit, R.J.M., W.A.M. Brekelmans, and H.E.H. Meijer (Mar. 1998). “Prediction of the Mechanical Behavior of Nonlinear Heterogeneous Systems by Multi-Level Finite Element Modeling”. en. In: *Computer Methods in Applied Mechanics and Engineering* 155.1-2, pp. 181–192. ISSN: 00457825. DOI: [10.1016/S0045-7825\(97\)00139-4](https://doi.org/10.1016/S0045-7825(97)00139-4).
- Suquet, Pierre (1983). “Local and Global Aspects in the Mathematical Theory of Plasticity”. In: *International Symposium on Current Trends and Results in Plasticity*.

- Taylor I., G. (1938). "Plastic Strain in Metals". In: *Journal of the Institute of Metals* 62, pp. 307–324.
- Tchalla, Adjovi, Salim Belouettar, Ahmed Makradi, and Hamid Zahrouni (Sept. 2013). "An ABAQUS Toolbox for Multiscale Finite Element Computation". en. In: *Composites Part B: Engineering* 52, pp. 323–333. ISSN: 13598368. DOI: [10.1016/j.compositesb.2013.04.028](https://doi.org/10.1016/j.compositesb.2013.04.028).
- Temizer, I. and T. I. Zohdi (Apr. 2007). "A Numerical Method for Homogenization in Non-Linear Elasticity". en. In: *Computational Mechanics* 40.2, pp. 281–298. ISSN: 0178-7675, 1432-0924. DOI: [10.1007/s00466-006-0097-y](https://doi.org/10.1007/s00466-006-0097-y).
- Terada, K. and N. Kikuchi (July 2001). "A Class of General Algorithms for Multi-Scale Analyses of Heterogeneous Media". en. In: *Computer Methods in Applied Mechanics and Engineering* 190.40-41, pp. 5427–5464. ISSN: 00457825. DOI: [10.1016/S0045-7825\(01\)00179-7](https://doi.org/10.1016/S0045-7825(01)00179-7).
- Tong, Liyong, Adrian P. Mouritz, and Michael K. Bannister (2002). *3D Fibre Reinforced Polymer Composites*. 1st ed. Boston: Elsevier. ISBN: 978-0-08-043938-9.
- Ullah, Z., L. Kaczmarczyk, and C.J. Pearce (Feb. 2017). "Three-Dimensional Nonlinear Micro/Meso-Mechanical Response of the Fibre-Reinforced Polymer Composites". en. In: *Composite Structures* 161, pp. 204–214. ISSN: 02638223. DOI: [10.1016/j.compstruct.2016.11.059](https://doi.org/10.1016/j.compstruct.2016.11.059).
- Ural, Ani and Susan Mischinski (May 2013). "Multiscale Modeling of Bone Fracture Using Cohesive Finite Elements". en. In: *Engineering Fracture Mechanics* 103, pp. 141–152. ISSN: 00137944. DOI: [10.1016/j.engfracmech.2012.05.008](https://doi.org/10.1016/j.engfracmech.2012.05.008).
- van den Munckhof, Sven and Amir Abbas Zadpoor (Apr. 2014). "How Accurately Can We Predict the Fracture Load of the Proximal Femur Using Finite Element Models?" en. In: *Clinical Biomechanics* 29.4, pp. 373–380. ISSN: 02680033. DOI: [10.1016/j.clinbiomech.2013.12.018](https://doi.org/10.1016/j.clinbiomech.2013.12.018).
- Vaz Júnior, Miguel, E. A. de Souza Neto, and Pablo A. Muñoz-Rojas, eds. (2011). *Advanced Computational Materials Modeling: From Classical to Multi-Scale Techniques*. OCLC: ocn696923256. Weinheim, Germany: Wiley-VCH. ISBN: 978-3-527-32479-8.
- Vellwock, Andre E., Laura Vergani, and Flavia Libonati (May 2018). "A Multiscale XFEM Approach to Investigate the Fracture Behavior of Bio-Inspired Composite Materials". en. In: *Composites Part B: Engineering* 141, pp. 258–264. ISSN: 13598368. DOI: [10.1016/j.compositesb.2017.12.062](https://doi.org/10.1016/j.compositesb.2017.12.062).
- Wolfram, Uwe and Jakob Schwiedrzik (Aug. 2016). "Post-Yield and Failure Properties of Cortical Bone". In: *BoneKEy Reports* 5. ISSN: 20476396. DOI: [10.1038/bonekey.2016.60](https://doi.org/10.1038/bonekey.2016.60).
- Yuan, Zheng and Jacob Fish (Jan. 2008). "Toward Realization of Computational Homogenization in Practice". en. In: *International Journal for Numerical Methods in Engineering* 73.3, pp. 361–380. ISSN: 00295981, 10970207. DOI: [10.1002/nme.2074](https://doi.org/10.1002/nme.2074).

## A. MATHEMATICAL PRELIMINARIES

### A.1. LINEARIZATION OF A GENERAL NONLINEAR MULTI VARIABLE FUNCTION

Given a general multi variable function, or functional,  $\mathbf{F}(\mathbf{x})$ , we can state the following problem which consists of finding a root  $\mathbf{x}$  of the function

$$\mathbf{F}(\mathbf{x}) = \mathbf{0} \quad (\text{A.1})$$

we then take the Taylor expansion of this function about a general point,  $\mathbf{x} = \mathbf{x}_0$ , in a general direction  $\delta\mathbf{x} = \mathbf{x} - \mathbf{x}_0$ ,

$$\mathbf{F}(\mathbf{x}) = \mathbf{F}(\mathbf{x}_0) + \mathcal{D}\mathbf{F}(\mathbf{x}_0)[\delta\mathbf{x}] + \dots \quad (\text{A.2})$$

where the notation  $\mathcal{D}\mathbf{F}(\cdot)[\cdot]$  indicates the directional derivative of the function  $\mathbf{F}$  at  $(\cdot)$  in the direction of  $[\cdot]$  (Gurtin 1981). We can also ignore the higher order terms in the expansion to get a linear approximation. The directional derivative, which is also called tangent matrix, can be computed with the aid of an extra perturbation parameter  $\epsilon$ ,

$$\mathcal{D}\mathbf{F}(\mathbf{x}_0)[\delta\mathbf{x}] = \left. \frac{d}{d\epsilon} \right|_{\epsilon=0} \mathbf{F}(\mathbf{x}_0 + \epsilon\delta\mathbf{x}) \quad (\text{A.3})$$

$$= \begin{bmatrix} \left. \frac{dF_1}{dx_1} \right|_{\mathbf{x}_0} & \left. \frac{dF_1}{dx_2} \right|_{\mathbf{x}_0} & \dots \\ \left. \frac{dF_2}{dx_1} \right|_{\mathbf{x}_0} & \left. \frac{dF_2}{dx_2} \right|_{\mathbf{x}_0} & \dots \\ \vdots & \vdots & \ddots \end{bmatrix} \delta\mathbf{x} \quad (\text{A.4})$$

$$= \mathbf{K}(\mathbf{x}_0)\delta\mathbf{x} \quad (\text{A.5})$$

where the chain rule was used. Then, calling the linear approximation a *linearization* of  $\mathbf{F}$  about  $\mathbf{x}_0$ , the problem can be stated as *find*  $\delta\mathbf{x}$  such that

$$\mathcal{L}\mathbf{F}(\mathbf{x}_0 + \delta\mathbf{x}) = \mathbf{F}(\mathbf{x}_0) + \mathcal{D}\mathbf{F}(\mathbf{x}_0)[\delta\mathbf{x}] = \mathbf{0}. \quad (\text{A.6})$$

which implies finding when the linearization is zero. In two dimension this means approximate the solution for the zero of the tangent line. If we repeat this procedure we tend to get closer to the actual solution to eq. (A.1). Using the result in eq. (A.6), we get the following system to find the increment of the approximate solution

$$\mathbf{K}(\mathbf{x}_0)\delta\mathbf{x} = -\mathbf{F}(\mathbf{x}_0) \quad (\text{A.7})$$

### A.2. DERIVATIVE OF TENSORS FUNCTIONS OF TENSORS

The derivative is a linear transformation between finite dimensional spaces (Gurtin 1981; de Souza Neto et al. 2008). It can be represented for second order tensor function with arguments also second order tensors as

$$\mathcal{D}\mathcal{F}(\boldsymbol{\varepsilon}_*)[\delta\boldsymbol{\varepsilon}] \equiv \left. \frac{d\mathcal{F}}{d\boldsymbol{\varepsilon}} \right|_{\boldsymbol{\varepsilon}_*} : \delta\boldsymbol{\varepsilon} \quad (\text{A.8})$$

where the derivative of second order tensor with respect to a second order tensor is equal a fourth order tensor, hence the double contraction operation in order to satisfy the mapping between two second order tensors ( $\delta\boldsymbol{\varepsilon}$  and  $\mathcal{D}\mathcal{F}(\boldsymbol{\varepsilon}_0)[\delta\boldsymbol{\varepsilon}]$ ).

The above expression, eq. (B.33), can be visualized using an analogy with scalar variables,

$$f(x_0 + \delta x) = f(x_0) + \left. \frac{df}{dx} \right|_{x_0} \delta x \quad (\text{A.9})$$

hence, from eq. (A.2), ignoring higher order terms, we arrive at eq. (A.9). Therefore,

$$\mathcal{D}f(x_0)[\delta x] = \left. \frac{df}{dx} \right|_{x_0} \delta x \quad (\text{A.10})$$

### A.3. CHAIN RULE

For a function of another function, a composition,

$$\mathcal{Y}(\varepsilon) = \mathcal{Y}(\mathcal{G}(\varepsilon)) \quad (\text{A.11})$$

the derivative of  $\mathcal{Y}$  at  $\varepsilon$ , (Gurtin 1981), is

$$\mathcal{D}\mathcal{Y}(\varepsilon)[\delta\varepsilon] = \mathcal{D}\mathcal{Y}(\mathcal{G}(\varepsilon))[\mathcal{D}\mathcal{G}(\varepsilon)[\delta\varepsilon]] \quad (\text{A.12})$$

Using a scalar function as example,

$$\mathcal{D}f(g(x))[\delta x] = \mathcal{D}f(g(x))[\mathcal{D}g(x)[\delta x]] \quad (\text{A.13})$$

which can be written, using the definition in eq. (A.10), as

$$\mathcal{D}f(g(x))[\delta x] = \frac{df}{dg} \frac{dg}{dx} \delta x \quad (\text{A.14})$$

## B. COMPUTATIONAL PLASTICITY

In this appendix some aspects of computational plasticity are presented with explicit expression for ready implementation. First we present the linearization of the virtual work equation. Then, its discretized form. After stating the FEM procedure we need to solve the material nonlinearity with a return mapping algorithm. This solution will yield the tangent operator. The general formulation for obtaining the tangent operator is presented followed by a specific formulation considering Von Mises yield criteria and isotropic hardening. Next the specific case of the returning map procedure is presented considering Von Mises yield criteria.

### B.0.1. LINEARIZATION OF THE VIRTUAL WORK

This process is also discussed in Simo and Hughes (1998) and de Souza Neto et al. (2008). Considering that the stress tensor is a function only of the current strains only,

$$\boldsymbol{\sigma} \stackrel{\text{def}}{=} \boldsymbol{\sigma}(\boldsymbol{\varepsilon}) \quad (\text{B.1})$$

the problem can be stated as finding kinematically admissible displacement field,  $\mathbf{u}$ , that satisfy the equilibrium equation,

$$G(\mathbf{u}, \boldsymbol{\eta}) = 0, \quad \forall \boldsymbol{\eta} \in \mathcal{V} \quad (\text{B.2})$$

where,  $\mathcal{V}$  is the space of virtual displacements defined as  $\mathcal{V} = \{\boldsymbol{\eta} : V \rightarrow \mathcal{U} \mid \boldsymbol{\eta} = \mathbf{0} \text{ on } S_u\}$ , in which  $\mathcal{U}$  is the space of vectors the three-dimensions euclidian space, and  $S_u$  is the boundary where the displacement is prescribed.  $G$  is the virtual work functional,

$$G(\mathbf{u}, \boldsymbol{\eta}) \stackrel{\text{def}}{=} \int_V (\boldsymbol{\sigma} : \nabla^s \boldsymbol{\eta} - \mathbf{b} \cdot \boldsymbol{\eta}) dV - \int_{S_t} \mathbf{t} \cdot \boldsymbol{\eta} dA \quad (\text{B.3})$$

Noting that the dependence of  $\mathbf{u}$  occurs through the stress functional  $\boldsymbol{\sigma}(\boldsymbol{\varepsilon})$ .

We aim to linearize equation (B.2) with respect to  $\mathbf{u}$  about an arbitrary argument  $\mathbf{u}^*$ . Using the multi variable Taylor expansion, the linearized problem consists of finding  $\delta \mathbf{u}$  such that,

$$L(\delta \mathbf{u}, \boldsymbol{\eta}) \stackrel{\text{def}}{=} G(\mathbf{u}^*, \boldsymbol{\eta}) + \mathcal{D}G(\mathbf{u}^*, \boldsymbol{\eta})[\delta \mathbf{u}] = 0, \forall \boldsymbol{\eta} \in \mathcal{V}, \quad (\text{B.4})$$

where  $L$  is the linearized virtual work functional and the gradient operator  $\mathcal{D}$ , or directional derivatives at  $\mathbf{u}^*$  in the direction of  $\delta \mathbf{u}$ , is defined as<sup>7</sup>,

$$\mathcal{D}G(\mathbf{u}^*, \boldsymbol{\eta})[\delta \mathbf{u}] \stackrel{\text{def}}{=} \left. \frac{d}{d\epsilon} \right|_{\epsilon=0} G(\mathbf{u}^* + \epsilon \delta \mathbf{u}, \boldsymbol{\eta}). \quad (\text{B.6})$$

Substituting  $G$  from equation (B.3), into above equation (B.6), we get,

$$\mathcal{D}G(\mathbf{u}^*, \boldsymbol{\eta})[\delta \mathbf{u}] = \left. \frac{d}{d\epsilon} \right|_{\epsilon=0} \int_V \boldsymbol{\sigma}(\boldsymbol{\varepsilon}(\epsilon)) : \nabla^s \boldsymbol{\eta} dV \quad (\text{B.7})$$

applying the chain rule in the derivative of the stress tensor,  $\frac{d\boldsymbol{\sigma}}{d\epsilon} = \frac{d\boldsymbol{\sigma}}{d\boldsymbol{\varepsilon}} \frac{d\boldsymbol{\varepsilon}}{d\epsilon}$ , the above equation becomes

$$\mathcal{D}G(\mathbf{u}^*, \boldsymbol{\eta})[\delta \mathbf{u}] = \int_V \mathbf{D} : \nabla^s \delta \mathbf{u} : \nabla^s \boldsymbol{\eta} dV \quad (\text{B.8})$$

where the following function was used for the strain as a function of the perturbation  $\epsilon$

$$\boldsymbol{\varepsilon}(\epsilon) \stackrel{\text{def}}{=} \nabla^s (\mathbf{u}^* + \epsilon \delta \mathbf{u}) \equiv \boldsymbol{\varepsilon}^* + \epsilon \nabla^s \delta \mathbf{u} \quad (\text{B.9})$$

and the infinitesimal tangent modulus is then defined as,<sup>8</sup>

$$\mathbf{D} \stackrel{\text{def}}{=} \left. \frac{\partial \boldsymbol{\sigma}}{\partial \boldsymbol{\varepsilon}} \right|_{\boldsymbol{\varepsilon}^*} \quad (\text{B.10})$$

where,  $\boldsymbol{\varepsilon}^* \stackrel{\text{def}}{=} \nabla^s \mathbf{u}^*$  is simply the strain tensor field at  $\mathbf{u}^*$ .<sup>9</sup>

The linearized virtual work is then,

$$\int_V \mathbf{D} : \nabla^s \delta \mathbf{u} : \nabla^s \boldsymbol{\eta} dV = - \int_V (\boldsymbol{\sigma} : \nabla^s \boldsymbol{\eta} - \mathbf{b} \cdot \boldsymbol{\eta}) dV - \int_S \mathbf{t} \cdot \boldsymbol{\eta} dA \quad (\text{B.11})$$

where  $\boldsymbol{\sigma}$  is the stress corresponding to the field  $\mathbf{u}^*$ , because the right hand side (RHS) was originated from  $G(\mathbf{u}^*, \boldsymbol{\eta})$ .<sup>10</sup> Therefore we can compute an correction to the displacement from the state defined by the previous step.

<sup>7</sup>Another definition using limits is

$$\mathcal{D}G(\mathbf{u}^*, \boldsymbol{\eta})[\delta \mathbf{u}] \stackrel{\text{def}}{=} \lim_{\delta \mathbf{u} \rightarrow 0} \frac{G(\mathbf{u}^* + \delta \mathbf{u}) - G(\mathbf{u}^*)}{\delta \mathbf{u}} \quad (\text{B.5})$$

<sup>8</sup>Details on (de Souza Neto et al. 2008, p. 754)

<sup>9</sup>Note that the linearization occurred at a specific point  $\mathbf{u}^*$  and the goal is to find the displacement increment of the iteration  $\delta \mathbf{u}$ , which in the discretized version is given by the vector  $\delta \mathbf{u}$

<sup>10</sup>Note that  $\mathbf{u}$  and  $\boldsymbol{\eta}$  are still italic so they represent field and not finite element vectors, which are obtained by discretization of  $V$

## B.1. DISCRETIZATION OF THE LINEARIZED VIRTUAL WORK

The discretized version of (B.11) is,<sup>11</sup>

$$\left( \int_{^hV} (\mathbf{B}^g)^T \mathbf{D}^{(k)} \mathbf{B}^g dV \right) \delta \mathbf{u}^{(k+1)} = - \left( \int_{^hV} [(\mathbf{B}^g)^T \hat{\boldsymbol{\sigma}}^{(k)} - (\mathbf{N}^g)^T \mathbf{b}] dV - (\mathbf{N}^g)^T \mathbf{t} dA \right) \quad (\text{B.12})$$

where  $^hV$  is the discretization  $h$  of domain  $V$  by finite elements, the superscript  $g$  indicates global matrices. The right hand side of equation (B.12) above represents the residual for a global displacement vector  $\mathbf{u}_{n+1}^{(k)}$ . So, the above equation can be rewritten as a general iterative formula on the index  $k$  as<sup>12</sup>

$$\mathbf{K}_T^{(k)} \delta \mathbf{u}^{(k+1)} = -\mathbf{r}^{(k)}. \quad (\text{B.13})$$

We can compute the residual on the previous step as,

$$\mathbf{r}^{(k)} \stackrel{\text{def}}{=} \mathbf{f}^{\text{int}}(\mathbf{u}_{n+1}^{(k)}) - \mathbf{f}_{n+1}^{\text{ext}} \quad (\text{B.14})$$

and  $\mathbf{K}_T$  is the global tangent stiffness matrix, computed as

$$\mathbf{K}_T^{(k)} \stackrel{\text{def}}{=} \int_{^hV} (\mathbf{B}^g)^T \mathbf{D} \mathbf{B}^g dV. \quad (\text{B.15})$$

Therefore, solving for  $\delta \mathbf{u}$ , we can update the solution for the displacement until convergence is archived.

$$\mathbf{u}_{n+1}^{(k+1)} = \mathbf{u}_{n+1}^{(k)} + \delta \mathbf{u}^{(k+1)} \quad (\text{B.16})$$

This procedure is presented in algorithm 1.

## B.2. NUMERICAL INTEGRATION FOR ELASTOPLASTIC CONSTITUTIVE EQUATIONS

This section details the procedure for solving the nonlinear constitutive problem. At a given pseudo-time  $t_0$ , the elastic strain is  $\boldsymbol{\varepsilon}^e(t_0)$ , the plastic strain is  $\boldsymbol{\varepsilon}^p(t_0)$  and the set  $\boldsymbol{\alpha}(t_0)$  is the collection of internal hardening variables at a known point  $\mathbf{p}$ .

The problem is stated as: Given the initial values of  $\boldsymbol{\varepsilon}^e(t_0)$  and the internal hardening variables  $\boldsymbol{\alpha}(t_0)$  and given the history of the strain tensor  $\boldsymbol{\varepsilon}(t)$  for  $t \in [t_0, T]$ , find the functions  $\boldsymbol{\varepsilon}^e(t)$ ,  $\boldsymbol{\alpha}(t)$  and  $\dot{\gamma}(t)$  (plastic multiplier) that satisfy the reduced general elastoplastic constitutive equations.

$$\dot{\boldsymbol{\varepsilon}}^e(t) \stackrel{\text{def}}{=} \dot{\boldsymbol{\varepsilon}}(t) - \dot{\gamma}(t) \mathbf{N}, \quad \text{where, } \dot{\boldsymbol{\varepsilon}}^p \stackrel{\text{def}}{=} \dot{\gamma}(t) \mathbf{N}(\boldsymbol{\sigma}(t), \mathbf{A}(t)) \quad (\text{B.17})$$

$$\dot{\boldsymbol{\alpha}} \stackrel{\text{def}}{=} \dot{\gamma}(t) \mathbf{H}(\boldsymbol{\sigma}(t), \mathbf{A}(t)) \quad (\text{B.18})$$

$$\text{Loading, unloading condition} \quad (\text{B.19})$$

Where the plastic flow equation was incorporated in the additive strain rate decomposition, (B.17). The plastic strain does not appear explicitly in the system.  $\mathbf{A}$  is defined through potential relations.  $\mathbf{N}$  is the flow vector and  $\mathbf{H}$  is an associative hardening rule.

<sup>11</sup>It was used the convention presented in appendix E

<sup>12</sup>Note that  $\boldsymbol{\sigma}$  is the vector representation of the stress tensor  $\boldsymbol{\sigma}$

The time discretization of the constitutive equations is done using backward Euler scheme (fully implicit). For integration in a generic time interval  $[t_n, t_{n+1}]$ , the system becomes,

$$\boldsymbol{\varepsilon}_{n+1}^e \stackrel{\text{def}}{=} \boldsymbol{\varepsilon}_n^e + \Delta\boldsymbol{\varepsilon} - \Delta\gamma(t)\mathbf{N} \quad (\text{B.20})$$

$$\boldsymbol{\alpha}_{n+1} \stackrel{\text{def}}{=} \boldsymbol{\alpha}_n + \Delta\gamma\mathbf{H} \quad (\text{B.21})$$

where the unknowns are  $\boldsymbol{\varepsilon}_{n+1}^e$ ,  $\boldsymbol{\alpha}_{n+1}$  and  $\Delta\gamma$  with the loading/unloading constraints,

$$\Delta\gamma \geq 0, \quad \Phi(\boldsymbol{\sigma}_{n+1}, \mathbf{A}_{n+1}) \leq 0, \quad \Delta\gamma\Phi(\boldsymbol{\sigma}_{n+1}, \mathbf{A}_{n+1}) = 0 \quad (\text{B.22})$$

In which  $(\cdot)_n$  denotes the variable  $(\cdot)$  at time  $t_n$ .

The solution of the incremental problem is done using a two step algorithm (de Souza Neto et al. 2008, p. 193). Only two possibilities, mutually exclusive, are possible:

1. Null incremental plastic multiplier

$$\Delta\gamma = 0 \quad (\text{B.23})$$

which means that there is no plastic flow,  $\dot{\boldsymbol{\varepsilon}}^p = 0$  and no evolution of internal variables  $\dot{\boldsymbol{\alpha}} = 0$ . This step is purely elastic. The evolution of the unknowns are straightforward

$$\boldsymbol{\varepsilon}_{n+1}^e = \boldsymbol{\varepsilon}_n^e + \Delta\boldsymbol{\varepsilon} \quad (\text{B.24})$$

$$\quad (\text{B.25})$$

$$\boldsymbol{\alpha}_{n+1} = \boldsymbol{\alpha}_n. \quad (\text{B.26})$$

and the yield function must satisfy the condition  $\Phi \leq 0$  which indicates the elastic domain.

2. Positive plastic multiplier

$$\Delta\gamma > 0 \quad (\text{B.27})$$

In this case, the unknowns satisfy the constitutive equations, presented in (B.20) and (B.21). Those equations simply represent the additive properties of strain and the evolution of the internal hardening variables. Also, the yield function for this case is null,  $\Phi = 0$ .

The strategy for implementation is called *return mapping algorithm* and it consists of defining an elastic trial step,

$$\boldsymbol{\varepsilon}_{n+1}^{e \text{ trial}} = \boldsymbol{\varepsilon}_n^e + \Delta\boldsymbol{\varepsilon} \quad (\text{B.28})$$

$$\boldsymbol{\alpha}_{n+1}^{\text{trial}} = \boldsymbol{\alpha}_n \quad (\text{B.29})$$

where, the strain increment,  $\Delta\boldsymbol{\varepsilon}$  is defined a priori. Then check the yield criteria and update the state variables by solving a nonlinear system with the Newton Raphson, or solve analytically in the case of isotropic hardening and von Mises yield criteria as shown in later sections.

### B.3. CONSTITUTIVE MODEL CONSIDERING VON MISES YIELD CRITERIA

This constitutive model is the set of equations that govern the material behavior.

The model considering the von Mises yield criteria contains,

1. Linear elastic constitutive law,

$$\boldsymbol{\sigma} \stackrel{\text{law}}{=} \mathbf{D}^e : \boldsymbol{\varepsilon}^e \quad (\text{B.30})$$

2. In this particular case, the yield function is given by,

$$\Phi = \Phi(\boldsymbol{\sigma}, \sigma_y) = \sqrt{3J_2(\mathbf{s}(\boldsymbol{\sigma}))} - \sigma_y \quad (\text{B.31})$$

where  $\sigma_y = \sigma_y(\bar{\varepsilon}^p)$ , the yield stress is a function of the accumulated plastic strain which accounts for creation of new dislocations in the material which increases the strength of the material. The  $J_2$  is the second invariant of the deviatoric stress tensor.

3. The flow rule is given by,

$$\dot{\boldsymbol{\varepsilon}}^p \stackrel{\text{def}}{=} \dot{\gamma} \mathbf{N} \quad (\text{B.32})$$

where the flow vector (Prandtl-Reuss) is defined with,

$$\mathbf{N} \stackrel{\text{def}}{=} \frac{\partial \Phi}{\partial \boldsymbol{\sigma}} \equiv \sqrt{\frac{3}{2}} \frac{\mathbf{s}}{\|\mathbf{s}\|} \quad (\text{B.33})$$

4. A hardening rule, where the internal variable of interest is the equivalent plastic strain and its evolution is given by,

$$\dot{\bar{\varepsilon}}^p = \sqrt{\frac{2}{3}} \|\dot{\boldsymbol{\varepsilon}}^p\| \equiv \dot{\gamma} \quad (\text{B.34})$$

#### B.4. SINGLE EQUATION RETURN MAPPING

In order to update de state variables of the model based on the strain increment we use a return mapping algorithm.

The nonlinear system of the return mapping can be reduced to a single equation when considering the von Mises model. First, we start from a general load step  $n + 1$  and we know the variable values at the previous step  $n$ . At this pseudo-time step, we have the incremental displacement vector  $\delta \mathbf{u}$  and our goal is to compute the next increment  $\delta \mathbf{u}$ . We start by computing the update displacement at all nodes,

$$\mathbf{u}_{n+1}^{(k+1)} = \mathbf{u}_{n+1}^{(k)} + \delta \mathbf{u}^{(k+1)} \quad (\text{B.35})$$

Note that the first iteration  $k = 0$ , the displacement increment is  $\delta \mathbf{u}^{(k)} = 0$  and at the beginning of every iteration the increment is set to zero. Next, we compute the strain increment at each gauss point of each element,

$$\Delta \boldsymbol{\varepsilon} = \mathbf{B} \delta \mathbf{u}^{(e)} \quad (\text{B.36})$$

We then use this strain increment<sup>13</sup> to compute the *elastic* trial strain at the pseudo-time step  $n + 1$ ,

$$\boldsymbol{\varepsilon}_{n+1}^{e \text{ trial}} = \boldsymbol{\varepsilon}_n^e + \Delta \boldsymbol{\varepsilon} \quad (\text{B.37})$$

Note that we need the *elastic* strain from the previous step  $n$ , this is computed by the return-mapping function. This trial strain is then decomposed in a deviatoric and volumetric part.

$$\boldsymbol{\varepsilon}_{v \ n+1}^{e \text{ trial}} \stackrel{\text{def}}{=} \text{tr}(\boldsymbol{\varepsilon}_{n+1}^{e \text{ trial}}), \quad \boldsymbol{\varepsilon}_{d \ n+1}^{e \text{ trial}} \stackrel{\text{def}}{=} \boldsymbol{\varepsilon}_{n+1}^{e \text{ trial}} - \frac{1}{3} \boldsymbol{\varepsilon}_{v \ n+1}^{e \text{ trial}} \mathbf{I} \quad (\text{B.38})$$

<sup>13</sup>Note that  $\delta \mathbf{u}^{(e)(k)}$  corresponds to the values referent to a particular element, so we need to slice the global displacement increment array.

Considering the volumetric/deviatoric decomposition of strains, and the fact that the flow vector using the effective von Mises stress is purely deviatoric, we have

$$\boldsymbol{\varepsilon}_{d\,n+1}^e \stackrel{\text{def}}{=} \boldsymbol{\varepsilon}_{d\,n+1}^{e\ \text{trial}} - \Delta\gamma \sqrt{\frac{3}{2}} \frac{\mathbf{s}_{n+1}}{\|\mathbf{s}_{n+1}\|} \quad (\text{B.39})$$

which, in terms of stresses (multiply by  $2G$ ),

$$\mathbf{s}_{n+1} \stackrel{\text{def}}{=} \mathbf{s}_{n+1}^{\text{trial}} - \Delta\gamma 2G \sqrt{\frac{3}{2}} \frac{\mathbf{s}_{n+1}}{\|\mathbf{s}_{n+1}\|} \quad (\text{B.40})$$

the plastic multiplier  $\Delta\gamma$  only affects the deviatoric part, so the hydrostatic part can be removed from the nonlinear system. Rearranging the terms in Eq. (B.40), we get,

$$\mathbf{s}_{n+1}^{\text{trial}} \stackrel{\text{def}}{=} \mathbf{s}_{n+1} \left( 1 + \sqrt{\frac{3}{2}} \frac{\Delta\gamma 2G}{\|\mathbf{s}_{n+1}\|} \right) \quad (\text{B.41})$$

which implies a linear relation between the trial and updated deviatoric stresses. Because of the linear property, we can write the following ratio relation

$$\frac{\mathbf{s}_{n+1}}{\|\mathbf{s}_{n+1}\|} = \frac{\mathbf{s}_{n+1}^{\text{trial}}}{\|\mathbf{s}_{n+1}^{\text{trial}}\|} \quad (\text{B.42})$$

substituting this relation, Eq. (B.42), into Eq. (B.40), and considering  $q \stackrel{\text{def}}{=} \sqrt{3/2} \|\mathbf{s}\|$ ,

$$\mathbf{s}_{n+1} \stackrel{\text{def}}{=} \mathbf{s}_{n+1}^{\text{trial}} \left( 1 - \frac{\Delta\gamma 3G}{q_{n+1}^{\text{trial}}} \right). \quad (\text{B.43})$$

Substituting this results, Eq. (B.43), and the evolution of accumulated plastic strain (internal variable) into the yield function we obtain the single return mapping equation, (de Souza Neto et al. 2008, Eq. 7.91),

$$\tilde{\Phi} \stackrel{\text{def}}{=} \sqrt{3J_2(\mathbf{s}_{n+1})} - \sigma_y(\bar{\varepsilon}_{n+1}^p) \quad (\text{B.44})$$

$$\equiv \sqrt{\frac{3}{2}} \|\mathbf{s}_{n+1}\| - \sigma_y(\bar{\varepsilon}_n^p + \Delta\gamma) \quad (\text{B.45})$$

$$\equiv \sqrt{\frac{3}{2}} \|\mathbf{s}_{n+1}^{\text{trial}} \left( 1 - \frac{\Delta\gamma 3G}{q_{n+1}^{\text{trial}}} \right)\| - \sigma_y(\bar{\varepsilon}_n^p + \Delta\gamma) \quad (\text{B.46})$$

$$\equiv \sqrt{\frac{3}{2}} \|\mathbf{s}_{n+1}^{\text{trial}}\| \left( 1 - \frac{\Delta\gamma 3G}{q_{n+1}^{\text{trial}}} \right) - \sigma_y(\bar{\varepsilon}_n^p + \Delta\gamma) \quad (\text{B.47})$$

$$\equiv q_{n+1}^{\text{trial}} \left( 1 - \frac{\Delta\gamma 3G}{q_{n+1}^{\text{trial}}} \right) - \sigma_y(\bar{\varepsilon}_n^p + \Delta\gamma) \quad (\text{B.48})$$

$$\equiv q_{n+1}^{\text{trial}} - 3G\Delta\gamma - \sigma_y(\bar{\varepsilon}_n^p + \Delta\gamma) = 0 \quad (\text{B.49})$$

After solving the above equation, Eq. (B.49), for the unknown  $\Delta\gamma$  using a local Newton-Raphson, the variables can be updated with,

$$\mathbf{s}_{n+1} \stackrel{\text{def}}{=} \mathbf{s}_{n+1}^{\text{trial}} \left( 1 - \frac{\Delta\gamma 3G}{q_{n+1}^{\text{trial}}} \right) \quad (\text{B.50})$$

$$\boldsymbol{\sigma}_{n+1} \stackrel{\text{def}}{=} \mathbf{s}_{n+1} + p_{n+1}^{\text{trial}} \mathbf{I} \quad (\text{B.51})$$

$$\boldsymbol{\varepsilon}_{n+1}^e \stackrel{\text{def}}{=} [\mathbf{D}^e]^{-1} : \boldsymbol{\sigma}_{n+1} \equiv \frac{1}{2G} \mathbf{s}_{n+1} + \frac{1}{3} \varepsilon_{v\,n+1}^{e\ \text{trial}} \quad (\text{B.52})$$

$$\bar{\varepsilon}_{n+1}^p \stackrel{\text{def}}{=} \bar{\varepsilon}_n^p + \Delta\gamma \quad (\text{B.53})$$

This procedure is implemented in algorithm 2.

## B.5. GENERAL ELASTOPLASTIC CONSISTENT TANGENT CONSTITUTIVE OPERATOR FOR IMPLICIT RETURN MAPPINGS

From (de Souza Neto et al. 2008, sec. 7.4.4). The returning map equations for the solution of the constitutive model at each gauss point is,

$$\begin{Bmatrix} \boldsymbol{\varepsilon}_{n+1}^e - \boldsymbol{\varepsilon}_{n+1}^{e \text{ trial}} + \Delta\gamma \mathbf{N}_{n+1} \\ \boldsymbol{\alpha}_{n+1} - \boldsymbol{\alpha}_n - \Delta\gamma \mathbf{H}_{n+1} \\ \Phi(\boldsymbol{\sigma}_{n+1}, \mathbf{A}_{n+1}) \end{Bmatrix} = \begin{Bmatrix} \mathbf{0} \\ \mathbf{0} \\ \mathbf{0} \end{Bmatrix} \quad (\text{B.54})$$

where  $\mathbf{H}_{n+1}$  is the generalized hardening modulus which defines the evolution of hardening variables, and  $\mathbf{A}_{n+1}$  is the hardening thermodynamic forces. The unknowns are  $\boldsymbol{\varepsilon}_{n+1}^e$ , which can recuperate the updated stresses, the set of internal variables,  $\boldsymbol{\alpha}$  and the plastic multiplier  $\Delta\gamma$ . In order to compute the derivative of the stress, the consistent tangent modulus, we need to linearized the returning map equations. This linearization yields the system,

$$\begin{bmatrix} \mathbf{C} + \Delta\gamma \frac{\partial \mathbf{N}}{\partial \boldsymbol{\sigma}} & \mathbf{B} + \Delta\gamma \frac{\partial \mathbf{N}}{\partial \mathbf{A}} & \mathbf{N} \\ \mathbf{A} - \Delta\gamma \frac{\partial \mathbf{H}}{\partial \boldsymbol{\sigma}} & \mathbf{J} - \Delta\gamma \frac{\partial \mathbf{H}}{\partial \mathbf{A}} & -\mathbf{H} \\ \frac{\partial \Phi}{\partial \boldsymbol{\sigma}} & \frac{\partial \Phi}{\partial \mathbf{A}} & 0 \end{bmatrix} \begin{bmatrix} d\boldsymbol{\sigma} \\ d\mathbf{A} \\ d\Delta\gamma \end{bmatrix} = \begin{bmatrix} d\boldsymbol{\varepsilon}^{e \text{ trial}} \\ 0 \\ 0 \end{bmatrix} \quad (\text{B.55})$$

where the subscript  $n + 1$  was omitted. By inverting the relation we get,

$$d\boldsymbol{\sigma} = \mathbf{D}_{11} d\boldsymbol{\varepsilon}^{e \text{ trial}} \quad (\text{B.56})$$

where  $\mathbf{D}_{11} = \mathbf{D}^{ep}$  is the elastoplastic consistent tangent modulus and it represents the first set of terms from the inverse of the above matrix.

For the particular case of using von Mises yield criteria and isotropic hardening, a couple of simplification can be made, see (de Souza Neto et al. 2008, sec. 6.6.3). First, the set of internal variables is reduced to one scalar  $\boldsymbol{\alpha} = \{\bar{\varepsilon}^p\}$ , the accumulated plastic strain. The set of thermodynamic forces is reduced to the scalar  $\kappa = \kappa(\bar{\varepsilon}^p)$ , which is a function of the accumulated plastic strain (could be linear or nonlinear). The associative evolution equation of the internal variable is simply  $\dot{\bar{\varepsilon}}^p = \dot{\gamma}$ .

Using that, we have

$$\frac{\partial \mathbf{H}}{\partial \boldsymbol{\sigma}} = 0; \quad \frac{\partial \mathbf{H}}{\partial \mathbf{A}} = \mathbf{0}. \quad (\text{B.57})$$

The operators  $\mathbf{B} = \mathbf{A} = \mathbf{0}$ , the only operators that don't vanish are  $\mathbf{C} = [\mathbf{D}^e]^{-1}$ ,<sup>14</sup> and  $\mathbf{J} = 1/H$ , where  $H$  is the hardening modulus.<sup>15</sup> All that together generates a system,

$$\begin{bmatrix} [\mathbf{D}^e]^{-1} + \Delta\gamma \frac{\partial \mathbf{N}}{\partial \boldsymbol{\sigma}} & \mathbf{0} & \mathbf{N} \\ \mathbf{0} & \frac{1}{H} & -1 \\ \mathbf{N} & -1 & 0 \end{bmatrix} \begin{bmatrix} d\boldsymbol{\sigma} \\ d\mathbf{A} \\ d\Delta\gamma \end{bmatrix} = \begin{bmatrix} d\boldsymbol{\varepsilon}^{e \text{ trial}} \\ 0 \\ 0 \end{bmatrix} \quad (\text{B.58})$$

<sup>14</sup>This is the dependence of the model in the elastic properties, at this point we can use the multiscale model to generate a homogenized elastic constitutive matrix.

<sup>15</sup>considering a linear relation between the yield stress and accumulated plastic strain,  $\sigma_y = \sigma_{y0} + H\bar{\varepsilon}^p$ .

the tangential relation is then obtained by inverting this matrix, which results in (de Souza Neto et al. 2008, Eq. 7.148),

$$\mathbf{D}^{ep} = \mathbf{P} - \frac{1}{\mathbf{N} : \mathbf{P} : \mathbf{N} + H} (\mathbf{N} : \mathbf{P}) \otimes (\mathbf{P} : \mathbf{N}) \quad (\text{B.59})$$

where,

$$\mathbf{P} \equiv \left( \mathbf{I}_S + \Delta\gamma \mathbf{D}^e : \frac{\partial \mathbf{N}}{\partial \boldsymbol{\sigma}} \right)^{-1} : \mathbf{D}^e \quad (\text{B.60})$$

The fourth order symmetric identity tensor,  $\mathbf{I}_S$  has as a matrix equivalent for computational implementation for the 2D problems,  $\mathbf{I}_S$ ,

$$\mathbf{I}_S \stackrel{\text{def}}{=} \begin{bmatrix} 1 & 0 & 0 \\ & 1 & 0 \\ \text{sym.} & & \frac{1}{2} \end{bmatrix}. \quad (\text{B.61})$$

Note the notation for computer implementation matrix, the sans-serif font is substituted to serif types. The double contraction operation between a fourth order tensor and a second order becomes,

$$\mathbf{N} : \mathbf{P} : \mathbf{N} \stackrel{\text{def}}{=} \mathbf{N}^T \mathbf{P} \mathbf{N} \quad (\text{B.62})$$

The flow vector considering the von Mises yield criteria,

$$\mathbf{N} \stackrel{\text{def}}{=} \sqrt{\frac{3}{2}} \frac{\mathbf{s}}{\|\mathbf{s}\|} \quad (\text{B.63})$$

where  $\mathbf{s}$  is the deviatoric stress,

$$\mathbf{s} \stackrel{\text{def}}{=} \boldsymbol{\sigma} - p \mathbf{I} \quad (\text{B.64})$$

where  $p \stackrel{\text{def}}{=} \frac{1}{3} \text{tr}(\boldsymbol{\sigma})$  is the hydrostatic stress. The relation between shear and bulk modulus with respect to Young's modulus and Poisson's ration is,

$$G \stackrel{\text{def}}{=} \frac{E}{2(1 + \nu)}, \quad K \stackrel{\text{def}}{=} \frac{E}{3(1 - 2\nu)} \quad (\text{B.65})$$

and the following relations are valid,

$$p \stackrel{\text{def}}{=} K \varepsilon_v^e, \quad \mathbf{s} \stackrel{\text{def}}{=} 2G \boldsymbol{\varepsilon}_d^e \quad (\text{B.66})$$

where  $\varepsilon_v^e = \text{tr}(\boldsymbol{\varepsilon}^e)$  is the volumetric part of the elastic strain, and  $\boldsymbol{\varepsilon}_d^e$  is the deviatoric part. The second order identity tensor in its computer implementation form is represented by,

$$\mathbf{I} \equiv \mathbf{i} \stackrel{\text{def}}{=} \begin{bmatrix} 1 \\ 1 \\ 0 \end{bmatrix} \quad (\text{B.67})$$

## B.6. ELASTOPLASTIC CONSISTENT TANGENT FOR VON MISES MODEL WITH ISOTROPIC HARDENING

This particular case have the following formula for the consistent tangent constitutive modulus (de Souza Neto et al. 2008, Eq. 7.120)

$$\mathbf{D}^{ep} \stackrel{\text{def}}{=} 2G \left( 1 - \frac{\Delta\gamma 3G}{q_{n+1}^{\text{trial}}} \right) \mathbf{I}_d + 6G^2 \left( \frac{\Delta\gamma}{q_{n+1}^{\text{trial}}} - \frac{1}{3G + H} \right) \bar{\mathbf{N}} \otimes \bar{\mathbf{N}} + K \mathbf{I} \otimes \mathbf{I} \quad (\text{B.68})$$

where  $\bar{\mathbf{N}} = \sqrt{\frac{2}{3}} \mathbf{N}$  is the unit flow vector defined in (de Souza Neto et al. 2008, Eq. 7.117), and computed using the deviatoric stress tensor,

$$\bar{\mathbf{N}} \stackrel{\text{def}}{=} \frac{\mathbf{s}}{\|\mathbf{s}\|}. \quad (\text{B.69})$$

The effective von Mises stress is computed with,

$$\sigma_{\text{eq}} \equiv q \stackrel{\text{def}}{=} \sqrt{3J_2} \equiv \sqrt{\frac{3}{2}} \|\mathbf{s}\| \quad (\text{B.70})$$

The tensor  $\mathbf{I}_d$  is the forth order deviatoric projection tensor given by  $\mathbf{I}_d \stackrel{\text{def}}{=} \mathbf{I}_s - \mathbf{I} \otimes \mathbf{I}$ . Note, in the code presented in (de Souza Neto et al. 2008, sec. 7.4.3), the trial effective von Mises stress is computed with  $q = \sqrt{3/2} \|\mathbf{s}\| + 3G\Delta\gamma$ <sup>16</sup>. In Voigt notation, appendix E, the elastoplastic tangent matrix is computed with,

$$\mathbf{D}^{ep} = 2G \left( 1 - \frac{3\Delta\gamma}{q^{\text{trial}}} \right) \mathbf{I}_d + 6G^2 \left( \frac{\Delta\gamma}{q^{\text{trial}}} - \frac{1}{3G + H} \right) \frac{1}{\|\mathbf{s}\|^2} \mathbf{ss}^T + K \mathbf{ii}^T \quad (\text{B.75})$$

The elastic tangent operator is given by (de Souza Neto et al. 2008, eq. 7.107),

$$\mathbf{D}^e \stackrel{\text{def}}{=} 2G \mathbf{I}_s + K \mathbf{I} \otimes \mathbf{I} \quad (\text{B.76})$$

---

<sup>16</sup>He recovered the last von Mises effective stress with  $q = \sqrt{\frac{3}{2}} \|\mathbf{s}\|$ , then used this value to find the new trial effective stress  $q^{\text{trial}} = q + 2G\Delta\gamma$ . The trial effective von Mises is given by,

$$q_{n+1}^{\text{trial}} = \sqrt{3J_2(\mathbf{s}_{n+1}^{\text{trial}})} = \sqrt{\frac{3}{2}} \|\mathbf{s}_{n+1}^{\text{trial}}\| \quad (\text{B.71})$$

but, only the converged value of  $\sigma_{n+1}$  is passed to the `ctvm` function. So using the update equation for the deviatoric stress,

$$\mathbf{s}_{n+1} = \left( 1 - \frac{3G\Delta\gamma}{q_{n+1}^{\text{trial}}} \right) \mathbf{s}_{n+1}^{\text{trial}} \quad (\text{B.72})$$

inside the effective stress definition, we get

$$q_{n+1}^{\text{trial}} = \sqrt{\frac{3}{2}} \frac{\|\mathbf{s}_{n+1}\|}{\left( 1 - \frac{3G\Delta\gamma}{q_{n+1}^{\text{trial}}} \right)} \quad (\text{B.73})$$

which results in,

$$q_{n+1}^{\text{trial}} = \sqrt{\frac{3}{2}} \|\mathbf{s}_{n+1}\| + 3G\Delta\gamma \quad (\text{B.74})$$

where  $\|\mathbf{s}_{n+1}\|$  is compute based on the converged value for the stress tensor.

which in Voigt notation for computer implementation, appendix E, becomes

$$\mathbf{D}^e = 2G\mathbf{I}_s + K\mathbf{ii}^T \quad (\text{B.77})$$

This procedure is in algorithm 3.

### C. EXTENDED FINITE ELEMENTS

In this section some aspects of the mathematical description of the eXtended finite elements are discussed. This method will be used to model a highly heterogeneous material in order to compare with the multiscale procedure.

The eXtended finite element method (XFEM) is a numerical method that extends the classical finite element method (FEM) by adding additional degree's of freedom with local enrichments. One of the main advances of the method is to approximate solution with non-smooth characteristics.

One particular case of problem that presents non-smooth properties is the mechanical analysis of composite materials. In this case, stress and strain field are not continuous across the material boundary.

Discontinuities are classified accordingly to the jump in the gradient of the field, they can be strong or weak. If the gradient presents a jump the discontinuity is called strong. Weak discontinuity is characterized by a kink in the gradient distribution.

The enhanced approximation for an element displacement function is given by the sum of the standard FEM approximation and additional functions,

$$\mathbf{u}(\mathbf{x}, t) \approx \mathbf{u}^h(\mathbf{x}, t) \stackrel{\text{def}}{=} \sum_{i=1}^{\mathcal{N}} N_i(\boldsymbol{\xi}) \mathbf{u}_i + \sum_{j=1}^{\mathcal{M}} N_j(\boldsymbol{\xi}) (\psi(\mathbf{x}) - \psi(\mathbf{x}_j)) \mathbf{a}_j \quad (\text{C.1})$$

$$\equiv \mathbf{N}_{(\boldsymbol{\xi})}^{\text{std}} \mathbf{u} + \mathbf{N}_{(\boldsymbol{\xi})}^{\text{enr}} \mathbf{a}, \quad \mathbf{x} \in V^{(e)} \quad (\text{C.2})$$

where  $\psi(\mathbf{x})$  is the enrichment function. The form  $\psi(\mathbf{x}) - \psi(\mathbf{x}_j)$  is known as shifted enrichment function and is important to ensure that the function is approximated by the generalized coordinates at the nodes, i.e.,  $\mathbf{u}(\mathbf{x}_k) = \mathbf{u}_k$ . This allows one to enforce the boundary conditions directly in the linear system the same way as in the standard finite element method.

$\mathcal{N}$  and  $\mathcal{M}$  are the number of standard shape function and the number of enrichment functions. The vectors  $\mathbf{u}$  and  $\mathbf{a}$  contain the standard dof constant unknown and the new enrichment dof unknown respectively.

For the plane problem the shape function matrices are given by,

$$\mathbf{N}_i^{\text{std}}(\boldsymbol{\xi}) \stackrel{\text{def}}{=} \begin{bmatrix} N_i(\boldsymbol{\xi}) & 0 \\ 0 & N_i(\boldsymbol{\xi}) \end{bmatrix} \quad (\text{C.3})$$

$$\mathbf{N}_j^{\text{enr}}(\boldsymbol{\xi}) \stackrel{\text{def}}{=} \begin{bmatrix} N_j(\boldsymbol{\xi}) (\psi(\mathbf{x}) - \psi(\mathbf{x}_j)) & 0 \\ 0 & N_j(\boldsymbol{\xi}) (\psi(\mathbf{x}) - \psi(\mathbf{x}_j)) \end{bmatrix} \quad (\text{C.4})$$

where, for quad elements, the shape functions given in isoparametric coordinates  $\boldsymbol{\xi} = (\xi, \eta)$  are expressed by  $N_k(\xi, \eta) = \frac{1}{4} (1 - \xi_k \xi) (1 - \eta_k \eta)$ , with  $k = 1, 2, 3, 4$  and  $(\xi_k, \eta_k)$  the nodes coordinates of the master element in the isoparametric coordinate system.

Substituting the approximation (C.1) into the weak form for the equilibrium equations we arrive at a system,

$$\begin{bmatrix} \mathbf{K}_{\text{uu}} & \mathbf{K}_{\text{ua}} \\ \mathbf{K}_{\text{au}} & \mathbf{K}_{\text{aa}} \end{bmatrix} \begin{Bmatrix} \mathbf{u} \\ \mathbf{a} \end{Bmatrix} = \begin{Bmatrix} \mathbf{f}_u^{\text{ext}} \\ \mathbf{f}_a^{\text{ext}} \end{Bmatrix} \quad (\text{C.5})$$

where, the subscripts  $\mathbf{u}$  and  $\mathbf{a}$  refer to *standard* and *enriched* respectively. The stiffness matrix is computed with

$$\mathbf{K}_{\alpha\beta}^{(e)} \stackrel{\text{def}}{=} \int_{V^{(e)}} (\mathbf{B}^\alpha)^T \mathbf{D} \mathbf{B}^\beta dV, \quad \alpha, \beta = \text{std}, \text{enr} \quad (\text{C.6})$$

and the external load vector,

$$\mathbf{f}_\alpha^{\text{ext}} \stackrel{\text{def}}{=} \int_{S_t^{(e)}} (\mathbf{N}^\alpha)^T \mathbf{t} dS + \int_{V^{(e)}} (\mathbf{N}^\alpha)^T \mathbf{b} dV \quad \alpha = \text{std}, \text{enr} \quad (\text{C.7})$$

### C.1. LEVEL SET FUNCTION

The level set function is used to define the discontinuities interface and is defined as a sign distance,

$$\phi(\mathbf{x}) \stackrel{\text{def}}{=} \|\mathbf{x} - \mathbf{x}^*\| \text{sign}(\mathbf{n} \cdot (\mathbf{x} - \mathbf{x}^*)) \quad (\text{C.8})$$

where the variables are depicted in fig. C.1. The point  $\mathbf{x}^*$  is the closest from a general  $\mathbf{x}$  to the discontinuity surface. The zero level set indicates the discontinuity interface,  $\phi(\mathbf{x}^*) = 0$ . The inner product will indicate if the point is inside or outside the inclusion. If the inner product is negative then the point is inside.

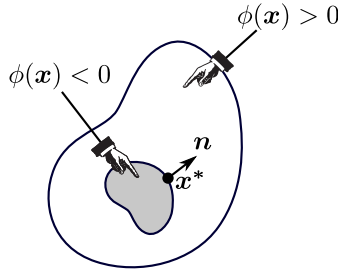


Figure C.1. Level set function definition.

### C.2. ENRICHMENT FUNCTIONS FOR WEAK DISCONTINUITY

The shifted ramp enrichment is often employed for weak discontinuity, different material inclusions for instance,

$$\bar{\psi}_i = |\phi(\mathbf{x})| - |\phi(\mathbf{x}_i)| \quad (\text{C.9})$$

where  $\phi(\mathbf{x})$  is the level set function defined in the previous section. The level set function is conveniently interpolated in an element using the standard shape functions,

$$\phi(\mathbf{x}) = \sum_{i=1}^{\mathcal{N}} N_i(\boldsymbol{\xi}) \phi_i \quad (\text{C.10})$$

where  $\phi_i$  is the nodal value of the level set function. The shifted ramp function ensures that the nodal values are consistent with the standard finite element. In this case, the derivative with respect to spatial coordinates yields,

$$\frac{\partial \bar{\psi}(\mathbf{x})}{\partial \mathbf{x}} = \text{sign}(\phi(\mathbf{x})) \frac{\partial \phi(\mathbf{x})}{\partial \mathbf{x}} \quad (\text{C.11})$$

in which the derivative of the level set function can be obtained by using the approximation in eq. (C.10). This represents a convenient approximation that improves accuracy as the mesh is refined, (Khoei 2015, p. 41).

$$\frac{\partial \phi(\mathbf{x})}{\partial \mathbf{x}} = \sum_{i=1}^{\mathcal{N}} \frac{\partial N_i(\boldsymbol{\xi})}{\partial \mathbf{x}} \phi_i \quad (\text{C.12})$$

Then we can compute a component of the enriched discretized gradient operator,

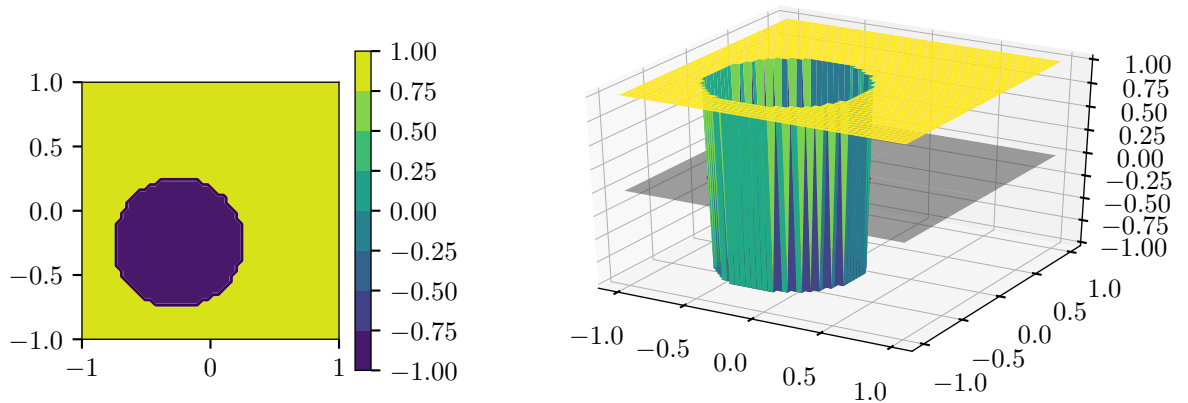
$$\frac{\partial N_i(\boldsymbol{\xi}) \bar{\psi}_i(\mathbf{x})}{\partial x} = \frac{\partial N_i(\boldsymbol{\xi})}{\partial x} \bar{\psi}_i(\mathbf{x}) + N_i(\boldsymbol{\xi}) \frac{\partial \bar{\psi}_i(\mathbf{x})}{\partial x} \quad (\text{C.13})$$

using eq. (C.12) and eq. (C.11) the component becomes,

$$\begin{aligned} \frac{\partial N_i(\boldsymbol{\xi}) \bar{\psi}_i(\mathbf{x})}{\partial x} = \frac{\partial N_i(\boldsymbol{\xi})}{\partial x} \left( \left| \sum_{i=1}^{\mathcal{N}} N_i(\boldsymbol{\xi}) \phi_i \right| - |\phi_i| \right) \\ + N_i(\boldsymbol{\xi}) \text{sign} \left( \sum_{i=1}^{\mathcal{N}} N_i(\boldsymbol{\xi}) \phi_i \right) \sum_{i=1}^{\mathcal{N}} \frac{\partial N_i(\boldsymbol{\xi})}{\partial x} \phi_i. \end{aligned} \quad (\text{C.14})$$

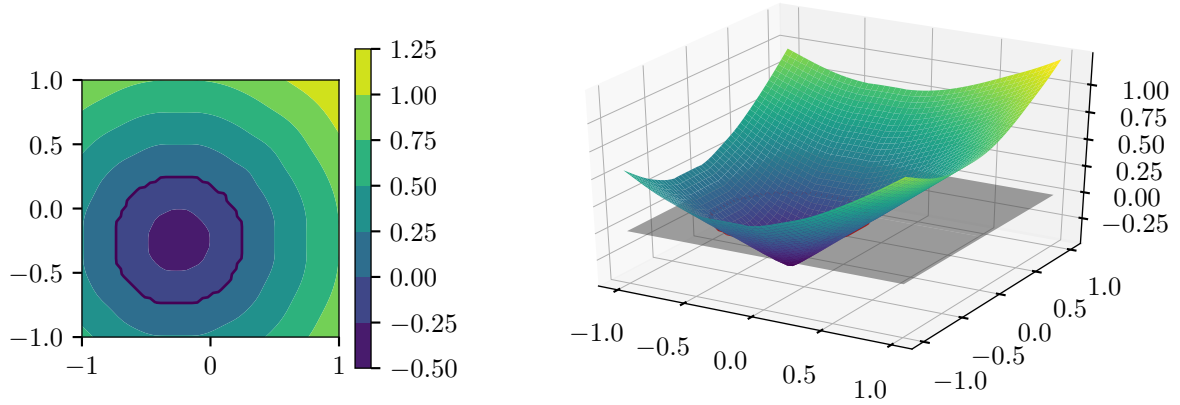
In the implementation, the shape functions are evaluated at the gauss points. The only extra information required differently from the standard finite elements is the level set value at the nodes. This value is obtained using a module (`scikit-fmm`) that computes the distance of a zero level set from a regular grid, then the distance value is interpolated from this grid into the Finite Element mesh.

Figure C.2 shows a zero level set definition in which the inclusion material is defined by -1 values and the matrix is equal to 1. The inclusion shape, or interface, is obtained when the function is equal to zero which is the definition of the zero level set. In this case, -1 and 1 were used so it is clear where the zero level set is, however any function can be used to define an inclusion interface.



**Figure C.2.** Interface definition with 2d array of 1 and -1.

Then using an external function to compute the distance of grid points (independent of the FEM mesh) to the zero level set we get a distance function shown in fig. C.3. This function is then interpolated to the mesh nodes to form the array  $\phi_i$ . The nodal values of the distance function is used to find if the element contains the discontinuity interface. A method is used to



**Figure C.3.** Distance of grid points to the zero level set, which defines the inclusion interface.

check the distance function sign in a particular element. If the distance function is negative on a node means that the discontinuity cross the element, and this element is marked for enrichment. If all distance values are negative, means that the whole element is inside the inclusion. Doing that for all nodes we can classify the standard and enriched nodes, see fig. C.4.

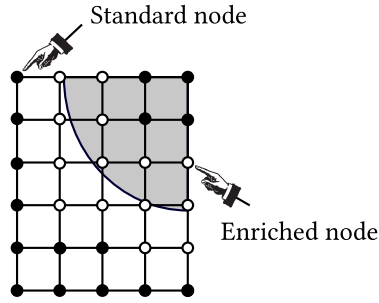


**Figure C.4.** Enriched nodes and regular nodes in the presence of a discontinuity.

## D. IMPLEMENTATION ASPECTS

### D.1. DISCRETIZED EQUILIBRIUM EQUATION

This section details the conversion between continuum mechanics to a discrete system of equations using standard finite element procedures.

Considering the weak form of equilibrium,

$$\int_V \boldsymbol{\sigma} : \nabla^s \boldsymbol{\eta} - \mathbf{b} \cdot \boldsymbol{\eta} dV - \int_S \mathbf{t} \cdot \boldsymbol{\eta} dS = 0 \quad (\text{D.1})$$

Substituting the standard fem approximation for the displacement and test function,

$$\int_{hV} \boldsymbol{\sigma}^T \mathbf{B}^g \boldsymbol{\eta} - \mathbf{b} \cdot \mathbf{N}^g \boldsymbol{\eta} dV - \int_{hS} \mathbf{t} \cdot \mathbf{N}^g \boldsymbol{\eta} dS = 0 \quad (\text{D.2})$$

where we notice the change from tensor notation  $\boldsymbol{\sigma}$  to vector Voigt's notation  $\boldsymbol{\sigma}$ . The superscript  $g$  in the shape function and discretized gradient operator means that they are global matrices.

This eq. (D.2) can be simplified to,

$$\int_{h_V} (\mathbf{B}^g)^T \boldsymbol{\sigma} - (\mathbf{N}^g)^T \mathbf{b} dV - \int_{h_S} (\mathbf{N}^g)^T \mathbf{t} dS = 0 \quad (\text{D.3})$$

## D.2. HOMOGENIZED TANGENT CONSTITUTIVE OPERATOR FOR THE GENERAL CASE

In this appendix it will be discussed how to compute the homogenized constitutive tangent operator for any assumption for the RVE displacement fluctuation. The homogenized constitutive tangent operator is going to be one of the outputs of the multiscale analysis together with the homogenized stresses.

The definition of the homogenized tangent constitutive operator is given as the directional derivative of the homogenized constitutive functional,  $\bar{\mathcal{F}}(\bar{\boldsymbol{\varepsilon}})$ , defined by

$$\bar{\mathcal{F}}(\bar{\boldsymbol{\varepsilon}}) = \frac{1}{V^\mu} \int_{V^\mu} \mathcal{F}^\mu(\boldsymbol{\varepsilon}^\mu) dV \quad (\text{D.4})$$

which is derived from the macro-micro stress average relation. Its directional derivative at  $\bar{\boldsymbol{\varepsilon}}^*$  in the direction of  $\delta\bar{\boldsymbol{\varepsilon}}$  is given by,

$$\mathcal{D}\bar{\mathcal{F}}(\bar{\boldsymbol{\varepsilon}})[\delta\bar{\boldsymbol{\varepsilon}}] = \frac{1}{V^\mu} \int_{V^\mu} \mathcal{D}\mathcal{F}^\mu(\boldsymbol{\varepsilon}^\mu)[\delta\bar{\boldsymbol{\varepsilon}}] dV \quad (\text{D.5})$$

$$= \frac{1}{V^\mu} \int_{V^\mu} \left. \frac{d}{d\boldsymbol{\varepsilon}} \right|_{\boldsymbol{\varepsilon}=\bar{\boldsymbol{\varepsilon}}_\epsilon} \mathcal{F}^\mu(\boldsymbol{\varepsilon}^\mu(\bar{\boldsymbol{\varepsilon}}_\epsilon)) dV \quad (\text{D.6})$$

knowing that the micro strain is a function of the macro strain and the gradient of micro displacement fluctuation can also be related to the macro strain ,

$$\boldsymbol{\varepsilon}^\mu = \boldsymbol{\varepsilon}^\mu(\bar{\boldsymbol{\varepsilon}}) \quad \text{and} \quad \nabla_y^s \tilde{\mathbf{u}}^\mu = \tilde{\boldsymbol{\varepsilon}}^\mu = \tilde{\boldsymbol{\varepsilon}}^\mu(\bar{\boldsymbol{\varepsilon}}) = \mathcal{G}(\bar{\boldsymbol{\varepsilon}}) \quad (\text{D.7})$$

noticing that the relationship between  $\nabla_y^s \tilde{\mathbf{u}}^\mu$  and  $\bar{\boldsymbol{\varepsilon}}$  is generally nonlinear (de Souza Neto and Feijóo 2006). Using this information with the directional derivative definition, eq. (D.5) can be further developed using the chain rule,

$$\mathcal{D}\bar{\mathcal{F}}(\bar{\boldsymbol{\varepsilon}})[\delta\bar{\boldsymbol{\varepsilon}}] = \frac{1}{V^\mu} \int_{V^\mu} \left. \frac{d}{d\boldsymbol{\varepsilon}} \right|_{\boldsymbol{\varepsilon}=\bar{\boldsymbol{\varepsilon}}_\epsilon} \mathcal{F}^\mu(\bar{\boldsymbol{\varepsilon}}_\epsilon + \mathcal{G}(\bar{\boldsymbol{\varepsilon}}_\epsilon)) dV \quad (\text{D.8})$$

$$= \frac{1}{V^\mu} \int_{V^\mu} \left. \frac{d\mathcal{F}^\mu}{d\boldsymbol{\varepsilon}^\mu} \right|_{\boldsymbol{\varepsilon}^\mu=\boldsymbol{\varepsilon}_*^\mu} : \left( \delta\bar{\boldsymbol{\varepsilon}} + \left. \frac{d}{d\boldsymbol{\varepsilon}} \right|_{\boldsymbol{\varepsilon}=\bar{\boldsymbol{\varepsilon}}_\epsilon} \mathcal{G}(\bar{\boldsymbol{\varepsilon}}_\epsilon) \right) dV \quad (\text{D.9})$$

$$= \frac{1}{V^\mu} \int_{V^\mu} \left. \frac{d\mathcal{F}^\mu}{d\boldsymbol{\varepsilon}^\mu} \right|_{\boldsymbol{\varepsilon}^\mu=\boldsymbol{\varepsilon}_*^\mu} : \delta\bar{\boldsymbol{\varepsilon}} dV + \frac{1}{V^\mu} \int_{V^\mu} \left. \frac{d\mathcal{F}^\mu}{d\boldsymbol{\varepsilon}^\mu} \right|_{\boldsymbol{\varepsilon}^\mu=\boldsymbol{\varepsilon}_*^\mu} : \left. \frac{d}{d\boldsymbol{\varepsilon}} \right|_{\boldsymbol{\varepsilon}=\bar{\boldsymbol{\varepsilon}}_\epsilon} \mathcal{G}(\bar{\boldsymbol{\varepsilon}}_\epsilon) dV \quad (\text{D.10})$$

$$= \frac{1}{V^\mu} \int_{V^\mu} \mathcal{D}\mathcal{F}^\mu(\boldsymbol{\varepsilon}^\mu)[\delta\bar{\boldsymbol{\varepsilon}}] dV + \frac{1}{V^\mu} \int_{V^\mu} \mathcal{D}\mathcal{F}^\mu(\boldsymbol{\varepsilon}^\mu) [\mathcal{D}\mathcal{G}(\bar{\boldsymbol{\varepsilon}})[\delta\bar{\boldsymbol{\varepsilon}}]] dV \quad (\text{D.11})$$

where it was used the following macro strain perturbation at  $\bar{\boldsymbol{\varepsilon}}_\epsilon$ ,

$$\bar{\boldsymbol{\varepsilon}}_\epsilon = \bar{\boldsymbol{\varepsilon}}_* + \epsilon \delta\bar{\boldsymbol{\varepsilon}} \quad (\text{D.12})$$

the point  $\boldsymbol{\varepsilon}_*^\mu = \bar{\boldsymbol{\varepsilon}}_* + \mathcal{G}(\bar{\boldsymbol{\varepsilon}}_*)$  and the relationship presented in appendix A.2. Using the chain rule notation shown in appendix A.3 we can arrive at the same result in eq. (D.11). This result

agree with the ones presented in the literature (Terada and Kikuchi 2001; de Souza Neto and Feijóo 2006; Perić et al. 2011; Blanco et al. 2016)

In a time discrete context, eq. (D.11) generates the homogenized constitutive tangent operator, which can be written as

$$\bar{\mathbf{D}} : \delta \bar{\boldsymbol{\varepsilon}} = \frac{1}{V^\mu} \int_{V^\mu} \mathbf{D}^\mu : \delta \bar{\boldsymbol{\varepsilon}} dV + \frac{1}{V^\mu} \int_{V^\mu} \mathbf{D}^\mu : \tilde{\mathbf{A}} : \delta \bar{\boldsymbol{\varepsilon}} dV \quad (\text{D.13})$$

where  $\bar{\mathbf{D}}$  is the homogenized tangent constitutive tensor,  $\mathbf{D}^\mu$  is the micro tangent constitutive tensor. The tensor  $\tilde{\mathbf{A}}$  is the tangential relation between macro strain  $\bar{\boldsymbol{\varepsilon}}$  and the gradient of micro displacement fluctuation

$$\tilde{\mathbf{A}} : \delta \bar{\boldsymbol{\varepsilon}} = \mathcal{D}\mathcal{G}(\bar{\boldsymbol{\varepsilon}})[\delta \bar{\boldsymbol{\varepsilon}}] \quad (\text{D.14})$$

The tangential relation  $\tilde{\mathbf{A}}$  is obtained using one form of the linearized micro equilibrium, presented in appendix D.5. The first contribution to this homogenized operator is called Taylor contribution and the second the fluctuation contribution (Sánchez et al. 2013).

Eq. (D.13) in its space discrete form for FEM implementation is obtained using the notation from appendix E,

$$\bar{\mathbf{D}} = \frac{1}{V^\mu} \int_{hV^\mu} \mathbf{D}^\mu dV + \frac{1}{V^\mu} \int_{hV^\mu} \mathbf{D}^\mu \tilde{\mathbf{A}} dV \quad (\text{D.15})$$

### D.3. HOMOGENIZED TANGENT CONSTITUTIVE OPERATOR CONSIDERING TAYLOR ASSUMPTION FOR THE MICRO DISPLACEMENT FLUCTUATION

This section details the formulation for computing the homogenized constitutive operator considering Taylor assumption for micro displacement fluctuations.

Considering the Taylor assumption,  $\tilde{\mathbf{u}} = \mathbf{0}$  in the whole micro domain, the homogenized constitutive tensor, from eq. (D.13), becomes,

$$\mathbf{D}_T = \frac{1}{V^\mu} \int_{V^\mu} \mathbf{D}^\mu dV \quad (\text{D.16})$$

which is the classic mixing theory result. Within this assumption  $\mathcal{G} = \tilde{\mathbf{u}} = \mathbf{0}$  and therefore  $\tilde{\mathbf{A}} = \mathbf{0}$ . This constitutive tangent operator measures how the macroscopic stress varies under the Taylor assumption at the state defined by the microscopic strain (de Souza Neto and Feijóo 2006). If the constitutive functional  $\mathbf{D}^\mu$  does not depend on  $\mathbf{y}$  then it can be taken out of the integral expression. Then we can subdivide the micro domain in its homogenized parts, resulting in

$$\mathbf{D}_T = \sum_i^{gp} \frac{\mathbf{D}_i^\mu}{V^\mu} \int_{V_i^\mu} dV = \sum_i^{gp} v_i \mathbf{D}_i^\mu \quad (\text{D.17})$$

where  $v_i = V_i^\mu / V^\mu$  is the volume fraction of the solid fraction  $i$ . The nonlinear version is obtained by simply using the tangent constitutive operator computed as shown in appendix B.5 for the general case using Von Mises yield criteria and appendix B.6 considering isotropic hardening. In the nonlinear case, the tangent constitutive operator can vary from element to element, therefore we should compute the volume weighted average from eq. (D.16).

#### D.4. LINEARIZATION OF MICRO EQUILIBRIUM

In this section we discuss the procedure to linearize the micro equilibrium equation using standard techniques. From the definition of the linearization, eq. (3.25), repeated here for convenience

$$G(\mathbf{u}_*^\mu, \boldsymbol{\eta}) + \mathcal{D}G(\mathbf{u}_*^\mu, \boldsymbol{\eta})[\delta\mathbf{u}^\mu] = 0 \quad (\text{D.18})$$

It is important to remark that the linearization procedure starts at a guess point,  $\mathbf{u}_*^\mu$ , and we are interested in finding a correction,  $\delta\mathbf{u}^\mu$ . This means that the first term is only equals to zero, from equilibrium eq. (3.24), when we arrive at the converged solution. We proceed by substituting the definition of the function  $G(\tilde{\mathbf{u}}^\mu, \boldsymbol{\eta})$ , eq. (3.24), in the above equation,

$$\int_{V^\mu} \mathcal{F}^\mu(\boldsymbol{\varepsilon}_*^\mu) : \nabla_y^s \boldsymbol{\eta} dV + \int_{V^\mu} \mathcal{D}\mathcal{F}^\mu(\boldsymbol{\varepsilon}_*^\mu)[\delta\mathbf{u}^\mu] : \nabla_y^s \boldsymbol{\eta} dV = 0 \quad (\text{D.19})$$

Because at a micro scale step we have fixed macro strain,  $\delta\bar{\boldsymbol{\varepsilon}} = \mathbf{0}$ , we can write the perturbation as

$$\delta\mathbf{u}^\mu = \delta\bar{\boldsymbol{\varepsilon}}\mathbf{y} + \delta\tilde{\mathbf{u}}^\mu = \delta\tilde{\mathbf{u}}^\mu \quad (\text{D.20})$$

now, using the definition of directional derivative from appendix A.1 and following the same procedure as in appendix B.0.1, we get

$$\mathcal{D}\mathcal{F}^\mu(\boldsymbol{\varepsilon}_*^\mu)[\delta\mathbf{u}^\mu] = \left. \frac{d}{d\epsilon} \right|_{\epsilon=0} \mathcal{F}^\mu(\boldsymbol{\varepsilon}_\epsilon^\mu) \quad (\text{D.21})$$

$$= \left. \frac{d\mathcal{F}^\mu}{d\boldsymbol{\varepsilon}^\mu} \right|_{\boldsymbol{\varepsilon}_*^\mu} : \left. \frac{d\boldsymbol{\varepsilon}_\epsilon^\mu}{d\epsilon} \right|_{\epsilon=0} \quad (\text{D.22})$$

$$= \mathcal{D}\mathcal{F}^\mu(\boldsymbol{\varepsilon}_*^\mu)[\nabla_y^s \delta\tilde{\mathbf{u}}^\mu] \quad (\text{D.23})$$

where it was used the chain rule and the perturbed strain

$$\boldsymbol{\varepsilon}_\epsilon^\mu = \boldsymbol{\varepsilon}_*^\mu + \epsilon\delta\boldsymbol{\varepsilon}^\mu \quad (\text{D.24})$$

$$= \boldsymbol{\varepsilon}_*^\mu + \epsilon(\delta\bar{\boldsymbol{\varepsilon}} + \nabla_y^s \delta\tilde{\mathbf{u}}^\mu) \quad (\text{D.25})$$

$$= \boldsymbol{\varepsilon}_*^\mu + \epsilon\nabla_y^s \delta\tilde{\mathbf{u}}^\mu \quad (\text{D.26})$$

where eq. (D.20) was used. The tangent operator is computed using information from the known point  $\boldsymbol{\varepsilon}_*^\mu = \boldsymbol{\varepsilon}^{\mu(k)}$ . Substituting this result, eq. (D.23), in the eq. (D.19) we get,

$$\int_{V^\mu} \mathcal{D}\mathcal{F}^\mu(\boldsymbol{\varepsilon}_*^\mu)[\nabla\delta\mathbf{u}^\mu] : \nabla_y^s \boldsymbol{\eta} dV = - \int_{V^\mu} \mathcal{F}^\mu(\boldsymbol{\varepsilon}_*^\mu) : \nabla_y^s \boldsymbol{\eta} dV \quad (\text{D.27})$$

The results agree with the literature (Michel et al. 1999; de Souza Neto and Feijóo 2006; Asada and Ohno 2007; Perić et al. 2011; Gruer 2015; Saeb et al. 2016). This equation in space discretized iterative form, using notation from appendix E, can be written as

$$\int_{V^\mu} (\mathbf{B}^g)^T \mathbf{D}^{\mu(k)} \mathbf{B}^g \delta\tilde{\mathbf{u}}^{\mu(k+1)} dV = - \int_{V^\mu} (\mathbf{B}^g)^T \hat{\boldsymbol{\sigma}}^{\mu(k)} dV \quad (\text{D.28})$$

where the tangent matrix and stress vector are computed using the known internal variables, and the system is solved for the Newton correction  $\delta\tilde{\mathbf{u}}^\mu$ . This equation is similar to eq. (B.12), the only difference is the absence of external force vector. Notice that the macro strain does not appears splicitly in here, but it will affect the calculation of the stress when using the state update procedure in appendix B.4.

After solving the linear system we update the solution with

$$\mathbf{u}^{\mu(k+1)} = \mathbf{u}^{\mu(k)} + \delta\tilde{\mathbf{u}}^{\mu(k+1)} \quad (\text{D.29})$$

## D.5. TANGENTIAL RELATION BETWEEN MACRO STRAIN AND GRADIENT OF MICRO DISPLACEMENT FLUCTUATION

In this appendix we discuss an specialization of the linearized micro equilibrium equation in eq. (D.27). This tangential relation between macro strain,  $\bar{\boldsymbol{\varepsilon}}$ , gradient of micro displacement fluctuation,  $\nabla_y^s \tilde{\mathbf{u}}^\mu$ , is used to find the fluctuation contribution to the homogenized constitutive tangent operator in eq. (D.13).

It emerges from linearization of the micro equilibrium at a known point  $\mathbf{u}_*^\mu$  and at a *specific* direction  $\delta \mathbf{u}^\mu = \delta \bar{\boldsymbol{\varepsilon}} \mathbf{y} + \delta \tilde{\mathbf{u}}^\mu$ . This direction is formed by a pair,  $\bar{\boldsymbol{\varepsilon}}_\epsilon$  and  $\tilde{\mathbf{u}}_\epsilon^\mu$ , that solves the equilibrium equation in eq. (3.24). Differently from eq. (D.19), the first term will be equal to zero due equilibrium. Which means we are already with the converged micro displacement that satisfy micro equilibrium. Therefore, the linearized equilibrium equation becomes

$$\int_{V^\mu} \mathcal{D}\mathcal{F}^\mu(\boldsymbol{\varepsilon}_*^\mu)[\delta \mathbf{u}^\mu] : \nabla_y^s \boldsymbol{\eta} dV = 0 \quad (\text{D.30})$$

Applying the definition of directional derivative we get,

$$\mathcal{D}\mathcal{F}^\mu(\boldsymbol{\varepsilon}_*^\mu)[\delta \mathbf{u}^\mu] = \left. \frac{d}{d\epsilon} \mathcal{F}^\mu(\boldsymbol{\varepsilon}_\epsilon^\mu) \right|_{\epsilon=0} \quad (\text{D.31})$$

$$= \left. \frac{d\mathcal{F}^\mu}{d\boldsymbol{\varepsilon}^\mu} \right|_{\boldsymbol{\varepsilon}_*^\mu} : \left. \frac{d\boldsymbol{\varepsilon}_\epsilon^\mu}{d\epsilon} \right|_{\epsilon=0} \quad (\text{D.32})$$

$$= \mathbf{D}^\mu : \delta \boldsymbol{\varepsilon}^\mu \quad (\text{D.33})$$

$$= \mathbf{D}^\mu : (\delta \bar{\boldsymbol{\varepsilon}} + \nabla_y^s \delta \tilde{\mathbf{u}}^\mu) \quad (\text{D.34})$$

where it was used the definition of the perturbation  $\boldsymbol{\varepsilon}_\epsilon^\mu = \boldsymbol{\varepsilon}_*^\mu + \epsilon \delta \boldsymbol{\varepsilon}^\mu$  and the definition of constitutive tangent  $\mathbf{D}^\mu = \left. \frac{d\mathcal{F}^\mu}{d\boldsymbol{\varepsilon}^\mu} \right|_{\boldsymbol{\varepsilon}_*^\mu}$ .

Now, substituting this derivative in a time discrete version of the linearized equilibrium, eq. (D.30), we get the wanted tangential relation,

$$\int_{V^\mu} \mathbf{D}^\mu : \nabla_y^s \delta \tilde{\mathbf{u}}^\mu : \nabla_y^s \boldsymbol{\eta} dV = - \int_{V^\mu} \mathbf{D}^\mu : \delta \bar{\boldsymbol{\varepsilon}} : \nabla_y^s \boldsymbol{\eta} dV \quad (\text{D.35})$$

This result agrees with the literature (Terada and Kikuchi 2001; de Souza Neto and Feijóo 2006; Asada and Ohno 2007; Perić et al. 2011)

Using the relation from appendix A.2 and the notation from appendix E we get the following discrete linearized equilibrium equation

$$\int_{hV^\mu} (\mathbf{B}^g)^T \mathbf{D}^\mu \mathbf{B}^g \delta \tilde{\mathbf{u}}^\mu dV = - \int_{hV^\mu} (\mathbf{B}^g)^T \mathbf{D}^\mu \delta \bar{\boldsymbol{\varepsilon}} dV \quad (\text{D.36})$$

where  $\mathbf{B}^g$  is the discrete gradient matrix and  $\mathbf{D}^\mu$  is the consistent tangent constitutive matrix. Notice that this equation establishes the linear tangential relation between the macro strain and the displacement fluctuation. For a given macro displacement correction  $\delta \bar{\boldsymbol{\varepsilon}}$  find the micro displacement fluctuation correction  $\delta \tilde{\mathbf{u}}^\mu$ . Notice that we need to apply proper boundary conditions to this equation so we get an admissible solution.

We now focus on how to obtain the tangential tensor,  $\tilde{\mathbf{A}}$ , which relates

$$\nabla \delta \tilde{\mathbf{u}}^\mu = \tilde{\mathbf{A}} : \delta \bar{\boldsymbol{\varepsilon}} \quad (\text{D.37})$$

this is used to compute the fluctuation part of the homogenized constitutive tangent  $\tilde{\mathbf{D}}$ , eq. (D.13).

In order to obtain this tangent operator we need to use the linearized version of the micro equilibrium equations presented in eq. (D.36). The procedure can be described mathematically as in de Souza Neto and Feijóo (2006) and Sánchez et al. (2013) or in a algorithmic form as in Saeb et al. (2016).

For a given unit macro strain perturbation,  $\delta\bar{\varepsilon}_{ij} = \mathbf{e}_i \otimes \mathbf{e}_j$ , which in a discrete FEM setting will be three vectors with unit component,  $[1, 0, 0]$ ,  $[0, 1, 0]$ ,  $[0, 0, 1]$ , we compute the solution of the linear system from eq. (D.36) using the last consistent constitutive tangent  $\mathbf{D}^\mu$ , resulting in  $\delta\tilde{\mathbf{u}}_{ij}^\mu$  which the gradient is going to be part of the tensor  $\tilde{\mathbf{A}}$ . Substituting the strain perturbations in eq. (D.35),

$$\int_{V^\mu} \nabla_y^s \boldsymbol{\eta} : \mathbf{D}^\mu : \nabla_y^s \delta\tilde{\mathbf{u}}_{ij}^\mu dV = - \left[ \int_{V^\mu} \nabla_y^s \boldsymbol{\eta} : \mathbf{D}^\mu dV \right] \mathbf{e}_i \otimes \mathbf{e}_j \quad (\text{D.38})$$

Since eq. (D.35) is linear for  $\delta\tilde{\mathbf{u}}^\mu$ , we can write its solution as a linear combination of the solutions  $\delta\tilde{\mathbf{u}}_{ij}^\mu$ ,

$$\delta\tilde{\mathbf{u}}^\mu = \delta\bar{\varepsilon}_{ij} \delta\tilde{\mathbf{u}}_{ij}^\mu \quad (\text{D.39})$$

If we take the gradient on both sides we get an expression for the tangent relation shown in eq. (D.14),

$$\nabla_y^s \delta\tilde{\mathbf{u}}^\mu = \delta\bar{\varepsilon}_{ij} \nabla_y^s \delta\tilde{\mathbf{u}}_{ij}^\mu = \tilde{\mathbf{A}} : \delta\bar{\varepsilon} = \mathcal{D}\mathcal{G}(\bar{\varepsilon})[\delta\bar{\varepsilon}] \quad (\text{D.40})$$

Therefore the components of the tensor can be found  $\tilde{\mathbf{A}} = \nabla_y^s \delta\tilde{\mathbf{u}}_{ij}^\mu$ .

In a FEM discretized situation, the solution of the linear system in eq. (D.36) will be a vector,  $\delta\tilde{\mathbf{u}}_j^\mu$  which will be arranged as columns of a matrix, so we can compute the discrete version of the tensor  $\tilde{\mathbf{A}}$  as,

$$\tilde{\mathbf{A}} = \mathbf{B} [\delta\tilde{\mathbf{u}}_1 \quad \delta\tilde{\mathbf{u}}_2 \quad \delta\tilde{\mathbf{u}}_3] \quad (\text{D.41})$$

for plane problems, this will result in a 3x3 matrix. Notice that we are using the discrete gradient in a element setting, therefore we only use the interested part of the vectors  $\delta\tilde{\mathbf{u}}_j$ . This procedure is explicit in the algorithm 7.

## E. NOTATION CONVENTION

This notation is from Simo and Hughes (1998) and de Souza Neto et al. (2008).

### E.1. CONTRACTION OF TENSORS

When converting between tensor notation to Voigt notation (vectors and matrices),

$$\boldsymbol{\sigma} : \nabla \boldsymbol{\eta} \equiv \boldsymbol{\sigma}^T \mathbf{B}^g \boldsymbol{\eta} \quad (\text{E.1})$$

where the 2nd order stress tensor was substituted by a vector, the double contraction by a dot product (using the transpose notation) and the gradient by its discrete form by means for a matrix  $\mathbf{B}^g$ .

Applications of fourth order tensors to second order ones yields,

$$\mathbf{D} : \boldsymbol{\varepsilon} \equiv \mathbf{D} \boldsymbol{\varepsilon} \quad (\text{E.2})$$

Those two conventions can be applied to expressions with two double contractions,

$$\mathbf{D} : \nabla \delta \mathbf{u} : \nabla \boldsymbol{\eta} \equiv (\mathbf{B}^g \boldsymbol{\eta})^T \mathbf{D} \mathbf{B}^g \delta \mathbf{u} \quad (\text{E.3})$$

where it was used the transpose properties  $(\mathbf{A}\mathbf{U})^T \equiv \mathbf{U}^T \mathbf{A}^T$  and  $(\mathbf{A}^T)^T \equiv \mathbf{A}$ .

## E.2. TENSOR PRODUCT

The tensor product between two second order tensors is substituted with,

$$\mathbf{a} \otimes \mathbf{b} \equiv \mathbf{a}\mathbf{b}^T \quad (\text{E.4})$$

## E.3. SECOND ORDER TENSORS

Second order tensors are mapped to vectors,

$$\boldsymbol{\sigma} \equiv \begin{bmatrix} \sigma_{11} \\ \sigma_{22} \\ \sigma_{12} \end{bmatrix} \quad (\text{E.5})$$

## E.4. FOURTH ORDER TENSORS

Fourth order tensors will be mapped onto matrices. The fourth order identity, for instance, in a 2d setting, will be mapped into

$$\mathbf{I} \equiv \mathbf{I} = \begin{bmatrix} 1 & 0 & 0 \\ 0 & 1 & 0 \\ 0 & 0 & 1 \end{bmatrix} \quad (\text{E.6})$$

The general symmetric fourth order tensor will be mapped into,

$$\mathbf{D} \equiv \begin{bmatrix} D_{1111} & D_{1122} & D_{1112} \\ & D_{2222} & D_{2212} \\ & & D_{1212} \end{bmatrix} \quad (\text{E.7})$$

## F. ALGORITHMS

In this section the algorithms used to implement the solutions are presented.

### F.1. STANDARD NEWTON PROCEDURE

### F.2. STATE UPDATE PROCEDURE

---

**Algorithm 1** Standard Newton procedure

---

**procedure** NEWTON( $\mathbf{u}_n$ )

(1) Set initial guess  $\mathbf{u}_{n+1}^{(0)} = \mathbf{u}_n$

Element loop

(2) Compute  $\mathbf{f}_{(e)}^{\text{int}}(\boldsymbol{\sigma}_{n+1}^{(0)})$  and  $\mathbf{D}$  using  $\boldsymbol{\varepsilon}_{n+1}^{(0)} = \mathbf{B}\mathbf{u}_{n+1}^{(0)}$  call `suvm()` and `ctvm()`

(3) Compute  $\mathbf{K}_T^{(e)} = \sum_i^{gp} w_i j_i \mathbf{B}_i^T \mathbf{D}_i \mathbf{B}_i$

End Element loop

(4) Assemble global and solve for  $\delta \mathbf{u}^{(k+1)} = -\mathbf{K}_T^{-1} [\mathbf{f}^{\text{int}} - \lambda_{n+1} \bar{\mathbf{f}}^{\text{ext}}]$

(5) Apply Newton correction  $\mathbf{u}_{n+1}^{(k+1)} = \mathbf{u}_{n+1}^{(k)} + \delta \mathbf{u}^{(k+1)}$

Element loop

(6) Update strains  $\boldsymbol{\varepsilon}_{n+1}^{(k+1)} = \mathbf{B}\mathbf{u}_{n+1}^{(k+1)}$

(7) Compute  $\mathbf{f}_{(e)}^{\text{int}}(\boldsymbol{\sigma}_{n+1}^{(k+1)})$  and  $\mathbf{D}$  using  $\boldsymbol{\varepsilon}_{n+1}^{(k+1)}$

(8) Compute  $\mathbf{K}_T^{(e)} = \sum_i^{gp} w_i j_i \mathbf{B}_i^T \bar{\mathbf{D}}_i \mathbf{B}_i$

End Element loop

**if**  $\mathbf{r} = \mathbf{f}^{\text{int}} - \lambda_{n+1} \bar{\mathbf{f}}^{\text{ext}}$  converged **then**

Set  $(\cdot)_{n+1} = (\cdot)_{n+1}^{(k+1)}$  and Exit

**else**

Set  $k = k + 1$  and Go to (4)

**end if**

**end procedure**

---

---

**Algorithm 2** State update von Mises

---

**procedure** SUVM( $\Delta \boldsymbol{\varepsilon} = \boldsymbol{\varepsilon}_{n+1}^{(k+1)} - \boldsymbol{\varepsilon}_n$ ,  $\boldsymbol{\alpha}_n$ , mat)

(1) Compute trial state

(2) Check plastic admissibility

**if**  $\Phi < 0$  **then**

Elastic step set  $(\cdot)_{n+1} = (\cdot)_{n+1}^{\text{trial}}$  and Exit

**else**

Call returning mapping algorithm to compute  $\boldsymbol{\sigma}_{n+1}$  and  $\boldsymbol{\alpha}_{n+1}$

**end if**

**end procedure**

---

### F.3. CONSTITUTIVE CONSISTENT TANGENT MATRIX

---

#### Algorithm 3 Consistent tangent

---

```

procedure CTVM( $\sigma_{n+1}$ ,  $\alpha_n$ , flag, mat)
  if flag is elastic then
    Compute and return  $D^e(\text{mat})$ 
  else flag is plastic
    Compute and return  $D^{ep}(\text{mat}, \sigma_{n+1}, \alpha_n)$ 
  end if
end procedure

```

---

### F.4. NEWTON PROCEDURE FOR MULTISCALE ANALYSIS

---

#### Algorithm 4 Newton procedure for multiscale

---

```

procedure NEWTON( $\mathbf{u}_n$ )
  (1) Set initial guess  $\mathbf{u}_{n+1}^{(0)} = \mathbf{u}_n$ 
      Element loop
  (2) Compute  $\mathbf{f}_{(e)}^{\text{int}}(\bar{\boldsymbol{\sigma}}_{n+1}^{(0)})$  and  $\bar{\mathbf{D}}$  using  $\bar{\boldsymbol{\epsilon}}_{n+1}^{(0)} = \mathbf{B}\mathbf{u}_{n+1}^{(0)}$  call multiscale()
  (3) Compute  $\mathbf{K}_T^{(e)} = \sum_i^{gp} \mathbf{B}_i^T \bar{\mathbf{D}}_i \mathbf{B}_i w_i j_i$ 
      End Element loop
  (4) Assemble global and solve for  $\delta \mathbf{u}^{(k+1)} = -\mathbf{K}_T^{-1}[\mathbf{f}^{\text{int}} - \lambda_{n+1} \bar{\mathbf{f}}^{\text{ext}}]$ 
  (5) Apply Newton correction  $\mathbf{u}_{n+1}^{(k+1)} = \mathbf{u}_{n+1}^{(k)} + \delta \mathbf{u}^{(k+1)}$ 
      Element loop
  (6) Update strains  $\bar{\boldsymbol{\epsilon}}_{n+1}^{(k+1)} = \mathbf{B}\mathbf{u}_{n+1}^{(k+1)}$ 
  (7) Compute  $\mathbf{f}_{(e)}^{\text{int}}(\bar{\boldsymbol{\sigma}}_{n+1}^{(k+1)})$  and  $\bar{\mathbf{D}}^{(e)}$  using  $\bar{\boldsymbol{\epsilon}}_{n+1}^{(k+1)}$  call multiscale()
  (8) Compute  $\mathbf{K}_T^{(e)} = \sum_i^{gp} \mathbf{B}_i^T \bar{\mathbf{D}}_i \mathbf{B}_i w_i j_i$ 
      End Element loop
  if  $\mathbf{r} = \mathbf{f}^{\text{int}} - \lambda_{n+1} \bar{\mathbf{f}}^{\text{ext}}$  converged then
    Set  $(\cdot)_{n+1} = (\cdot)_{n+1}^{(k+1)}$  and Exit
  else
    Set  $k = k + 1$  and Go to (4)
  end if
end procedure

```

---

## F.5. MULTISCALE INCREMENTAL PROCEDURE

---

### Algorithm 5 Multiscale incremental procedure

---

**procedure** MULTISCALE( $\bar{\boldsymbol{\epsilon}}_{n+1}, \tilde{\mathbf{u}}_n^\mu$ )

(1) Set initial  $\tilde{\mathbf{u}}_{n+1}^{\mu(0)} = \tilde{\mathbf{u}}_n^\mu$

Element loop at micro scale

(2) Compute  $\mathbf{f}_{(e)}^{\text{int}}(\boldsymbol{\sigma}_{n+1}^{\mu(0)})$  and  $\mathbf{D}^\mu$  using  $\boldsymbol{\epsilon}_{n+1}^{\mu(0)} = \bar{\boldsymbol{\epsilon}}_{n+1} + \mathbf{B}\tilde{\mathbf{u}}_{n+1}^{\mu(0)}$  call `suvm()` and `ctvm()`

(3) Compute  $\mathbf{K}_T^{(e)} = \sum_i^{gp} \mathbf{B}_i^T \mathbf{D}_i^\mu \mathbf{B}_i w_i j_i$

End Element loop

(4) Assemble global and solve for  $\delta\tilde{\mathbf{u}}^{\mu(k+1)} = -\mathbf{K}_T^{-1} \mathbf{f}^{\text{int}}$

(5) Apply Newton correction  $\tilde{\mathbf{u}}_{n+1}^{\mu(k+1)} = \tilde{\mathbf{u}}_{n+1}^{\mu(k)} + \delta\tilde{\mathbf{u}}^{\mu(k+1)}$

Element loop at micro scale

(6) Update strains  $\boldsymbol{\epsilon}_{n+1}^{\mu(k+1)} = \bar{\boldsymbol{\epsilon}}_{n+1} + \mathbf{B}\tilde{\mathbf{u}}_{n+1}^{\mu(k+1)}$

(7) Compute  $\mathbf{f}_{(e)}^{\text{int}}(\boldsymbol{\sigma}_{n+1}^{\mu(k+1)})$  and  $\mathbf{D}^\mu$  using  $\boldsymbol{\epsilon}_{n+1}^{\mu(k+1)}$  call `suvm()` and `ctvm()`

(8) Compute  $\mathbf{K}_T^{(e)} = \sum_i^{gp} \mathbf{B}_i^T \mathbf{D}_i^\mu \mathbf{B}_i w_i j_i$

(9) Compute  $\mathbf{f}_D^{(e)} = \sum_i^{gp} \mathbf{B}_i^T \mathbf{D}_i^\mu w_i j_i$

End Element loop

**if**  $\mathbf{r} = \mathbf{f}^{\text{int}}$  converged **then**

Set  $(\cdot)_{n+1} = (\cdot)_{n+1}^{(k+1)}$

(10) Assemble global  $\mathbf{K}_T$  and  $\mathbf{f}_D$

(11) Compute and return  $\bar{\boldsymbol{\sigma}}_{n+1}$  and  $\bar{\mathbf{D}}$  call `hstress()` and `hct()`

**else**

Set  $k = k + 1$  and Go to (4)

**end if**

**end procedure**

---

## F.6. HOMOGENIZATION PROCEDURES

---

### Algorithm 6 Homogenized stress

---

**procedure** HSTRESS( $\boldsymbol{\sigma}_{n+1}^\mu$ )

Element loop

(1) Compute volume average  $\bar{\boldsymbol{\sigma}} += \sum_i^{gp} \boldsymbol{\sigma}_{n+1}^\mu w_i j_i$

End Element loop

(2) Return  $\bar{\boldsymbol{\sigma}}$

**end procedure**

---

---

**Algorithm 7** Homogenized constitutive tangent

---

**procedure** HCT( $\mathbf{K}_T, \mathbf{f}^D$ )

**for**  $\bar{\boldsymbol{\varepsilon}}_j$  in  $(\bar{\boldsymbol{\varepsilon}}_1, \bar{\boldsymbol{\varepsilon}}_2, \bar{\boldsymbol{\varepsilon}}_3) = ([1, 0, 0], [0, 1, 0], [0, 0, 1])$  **do**

(1) Compute  $\delta\tilde{\mathbf{u}}_j = -\mathbf{K}_T^{-1}\mathbf{f}^D\bar{\boldsymbol{\varepsilon}}_j$

**end for**

Element loop

(2) Compute  $\mathbf{D}_T += \frac{1}{V^\mu} \sum_i^{gp} \mathbf{D}^\mu j_i w_i$

(3) Compute  $\tilde{\mathbf{A}}^{(e)} = \mathbf{B}[\delta\tilde{\mathbf{u}}_1[e], \delta\tilde{\mathbf{u}}_2[e], \delta\tilde{\mathbf{u}}_3[e]]$

(4) Compute  $\tilde{\mathbf{D}} += \frac{1}{V^\mu} \sum_i^{gp} \tilde{\mathbf{A}}^{(e)} \mathbf{D}^\mu j_i w_i$

End Element loop

(5) Compute and return  $\bar{\mathbf{D}} = \mathbf{D}_T + \tilde{\mathbf{D}}$

**end procedure**

---